



TECHNISCHE
UNIVERSITÄT
WIEN

Master Thesis

Hollow Fibre Membrane Production Using a Nonsolvent Induced Phase Separation Spinning Unit

Carried out for the purpose of obtaining the degree of Master of Science (MSc or
Dipl.-Ing. or DI), submitted at TU Wien, Faculty of Mechanical and Industrial
Engineering, by:

Fatima Imran, BSc

Matr.Nr.: 01429906 Study Code: 066 473

Under the supervision of

Ao. Univ.Prof. Dipl.-Ing. Dr. techn Michael Harasek

Projektass. Dipl.-Ing. Benjamin Lukitsch

Projektass. Dipl.-Ing. Paul Ecker BSc

Institute of Chemical, Environmental und Bioscience Engineering, E166

Vienna, September 2022

Signature



TECHNISCHE
UNIVERSITÄT
WIEN

I confirm that going to press of this thesis needs the confirmation of the examination committee.

Affidavit

I declare in lieu of oath that I wrote this thesis and performed the associated research myself, using only literature cited in this volume. If text passages from sources are used literally, they are marked as such.

I confirm that this work is original and has not been submitted elsewhere for examination, nor is it currently under consideration for a thesis elsewhere.

Vienna, September 2022

Signature

Acknowledgements

I would like to express my sincerest gratitude to Prof. Harasek, for providing me with the opportunity to work and grow in a supporting team, and to be able to research an interesting and fulfilling theme and topic.

The Biomedfibre team and the whole group is acknowledged for their friendship and support in many ways. I would like to thank my thesis adviser Benjamin Lukitsch for his guidance, help and constant support during the whole research work. I thank Paul Ecker and Markus Pekovits for their help, support, direction and most importantly teamwork. Appreciation is also extended to the Thermal Process Engineering and Simulation and CFD (E166-02 and E166-02-2). They gave me support, advice, a friendly shoulder, and any help I needed at any point in time.

I also want to thank my parents for their sacrifices and providing their best to get me to where I am today. I want to thank my friends for always reminding me what is essential in life.

“No research without action, no action without research.”
-Kurt Lewin

Abstract

Membranes and membrane technology has become an essential part of modern-day life over the years. First and foremost, membranes can be found inside all living beings and serve extremely important purposes inside the body. Membrane technology, whilst beginning with biological membranes, has become a vast field of itself. Ever since the first successful asymmetric membrane produced using the nonsolvent induced phase separation (NIPS) in the 1960s, these types of membranes have found their application in a multitude of fields- from dialysis, blood oxygenation, extracorporeal membrane oxygenation in the medical field, to reverse osmosis, membrane distillation, gas separation and capture of carbon dioxide and methane, to wastewater hygienisation, to the food and pharmaceutical industry etc.

This thesis focuses mainly on the NIPS process and the asymmetric hollow fibre membranes spun from the newly built inhouse NIPS process plant (E166-02-2). NIPS is a multicomponent process, where a homogenous mixture of a polymer and a solvent (dope; in this case polyethersulfone (PES) and N-methyl-2-pyrrolidone (NMP) and any other additives is precipitated with a certain geometry in a nonsolvent (in this case water). Upon contact, diffusion is initiated, resulting in phase separation and polymer-rich and polymer-lean regions. This leads to membrane formation.

The theoretical framework behind this process will be closely examined, as well as the practical aspect of spinning fibres and characterising them. The scanning electron microscope (SEM), ultraviolet/visible light (UV/VIS) spectrophotometer, rheometer, porosity tests, ultrafiltration (UF), gas separation (GP) and tensile testing is used as means of characterisation. The newly built NIPS modular plant is what this thesis revolves around. The process beginning from the dope production to spinning and to modules ready for testing is the focus of this thesis. Documentation of the whole process is necessary, so that future research can be built upon. Certain parameters have been chosen and their effects on fibre morphology, UF or GP performance and mechanical stability have been examined- air gap length, PES concentration in the dope, dope viscosity, spinneret and dope temperature, NMP composition in the bore fluid, coagulation bath temperature, additives, dope and bore fluid flow rates. The results of each variation are mostly in alignment with literature and are proof that the NIPS plant requires further optimisation and operation to achieve desired and favourable asymmetric hollow fibres.

Kurzfassung

Membranen und Membrantechnik sind im Laufe der Jahre aus dem modernen Leben nicht mehr wegzudenken. Membranen sind in erster Linie in allen Lebewesen zu finden und erfüllen im Körper äußerst wichtige Aufgaben. Die Membrantechnologie begann zwar mit biologischen Membranen, hat sich aber zu einem weitreichenden Gebiet entwickelt. Seit der ersten erfolgreichen asymmetrischen Membran, die in den 1960er Jahren unter Verwendung der nicht lösungsmittelinduzierten Phasentrennung (NIPS) hergestellt wurde, haben diese Membrantypen ihre Anwendung in einer Vielzahl von Bereichen gefunden - von der Dialyse, Blutoxygenierung, extrakorporalen Membranoxygenierung, Umkehrosmose, Membrandestillation, Gastrennung und Abscheidung von Kohlendioxid und Methan, Abwasserreinigung, zur Lebensmittel- und Pharmaindustrie etc.

Diese Arbeit konzentriert sich hauptsächlich auf den NIPS-Prozess und die asymmetrischen Hohlfasermembranen, die aus der neu gebauten hauseigenen NIPS-Prozessanlage gesponnen werden. NIPS ist ein Mehrkomponentenverfahren, bei dem eine homogene Mischung aus einem Polymer und einem Lösungsmittel (Dope; in diesem Fall Polyethersulfon PES und N-Methyl-2-pyrrolidon NMP) und allen anderen Additiven in einem Nichtlösungsmittel (hier Wasser). Beim Kontakt wird eine Diffusion initiiert, was zu einer Phasentrennung und polymerreichen und polymerarmen Regionen führt. Dies führt zur Membranbildung.

Der theoretische Rahmen dieses Verfahrens wird ebenso beleuchtet wie der praktische Aspekt des Spinnens von Fasern und deren Charakterisierung. Zur Charakterisierung werden REM, UV/VIS-Gerät, Rheometer, Porositätsprüfung, Ultrafiltration (UF), Gastrennung (GP) und Zugversuche eingesetzt. Im Mittelpunkt dieser Arbeit steht die neu gebaute modulare NIPS-Anlage. Der Prozess von der Polymergemischherstellung über das Spinnen bis hin zu prüffertigen Modulen steht im Fokus dieser Arbeit. Bestimmte Parameter wurden ausgewählt und ihre Auswirkungen auf die Fasermorphologie, die UF- oder GP-Eigenschaften und die mechanische Stabilität untersucht- Luftspaltlänge, PES-Konzentration in der Spinnlösung, Spinnlösungviskosität, Spinndüsen- und Spinnlösungstemperatur, NMP-Zusammensetzung in der Bohrflüssigkeit, Koagulationsbadtemperatur, Additive, Dope- und Boreflüssigkeitsdurchflussraten. Die Ergebnisse jeder Variation stimmen größtenteils mit der Literatur überein und belegen, dass die NIPS-Anlage einer weiteren Optimierung und einem weiteren Betrieb bedarf, um die gewünschten und asymmetrischen Hohlfasern zu erzielen.

Table of Contents

Abstract	1
Kurzfassung.....	2
Table of Contents	3
1 Introduction and Motivation	6
1.1 Brief History of Membrane Separation Technology and Processes	6
1.2 Aim and Motivation	8
1.3 Structure of This Thesis.....	8
2 Review of Literature and Theoretical Framework.....	9
2.1 The Membrane	9
2.1.1 Classification Based on Structure.....	12
2.1.2 Classification Based on Geometry.....	14
2.1.3 Classification Based on Configuration	15
2.1.4 Classification Based on Separation Techniques: Pressure-driven Membrane Separation Processes	16
2.1.5 Classification Based on Transport Model	22
2.1.6 Classification Based on Production Process and Materials	31
2.2 The NIPS-Process	36
2.2.1 Thermodynamic Principle	36
2.2.2 Demixing Processes	41
2.2.3 The Ternary Phase Diagram	44
2.2.4 Spinning Process of Hollow Fibre Membranes.....	48
2.2.5 Influence of Spinning Parameters on the Hollow Fibre Membranes	48
3 Materials and Methodology	64
3.1 Dope Solution	64
3.1.1 Dope Solution Materials.....	64
3.1.2 Dope Solution Production Plant.....	64
3.1.3 Density of Dope Solution	65
3.1.4 Viscosity of Dope Solution	66
3.2 NIPS-Process	66
3.2.1 NIPS-Process Materials.....	66
3.2.2 NIPS-Process Plant.....	66
3.2.1 Post Treatment of Fibres	67
3.3 Membrane Characterization	68
3.3.1 SEM Analysis.....	68
3.3.2 Porosity.....	69
3.3.3 Membrane Module Production.....	71

3.3.4	Ultrafiltration Tests.....	71
3.3.5	Gas Separation Tests.....	73
3.3.6	Stress and Tensile Tests.....	73
4	Results.....	74
4.1	Viscosity of The Dope Solution.....	74
4.2	SEM Analysis.....	75
4.3	Ultrafiltration Tests.....	78
4.4	Gas Separation Tests.....	79
4.5	Mechanical Stability.....	81
5	Discussion and Interpretation.....	82
5.1	Viscosity of Dope Solution.....	82
5.2	SEM Analysis.....	82
5.2.1	Influence of Airgap on Fibres' Morphology.....	83
5.2.2	Influence of Polymer Concentration in Dope Solution on Fibres' Morphology.....	85
5.2.3	Influence of Temperature of Dope Solution on Fibres' Morphology.....	89
5.2.4	Influence of Solvent in Bore Fluid on Fibres' Morphology.....	91
5.2.5	Influence of Additives on Fibres' Morphology.....	93
5.2.6	Influence of Flow Rates on Fibres' Morphology.....	96
5.3	Ultrafiltration Tests.....	98
5.3.1	Influence of Flow Rates on UF Performance.....	99
5.3.2	Influence of Coagulation Bath Temperature on UF Performance and Fibre Morphology.....	99
5.4	Porosity Tests.....	101
5.5	Gas Separation Tests.....	106
5.5.1	Influence of Polymer Concentration in Dope Solution on Permselectivity Performance.....	106
5.5.2	Influence of Temperature of Dope Solution on Permselectivity Performance.....	107
5.5.3	Influence of PDMS Coating on Permselectivity Performance.....	108
5.6	Mechanical Stability.....	110
5.6.1	Influence of Polymer Concentration in Dope Solution on Mechanical Stability.....	110
6	Conclusions.....	112
7	Tables of Tables.....	114
8	Table of Figures.....	116
9	References.....	119
10	Appendix.....	124
10.1	SEM Pictures.....	124

10.1.1 PES Concentration Variation	124
10.1.2 Spinning Dope B; Temperature Variation	125
10.1.3 Spinning Dope B; Air Gap Length Variation	126
10.1.4 Spinning Dope B; Variation of NMP Concentration in Bore Fluid	127
10.1.5 Spinning Dope D; Coagulation Bath Temperature Variation	128
10.1.6 Spinning Dope D; Dope/Bore Fluid Flow Rate Variation	129
10.1.7 Spinning Dope C; GP Experiment (Temperature Variation)	130
10.1.8 Spinning Dopes, A_40, E and F; Additive Variation	131
10.2 Abbreviations	132
10.3 Symbols and Mathematical Abbreviations	133

1 Introduction and Motivation

1.1 Brief History of Membrane Separation Technology and Processes

The age-old and essential problem of separating liquids and gases has been a theme that has been researched and observed since at least the late 1740s- when Abbé Nolet used the word 'osmosis' to characterise the process of water permeating through a diaphragm [1], [2]. In 1861, Thomas Graham performed his first successful dialysis experiment using synthetic membranes. Around this time, James Clerk Maxwell came up with a thought experiment involving a very sharp demon that can follow every molecule in its course and distinguish between molecules (see Figure 1) [3]. Maxwell's thought experiment set up a vessel divided in the middle with a small hole controlled by the demon. The left part is filled with a gas consisting of hot and cold molecules, and the demon only lets the hot molecules pass into the right part of the vessel. Maxwell argued that this experiment worked against the second law of thermodynamics, as an ordered system seemed to result from an unordered random system. A driving force is exerted on the molecules, and the small hole acts as a membrane. A membrane cannot fully separate the mixture as the demon can. Furthermore, energy needs to be put into the system, while the thought experiment does not consider that the demon performs this task without any work done [3].

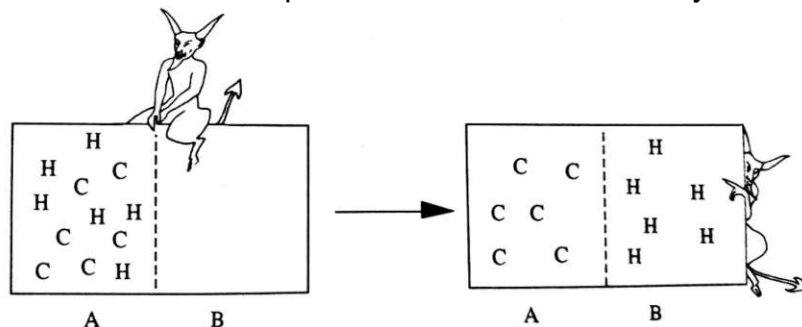


Figure 1: Maxwell's thought experiment- the demon has sorted the random disorderly system into an ordered system; H: hot, C: cold [3].

Further detail and discussion on the functionality of membranes will be elaborated on in later chapters.

The significant breakthroughs in membrane separation technology in the 1960s would not have been possible had it not been for the research that occurred since Nolet first discovered osmosis in 1748. The membrane industry and the resulting research and progress did not take off until the late 1900s, and before that, the process of separating through the usage of membranes had not been realised. It wasn't until the late 1930s that microporous nitrocellulose membranes were successfully produced commercially, and not until after World War II that membranes were significantly utilised for the application of testing drinking water in Germany and most of Europe [1], [2]. Until 1960, membranes found their application in only a few small-scale industries and exhibited four significant problems that impeded their widespread usage [1]:

- i. Undependable and unreliable results
- ii. Not fast enough for reasonable and sustainable industrial utilisation
- iii. Unselective

iv. Too pricey to justify application

However, the membrane industry underwent a breakthrough in the early 1960s when Loeb and Sourirajan conceived of and produced defect-free and high-flux asymmetric cellulose acetate (CA) membranes for reverse osmosis using a phase inversion process. They consisted of an ultrathin, asymmetric, and selective surface (thickness $< 0,5 \mu\text{m}$ [3]) that was supported by a thicker and more permeable microporous structure (thickness 50-200 μm [3]) that offered the mechanical stability the ultrathin selective surface greatly needed. These membranes catalysed the research, production and commercial use of membranes utilised for various applications- from reverse osmosis, micro-, nano- and ultrafiltration, dialysis to gas permeation and pervaporation. The CA flat membranes performed ten times better than any available membrane at the time and displayed the great potential of reverse osmosis in the desalination of water [1]. Capillary membranes (outer diameter 300-1000 μm), used in hemodialysis, as well as tubular membranes (1-2 cm), used in ultrafiltration, were developed later on [2].

Membranes were simultaneously developed for medical separation processes in 1945, when the first artificial kidney was produced. A further 20 years would pass until the artificial kidney was refined, optimised, and applied on a large scale. Blood oxygenators and extracorporeal membrane oxygenators were similarly developed and played a significant role in open-heart and other critical surgeries. The demand for biocompatible membranes to be utilised in drug-delivery systems was another reason for the vast adoption of membranes in the biomedical and pharmaceutical fields [1].

By the early 1980s, micro-, ultrafiltration, reverse osmosis, and electro dialysis were all established and vastly applied processes. This decade marked the evolution of industrial gas separation and pervaporation processes. While gas separation technology is widely used and has and will continue to develop, pervaporation has not been as widely adopted. The mid-1990s marked the advancement of reliable and economically feasible micro-/ultrafiltration systems for water treatment and bioreactors in sewage plants [1]. A summary is provided in Table 1.

Table 1: Overview of Technical Membrane Processes [3]

Membrane Process	Country	Year	Application
Microfiltration	Germany	1920	Laboratory use (bacteria filter)
Ultrafiltration	Netherlands	1930	Laboratory use
Hemodialysis	USA	1950	Artificial kidney
Electrodialysis	USA	1955	Desalination of seawater
Reverse osmosis	USA	1960	Desalination
Ultrafiltration	USA	1960	Concentration of macromolecules
Gas separation	USA	1979	Hydrogen recovery
Membrane distillation	Germany	1981	Concentration of aqueous solutions

Of the greater interest here are the invention, manufacture and the variety of parameters that influence asymmetric membranes. In this thesis, the focus lies on polymeric asymmetric hollow fibre membranes. Polymeric hollow fibre membranes were first patented 50 years ago by Mahon and are beneficial in their separation performances as compared to other membrane configurations. Among some of their advantages, the shape and geometry of the hollow fibre provide a greater membrane area, and they can be much densely packed into modules. Additionally, hollow fibres tend to be mechanically relatively stable and provide for more uncomplicated handling and utilisation [1], [4], [5]. The general principle of the functionality of membranes will be further explored in later units.

The importance of the experimentation, production and end application of such membranes cannot be understated- biocompatible membranes have and are capable of significantly and sustainably improving not only the biomedical field but also the quality and standard of life for the average person. Additionally, membrane separation technology, in general, brings with itself a modern era of growing sustainable treatments of living beings, wastewater, solid waste, heavy metals etc.

1.2 Aim and Motivation

The crux behind this thesis is to explore and document the manufacture, production, utilisation, and application of polymeric asymmetric hollow fibre membranes using the newly built in-house NIPS process plant (Institute of Chemical, Environmental and Bioscience Engineering, Research Group E166-02-2). During the manufacturing process (which can vary based on the application of the fibres), several parameters come into play and display their role in the fibres' characteristics, morphology, and separation performance. In this thesis, the focus lies on the process of nonsolvent induced phase separation (NIPS) to produce biocompatible novel hollow fibre membranes out of polyethersulfone (PES) for ultrafiltration/gas separation processes. This polymer was used for its ideal properties and characteristics in making ultrafiltration hollow fibre membranes and its superior biocompatibility [6]–[9]. In its terse definition, biocompatibility is the capability of a material to perform with an appropriate and safe host response in a specific situation [9], [10]. PES exhibits excellent biocompatibility, thus being an excellent choice for membrane production employed in biomedical applications.

1.3 Structure of This Thesis

The next chapter explores the theoretical framework of how membranes function and the varying aspects of their application and utilisation. This chapter will also take an in-depth look at hollow fibre membranes and their past and current experimental and large-scale production, application, and modifications. This lays the theoretical foundation and literature overview for the setup and experimentation performed in this thesis.

Next, this thesis dives into the experimental setup, parameters that influence the properties of the hollow fibres, the module building and ultrafiltration setups, and the tests and experimentation carried out in the laboratory. This chapter is followed by the results of the many tests accomplished, the discussion and interpretation of the varied

parameters and their respective outcomes in membrane performance. The influence of each parameter on the fibre's characteristics, selectivity, permeance, morphology, porosity and mechanical stability will be discussed. Specific trends will also be interpreted using the Design of Experiment method.

Lastly, this thesis serves as a literature overview and explores further the functionality, application, and optimisation of the NIPS process plant to produce hollow fibre membranes. Membrane technology has paced several breakthroughs over the years. It displays excellent potential as a sustainable method in the biomedical fields and the environmental future of this planet. Therefore, this thesis applies proven techniques and provides a starting base for further research and the application of biocompatible hollow fibre membranes.

2 Review of Literature and Theoretical Framework

2.1 The Membrane

Before diving into the specifics and details about the functionality, manufacture and application of membranes and membrane processes, the definition of a membrane at its core must be explained. A membrane is an all-encompassing object applied in different fields and thus can vary in its definition and function based on the domain it is used in. Therefore, having discussed the history of membrane technology in the previous unit, an overview of such an expansive definition must be achieved before embarking on the vast membrane separation technology journey.

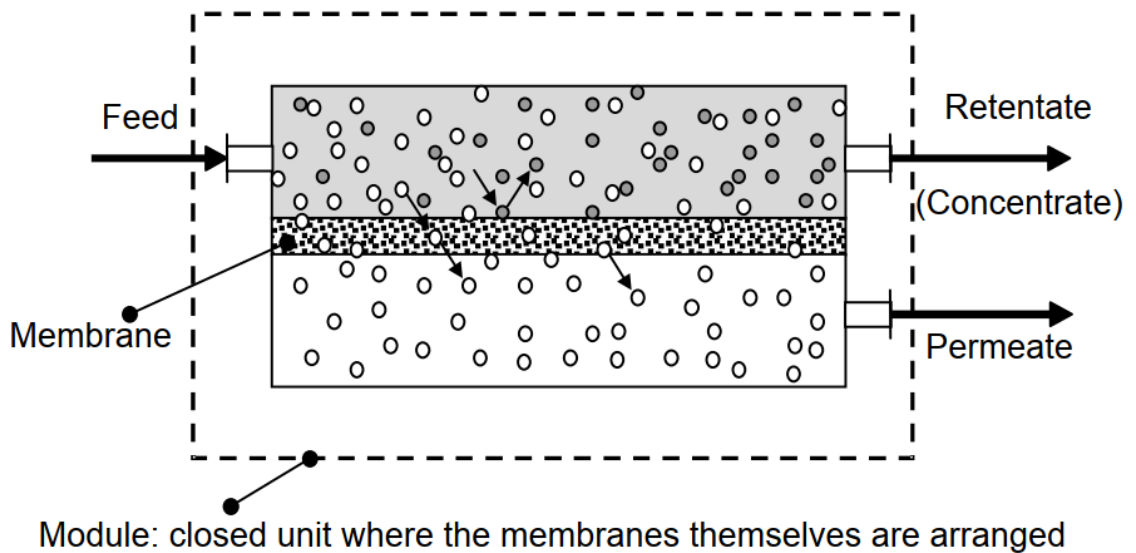


Figure 2: Fundamental basis of a porous membrane system; adapted from [11]

In its most general form, a membrane is a semi-permeable barrier that separates two phases and selectively impedes and controls the transport between these two phases [2], [3], [12]. To effectively transport and control the flow of the feed (the solution/mixture etc., to be separated in Figure 2), there needs to be a driving force acting on the components. Different components exhibit different transport rates through the membrane due to the driving force and the permeability of the membrane itself [2], [3]. The transport rate of a component is inversely proportional to the

membrane thickness. It is directly related to the driving force in a linear relationship, as shown in Equation 1 [2], [3]. In general terms, the flux J can be described by a linear phenomenological function [3]:

$$J = -A \frac{dX}{dx}$$

Equation 1: Proportionality between flux J and the driving force $\frac{dX}{dx}$; A is the phenomenological coefficient [3]

$\frac{dX}{dx}$ is described as the gradient of X (pressure, concentration, temperature etc.) along the coordinate x normal to the membrane. With a more detailed outlook, the flux of a component through a membrane can be described as:

$$J_i = \frac{P_i}{\Delta z} X_i$$

Equation 2: Flux through a membrane of component i : transmembrane flux J , permeability coefficient of the membrane P , driving force X , membrane thickness Δz [2]

Figure 2 depicts a typical separation process, where a porous membrane separates two components from each other. These can be liquids or gases, or both. The feed, in this case, consists of components A and B, and it can be assumed that the flux of component A through the membrane is much higher than the flux for component B. Therefore, a separation is achieved, and a permeate fortified with A and a retentate enriched in B are obtained. This selective property of a membrane to distinguish between two components is called selectivity and is a defining characteristic for a membrane and can be written with either mole fractions or weight fractions [2], [11]. Selectivity of component A, which is a dimensionless parameter, can be defined by:

$$S_{AB} = \frac{\frac{y_A}{1-y_A}}{\frac{x_A}{1-x_A}} = \frac{\frac{y_A}{y_B}}{\frac{x_A}{x_B}}$$

Equation 3: Selectivity of component A; mole fraction of A in permeate y_A , the mole fraction of B in permeate y_B , mole fraction of A in feed x_A , mole fraction of B in feed x_B [11]

Another determining factor for a membrane is the separation factor α and can be expressed by [2], [11]:

$$\alpha_{AB} = \frac{y_A x_B}{x_A y_B}$$

Equation 4: Separation factor α ; mole fraction of A in permeate y_A , mole fraction of B in permeate y_B , mole fraction of A in feed x_A , mole fraction of B in feed x_B [2], [11]

The separation factor is a dimensionless parameter and can take up values of anywhere between 1 and infinity. For $\alpha_{AB} > 1$, the permeation rate for component A is much higher than for component B. However, if the separation factor equals 1, the membrane shows no selectivity for the component, and therefore no separation is possible. With increasing numbers of the separation factor (reaching closer to infinity), the membrane can better permeate A so B is completely retained.

Lastly, the rejection of a membrane is another essential property of a membrane. For dilute solutions comprising of a solute and solvent, it is a handy characteristic to define selectivity in terms of rejection for the solute. [2], [11] The rejection is another dimensionless parameter. It varies between zero and one- zero for a membrane with no selectivity and one for an ideal permeable membrane. It is defined by:

$$R_A = 1 - \frac{C_A^p}{C_A^f}$$

Equation 5: Rejection of component A by the membrane: concentration of A in permeate C_A^p , concentration of A in feed C_A^f [2], [11]

As already stated, a membrane can take on many different forms for many different purposes. Membranes can vary in [1]–[3], [11]–[14]:

- i. their thickness
- ii. their structure (defined pores/heterogeneous or dense homogenous; symmetric/asymmetric)
- iii. their phase (solid/liquid/gel)
- iv. their components (organic/inorganic/metallic)
- v. their geometry (flat sheets/tubes/capillaries/hollow fibres)
- vi. their charge (neutral/positive/negative/bipolar)
- vii. the type of transport (convection/diffusion)
- viii. the driving force that leads to the transport through a membrane (electric field/concentration/pressure/temperature gradient)
- ix. the separation processes

The most straightforward distinction made by modern literature [1]–[3], [11]–[14], however, is the classification between synthetic and biological membranes, since these two classes of membrane function and appear utterly different to each other. In this thesis, however, the focus lies solely on synthetic membranes. The following figure summarises just one way of classifying membranes into synthetic and biological classifications and other specific classes.

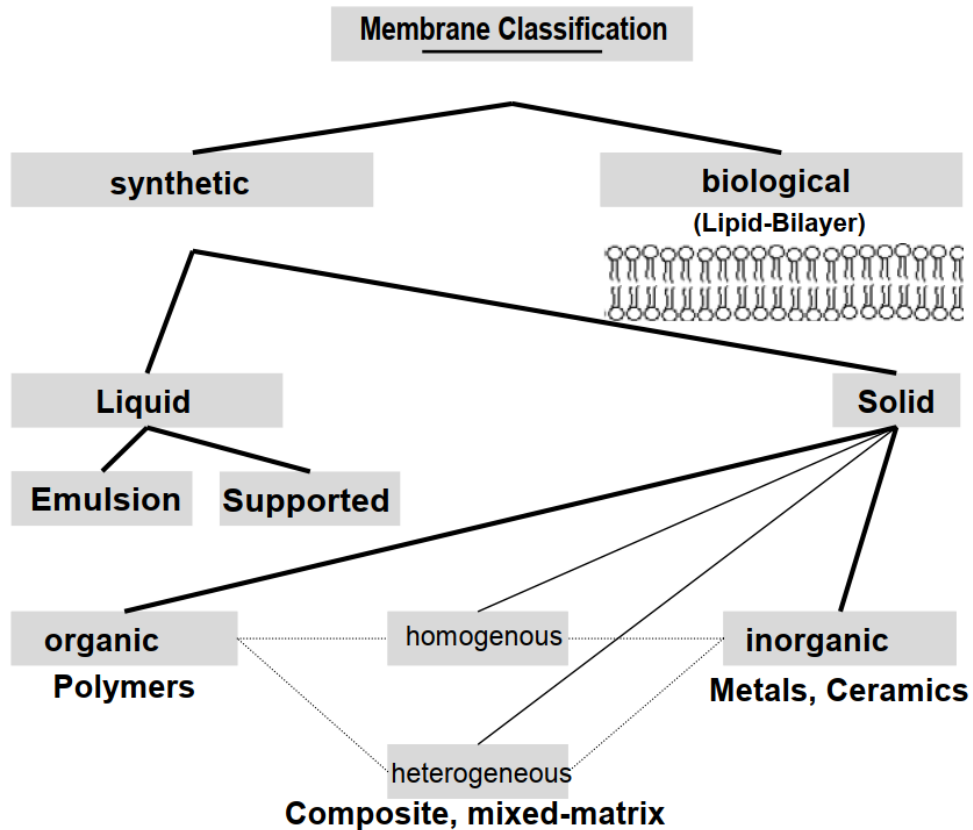


Figure 3: One means of classifying membranes; adapted from [11]

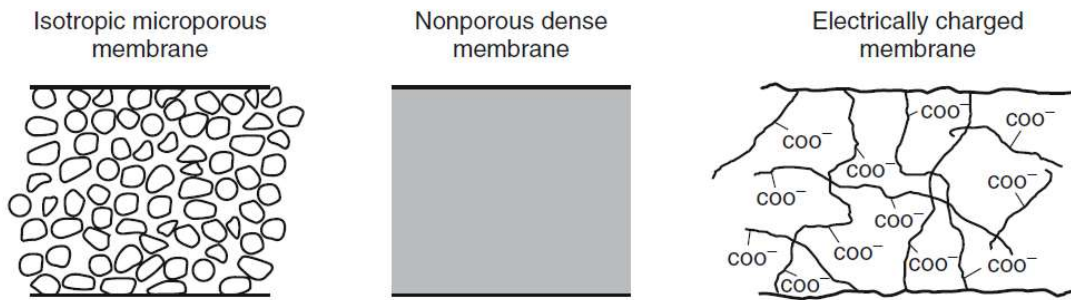
2.1.1 Classification Based on Structure

Figure 3 is not the only way of distinguishing between different membranes. A second means of organising membranes is by their structure. The morphology of the membrane plays an essential role in the separation technique displayed by the membrane. Figure 4 depicts a schematic representation of this means of classification. Membranes can be classified into either the symmetric/isotropic or asymmetric/anisotropic categories.

Symmetric membranes typically display a direct proportionality between their flux and thickness. The structure and transport properties remain constant over the entire cross-section. They find their function primarily in dialysis and electro dialysis [2], [3]. Several techniques can be found in literature [14] that are and can be used currently to produce symmetric membranes: irradiation-etching, TIPS (temperature-induced phase separation), VIPS (vapour induced phase separation), stretching and precipitation from a vapour phase.

On the other hand, asymmetric membranes consist of a relatively thick selective skin layer (0,1-5 µm) and a highly porous and dense substructure (100-300 µm). The separation properties of such a membrane are determined by the material or the pore sizes of the selective skin barrier. In contrast, the porous underlayer only serves as a stable mechanical support for the fragile skin layer. It does not influence the flux, mass transfer rate and transport characteristics of the membrane. The transport rate of a specific substance is, in this case, inversely proportional to the membrane thickness [1]. Due to their stable mechanical properties and high fluxes, these membranes are utilised in pressure-driven processes such as reverse osmosis, ultrafiltration, gas separation, and microfiltration.

Symmetrical Membranes



Anisotropic Membranes

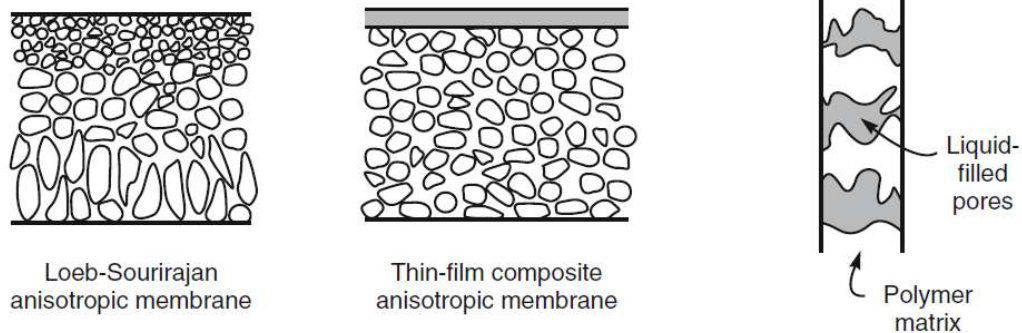


Figure 4: Schematic diagrams of various membranes (classified by their structure and morphology) [1]

Although multiple production techniques for asymmetric membranes have been developed, two stand out the most [2]:

- i. phase inversion that results in a membrane where the skin and the support structure are both made of the same material in a one-step process (this technique is further explored in this thesis)
- ii. phase inversion that results in a composite structure where a thin semi-permeable layer consisting of one material is deposited on a porous substructure made from another different material in a two-step-process

Another way a membrane can be classified by their structure is if they are porous or nonporous. Porous membranes are defined by their polymer phases and interconnected pores that serve as transport passages [14]. These defined pores display diameters of <1 nm and >10 μm and determine the type of membrane process it can be used for. Figure 5 shows the defining pore sizes of the three main types of porous membranes. Porous membranes can be symmetric (constant pore diameters over the cross-section) and asymmetric (increasing pore diameter from one side of the membrane to another). They can be produced from multiple materials such as ceramics, graphite, metal/metal oxides, and polymers. Their production methods vary widely from simple pressing and sintering to irradiation and leaching to phase inversion techniques [2]. Porous membranes are usually utilised to separate components characterised by a wide range in size or molecular weight in micro-, ultrafiltration and dialysis [2], [14].

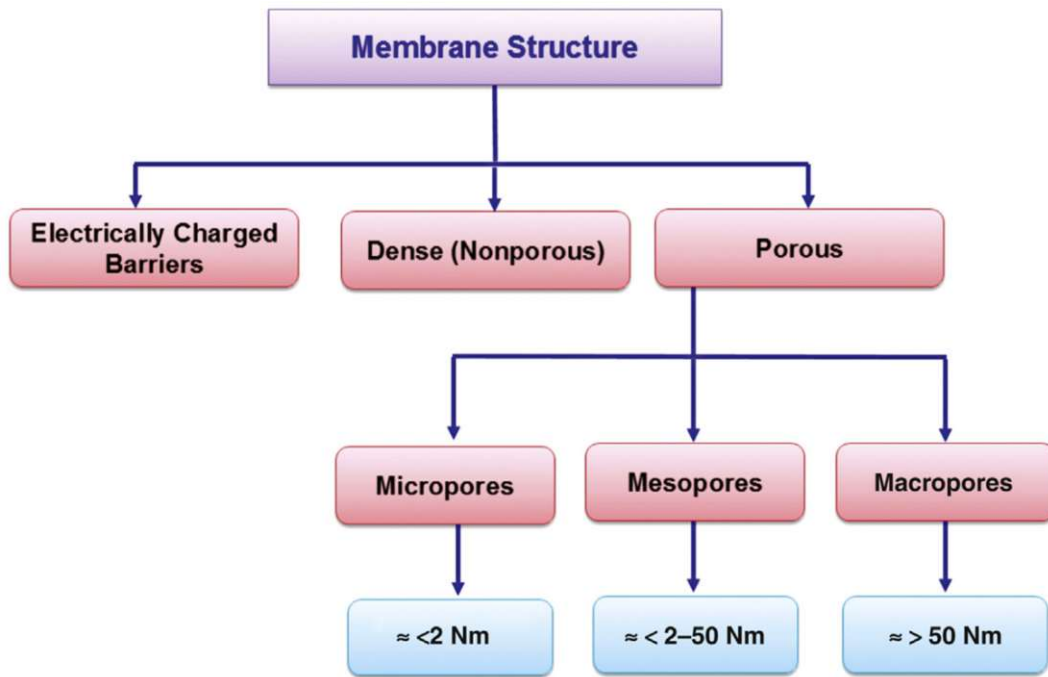


Figure 5: Membrane structure classification: pore size of the three main types of porous membranes [14]

On the other hand, nonporous membranes can be characterised by the layers of closely packed polymer chains that form a continuous phase with a continuous and constant packing density throughout the membrane [14].

2.1.2 Classification Based on Geometry

Membranes can be classified based on the geometry with which they are produced. There are a few geometries that are widespread and applied in the industry. The geometry and shape of the membrane to be used is dependent not only on the application but also on its performance, manufacturing and operating costs [1], [2]. The geometry of the membranes also determines the type of device the membranes are packaged in as well. The most used membrane geometries are outlined in Figure 6.

Flat sheet membranes can be symmetric or asymmetric and are supported by a porous polyester fibre felt paper for added mechanical strength and stability. Hollow fibre membranes with outer diameters ranging from 0,05-0,5 mm are usually asymmetric. Mass transport is typically carried out from the outside (shell side) into the lumen of the fibre. Capillary membranes are like hollow fibre membranes in terms of shape and geometry. However, they are much larger. The selective skin is usually found inside the capillary (the hollow fibre membranes, where the selective skin is located on the outside surface). Mass transport here occurs from within the lumen to the outside. A step larger and one finds tubular membranes, which resemble large tubes. A porous plastic or steel tube provides support, and the feed stream is always introduced in the lumen of the membrane [1], [2], [14]–[16].

The devices into which multiple membranes are installed are referred to as modules. These membrane geometries are packaged into the appropriate modules for optimal performance, cost, and utilisation and attain multiple properties such as hydrodynamic conditions, energy usages, filtration areas etc. These modules work as a way to separate the feed stream into permeate and retentate streams [1], [2], [14].

Based on the membrane geometries and many other parameters (some of which are listed in Table 2) necessary for module design, the appropriate module can be chosen. Table 2 summarises briefly the differences and the set-ups of each commercially utilised module.

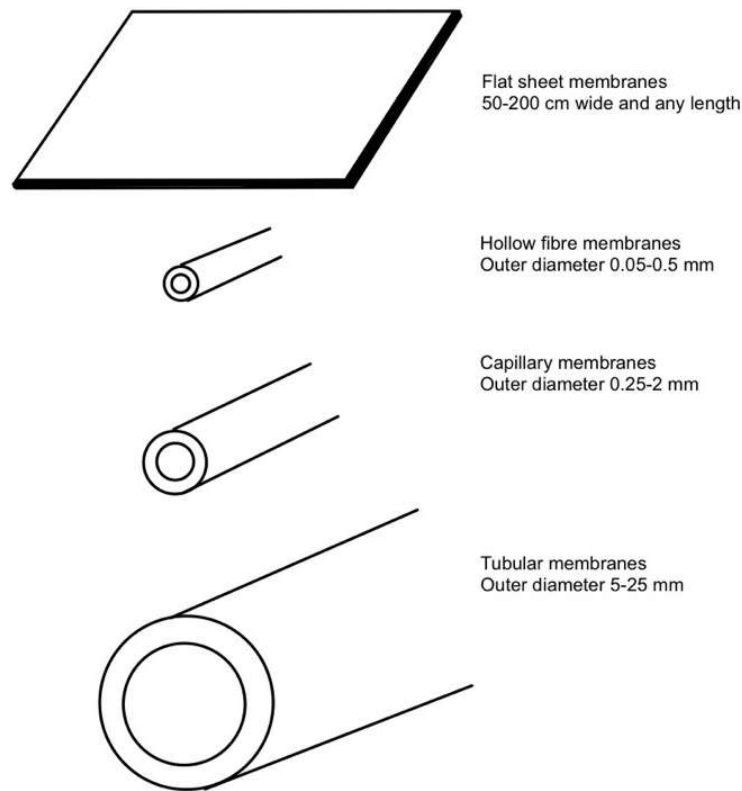


Figure 6: Four standard technically relevant membrane geometries; adapted from [2]

2.1.3 Classification Based on Configuration

Membrane processes and modules can be utilised in two main configurations—dead-end and crossflow configurations (Figure 7). In the crossflow configuration, the feed stream flows parallel to the membrane surface, the permeate permeates through the membrane at a pressure difference and the retentate is removed from the same side as the feed stream [3], [14]–[16]. A cross-flow configuration is widely used for industrial purposes as this configuration yields less fouling as compared to the dead-end configuration [3]. The most common modules operated in such configuration are the hollow fibre, tubular, flat-plate, and spiral-wound modules. However, these modules can also be utilised with the dead-end configuration as well [14], [16].

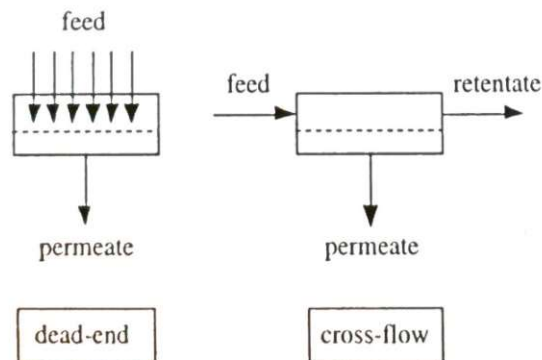


Figure 7: Schematic depiction of two basic module configurations [3]

A dead-end configuration is characterised by the fact that the feed stream flows through the membrane pores (normal to the membrane surface) due to a pressure being applied on the feed side [3], [11], [14], [16]. Due to such an operation, the concentration of the undesired components (the components that would be the retentate stream) in the permeate increases over time, thus decreasing the quality of the permeate, as shown in Figure 8 [3]. Unique module designs have been developed especially for this configuration- syringe-end filters, centrifugal machines and vacuum filtration devices all are applied as disposable systems so as to avoid the extra step of cleaning, which is a disadvantage when using the standard module designs [14], [16].

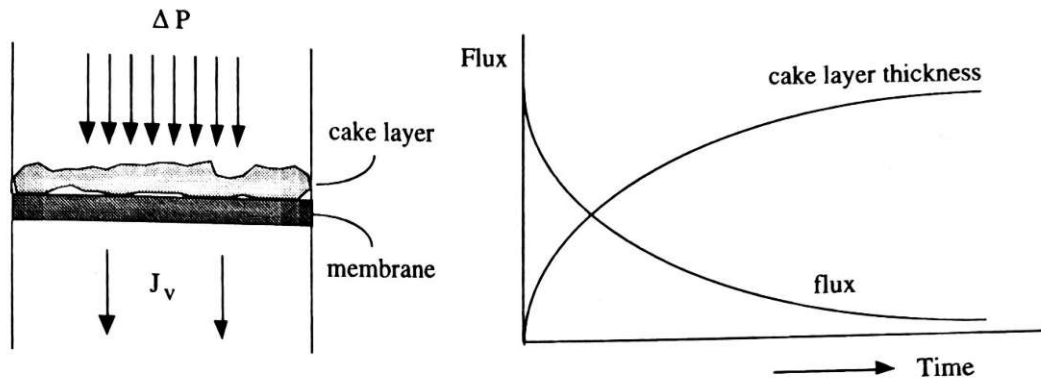


Figure 8: Flux decline in a dead-end configuration in filtration processes [3]

Figure 10 illustrates the five technically relevant module designs applied in the laboratory small-scale experimentation and production and large-scale industry manufacture. As is apparent by the differing geometries and properties of each module design, each finds its purpose in different membrane processes and functions. Some of the characteristics of module design are outlined in Table 2.

2.1.4 Classification Based on Separation Techniques: Pressure-driven Membrane Separation Processes

Amongst the many membrane separation processes that have been developed over the years (as explained in 1.1), the few most important and widely used and applied procedures are summarised in Table 3. As is evident in Table 3, membrane processes require a driving force and a transport mechanism through which the fluid molecules to be separated travel through the membrane. These transport models will be further explained later. However, it is essential to note that each process uniquely fulfils the need for separation in multiple ranges of molecular size, weight, etc.

While each of the membrane separation processes listed in Table 3 is important, and there are many more unique processes currently in use, this paper focuses on pressure-driven separation processes, especially ultrafiltration and gas separation. Table 4 summarises the four central pressure-driven separation processes as well as their applications. Such pressure-driven separation processes are usually utilised for the concentration/purification of dilute solutions, where the solvent is the continuous fluid phase and solute concentrations are generally low. A pressure difference characterises these processes as the driving force and the inverse proportional relationship between the flux across the membrane and the membrane thickness [3].

Each of these four separation processes separates using a different mechanism. This principle of size exclusion through the sieving effect can be seen in many pressure-driven processes. However, the difference lies between the structure

and pore size of the membranes as well as the pressure at which these processes are operated at [1], [2], [13], [14].

The ultrafiltration (UF) separation process lies in between the microfiltration (MF) and nanofiltration (NF) processes due to the range of the molecular weight and size of the separated components, the applied hydrostatic pressures, and the type of membrane used, as shown in Table 4 [3]. The UF process finds its utilisation mainly for the concentration of macromolecular solutions. In UF, larger macromolecules are separated from smaller molecules [11].

UF membranes are, as mentioned above, porous membranes, where the rejection/retention of a particle depends on its size and the structure relative to the size and structure of the pores of the membrane itself. In such porous membranes, the primary transportation method for materials is through convective material transport [1], [3], [11]. In such porous membranes, the primary transportation method for materials is through convective material transport [1], [3], [11].

UF membranes are characterised by the characteristic size of the molecular weight of the component to be rejected. This characteristic is called the solute MWCO (molecular weight cut-off). It is defined by the limit at which 90-95% of a specific molecule of a particular molecular weight is rejected [1], [11]. Another critical factor here, besides the size of the molecule, is the shape of the molecule. Depending on the condition of the molecule, different rejections are measured, as shown in Figure 9. Typical MWCO for UF membranes is between around 1000-10 000 Da [11].

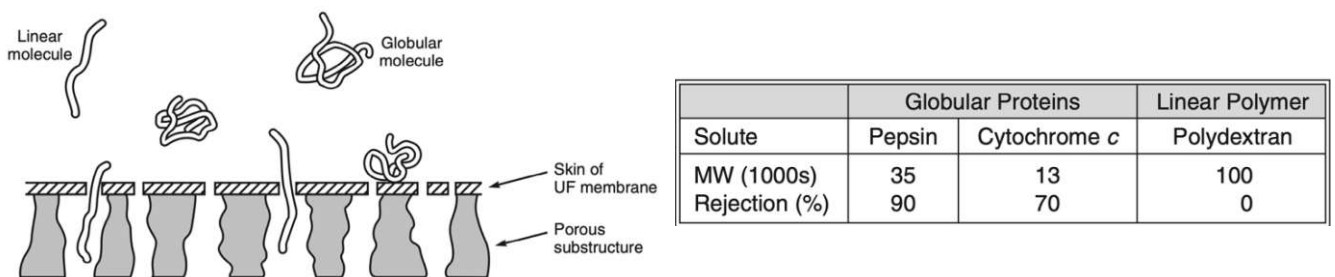


Figure 9: UF membranes are rated on the nominal MWCO, but the shape of the molecule also plays a massive role in the retentivity of the solute. Linear molecules are quickly passed, whereby globular modules of the same molecular weight may be rejected. The adjoining table shows typical results of testing globular protein and linear polydextran for a polysulfone membrane [1].

Another factor in the efficacy of UF membranes is the pH of the feed solution. The pH-value is attributed to a change in the configuration of, e.g., the polyacrylic acid. At higher pH values, the negatively charged carboxyl groups along the polymer repel each other, thus yielding an extended and inflexible molecule. At lower pH values, the carboxyl groups along the polymer backbone are all protonated, and thus the molecule is more flexible and can pass through the membrane pores [1].

Table 2: Some parameters for module design [1]–[3], [12], [14]–[16]

Parameter	Hollow fine fibres	Capillary fibres	Spiral-wound	Plate-and-frame	Tubular
Manufacturing cost (US\$/m ²)	5 to 20	10 to 50	5 to 100	5 to 200	5 to 200
Concentration polarization fouling control	Poor	Good	Moderate	Good	Very good
Permeate-side pressure drop	High	Moderate	Moderate	Low	Low
Suitability for high-pressure operation	Yes	No	Yes	Yes	Marginal
Limited to specific types of membrane material	Yes	Yes	No	No	No
Set-up	Loop or bundle of over a thousand hollow fibres with their ends potted in an epoxy resin in a pressure vessel	Similar to hollow fibre module	Plate-and-frame system wrapped around a perforated permeate collecting tube	Flat sheet membranes, support plates and spacers arranged on top of each other and stacked between two plates: feed stream flows across the membrane surface	Membranes inserted in pressure-tight stainless steel/fibre glass reinforced plastic tubes
Applications	Reverse osmosis desalination of seawater, gas separation	Artificial kidneys, microbiological water treatment, clarification of beverages and wastewater treatment, dialysis, micro- and ultrafiltration at low pressures	Reverse osmosis of seawater and brackish water desalination, ultrafiltration, and gas separation	Electrodialysis and pervaporation systems and in a limited capacity in reverse osmosis and ultrafiltration with highly fouling feed streams	Ultrafiltration at low pressures, in the food and pharmaceutical industry
Packing Density	Highest of all module types in the industry (500-10000 m ² /m ³)	High	Relatively high (>900 m ² /m ³)	100-400 m ² /m ³ possible	Low

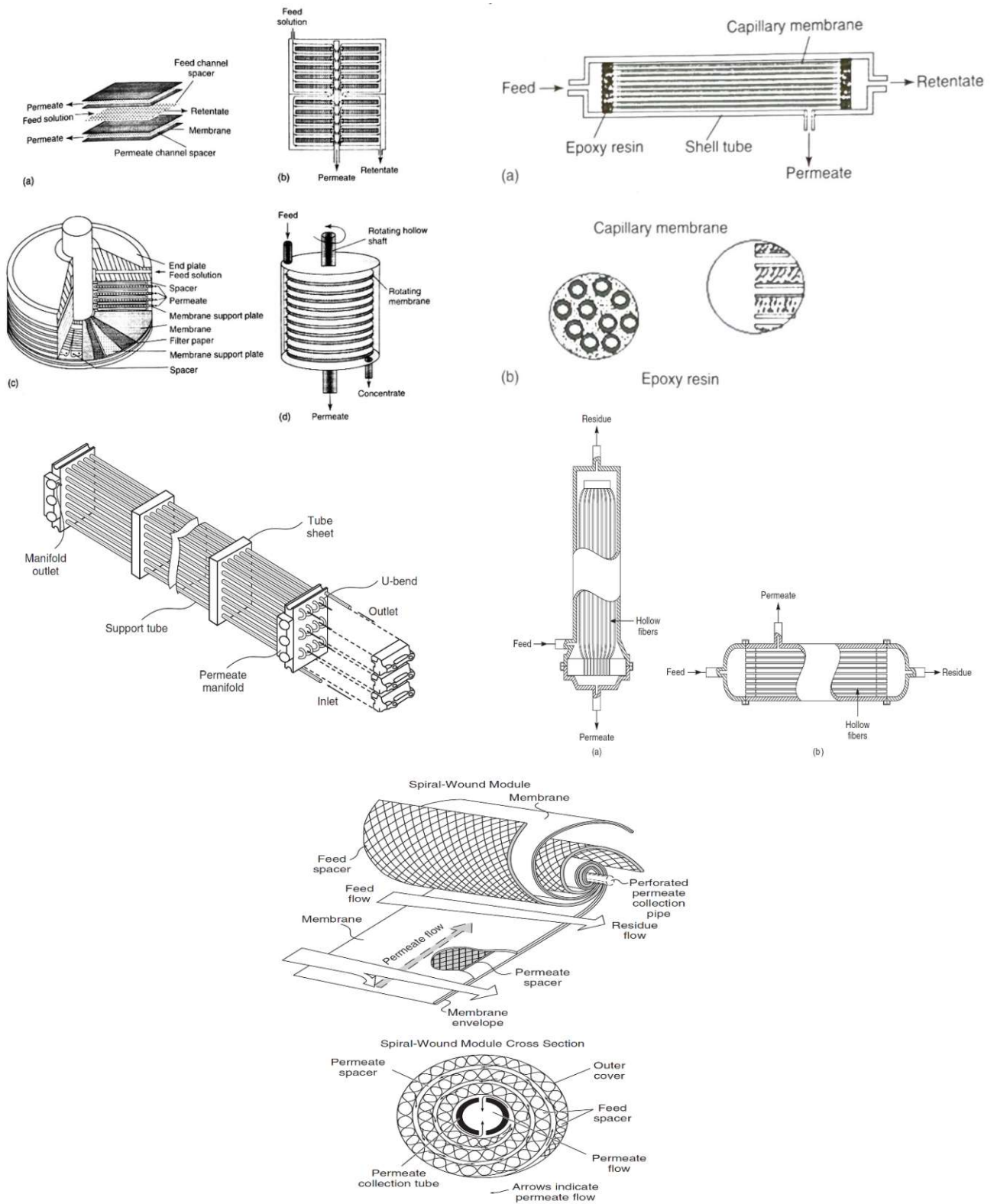


Figure 10: Top left: Plate-and-Frame module: a) components in flat sheet filtration modules; b) cross-section of flat sheet stack in a housing and the streams of feed, permeate and retentate; c) circular flat sheet module; d) rotating module design [2]; Top right: Capillary module: a) cross-section of the module; b) entrance/exit of the module where the membranes are potted in the shell tube [2]; Middle left: Tubular module with 30 tubes connected in series; permeate collected in permeate manifold [1]; Middle right: Two module designs for hollow fibre modules; a) shell-side feed modules; b) bore-side feed modules [1]; Bottom: Spiral-wound module; exploded and cross-section display; feed passes across the membrane surface where a portion enters the membrane envelope and flows towards the collection pipe [1]

The pore-flow model can be utilised to describe the flux in UF membranes (mesoporous structure). As a result of the tiny pores, especially on the surface, a non-negligible osmotic pressure difference and, therefore, a diffusive flux between the feed and filtrate can occur when the concentration in the feed/retentate is too high. The flux of individual components can be illustrated by the addition of the diffusive flux caused by the chemical potential gradient in the pores and a Poiseuille flow through the pore because of the pressure difference between the feed and filtrate solutions:

$$J = \sum_i J_i V_i = - \sum_i V_i L_i \frac{d\mu_i}{dz} - L_p \frac{dp}{dz} = - \sum_i V_i L_i \frac{d}{dz} (V_i p + RT \ln(a_i)) - L_p \frac{dp}{dz}$$

Equation 6: J and J_i: total volume flux and flux of component i; L_p and L_i: phenomenological coefficients referring to Poiseuille flow through the pores and diffusive flux in the pore; V_i: partial molar volume; μ_i: chemical potential; a_i: activity of component i; p: pressure; z: directional coordinate [2]

Assuming that the total volume flux of a dilute solution can be directly illustrated as the flux of only the solvent, the activity of the solvent as the osmotic pressure of the solution and a linear relationship between the pressure and activity gradient of the solvent across the membrane, integrating Equation 6 leads to [2]:

$$(a) \quad J = J_w = - V_w^2 L_w \frac{\Delta p - \Delta \pi}{\Delta z} - L_p \frac{dp}{dz}; (b) \quad J = - L_p \frac{\Delta p}{\Delta z}$$

Equation 7: (a) Flux through a UF membrane as a function of the pressure difference between feed and permeate, hydrodynamic permeability of Poiseuille flow, the osmotic pressure difference between feed and permeate and the phenomenological coefficient determining the diffusive flow of water through the pores; (b) simplified total volume flux [2]

In practical UF processes, the flux is simplified as the osmotic water transport is only an influential parameter for the volume flux only when the osmotic pressure difference is higher than the hydrostatic pressure difference, which only occurs in UF solutions of high concentrations of retained components of low molecular weight (seldom the case) [2].

This, however, cannot be done for solute transport as the diffusive flux does play a role:

$$J_i = J C_i^p = - L_i \frac{d}{dz} (V_i p + RT \ln(a_i)) - L_p C_i^m \frac{dp}{dz}$$

for pressure differences in UF: $V_i p \ll RT \ln(a_i)$

Equation 8: Flux of solute through the membrane described by the summation of the diffusive flux due to chemical potential and convective flux due to concentration in the pore solution; C_i^m: solute concentration in pore solution; C_i^p: solute concentration in permeate [2]

Assuming that the solutes' activity coefficients in the membrane are 1, then Fick's diffusion coefficient can be used to illustrate the phenomenological coefficient. Integrating this leads to [2]:

$$J_i = J \frac{C_i^{m,f} \exp \frac{J\tau\Delta Z}{D_i^m} - C_i^{m,p}}{\exp \frac{J\tau\Delta Z}{D_i^m} - 1}$$

Equation 9: Flux of component i consists of Poiseuille flow term (linear relationship with pressure) and of diffusion term in the pore liquid (exponential relationship with pressure); J: flux; C: concentration; D: Diffusion coefficient; τ : tortuosity; ΔZ : membrane thickness; superscripts m, f and p refer to the membrane, solution in the membrane at feed side, solution in the membrane at permeate side [2]

Thus, it can be deduced that two limiting cases can be established for the transport mechanism for UF processes. The first describes the case where the pressure and therefore viscous flow (Poiseuille flow) is zero and thus solute transport only occurs by diffusion only [2].

$$\lim_J J_i = 0$$

Equation 10: First limiting case where the pressure and viscous flow are zero [2]

The second describes precisely the opposite case- infinitely high pressure and viscous flow. Thus, solute transport is driven by its concentration in the membrane [2].

$$\lim_J J_i = J C_i^p$$

Equation 11: Second limiting case where the pressure and viscous flow are infinitely high [2]

As mentioned in Equation 5, the rejection of a UF is a function of the concentration of the component in the permeate to that in the feed. It is, however, also a function of applied pressure as the solute flux in UF membranes is a function of viscous flow and diffusion. Thus, the rejection can be expressed as [2]:

$$R_i = \left(1 - \frac{C_i^p}{C_i^f}\right) = \left(1 - \frac{J_i}{J C_i^f}\right)$$

Equation 12: R: rejection coefficient; C: concentration; superscripts f and p refer to feed and permeate [1], [2], [11]

Combining Equation 9 and Equation 12 together provides:

$$R_i = 1 - \frac{k^f \exp \frac{J\tau\Delta Z}{D_i^m}}{k^p - 1 + \exp \frac{J\tau\Delta Z}{D_i^m}}; k^f = \frac{C_i^{m,f}}{C_i^f}; k^p = \frac{C_i^{m,p}}{C_i^p}$$

Equation 13: Rejection expressed as relationships with solute concentrations in feed, permeate and membranes; k^f and k^p : partition coefficients [2]

The role hydrostatic pressure plays in the retention of UF membranes is more evident when two extreme cases are handled. At large Δp and therefore high viscous flows, the retention approaches a maximum defined as the partition coefficient of the solute between the membrane and solution. At low Δp , retention goes to zero [2].

$$\lim_{J \rightarrow \infty} R = 1 - k^f; \lim_{J \rightarrow 0} R = 0$$

Equation 14: At high hydrostatic pressure, rejection approaches the distribution coefficient; at low hydrostatic pressure, the rejection approaches zero [2]

However, in almost all UF processes, the diffusive flow can be neglected, and the volume flux is directly proportional to the hydrostatic pressure. Rejection of UF membranes does not depend on the applied pressure either [2]. It is still a challenge to model flux in asymmetric UF membranes in terms of membrane porosity, pore radius and membrane thickness since these aspects change across the membrane. The thickness of the selective skin layer is also challenging to calculate. Much experimental work, modelling, and simulation are still required to model mass transport and flux in asymmetric membranes accurately.

2.1.5 Classification Based on Transport Model

The crucial role of a membrane in selectivity and its ability to separate components has already been previously mentioned, as well as the fact that a driving force is necessary to determine the separation of one component from the other. This imperative aspect of membrane technology will be tackled next- the transport theory and modelling behind permeation mechanisms through the membrane. The two main types of transport models are the pore-flow model and the solute diffusion model. As shown in Figure 12, it is possible to find a combination of these two models, depending on the pore diameter, the molecular diameter of the solute and the free path that is available to the molecules [1], [3], [11], [17].

Table 3: Membrane Separation Processes [1]–[3], [12]–[14], [18], [19]

Membrane separation process	Driving force	Membrane structure	Transport mechanism	Membrane material	Pore Size [nm]
Microfiltration	Pressure-driven (hydrostatic pressure)	Macroporous	Viscous flow	Polymer, ceramic, metal	50-10000
Ultrafiltration		Mesoporous	Viscous flow; diffusion	Polymer, ceramic	1-100
Nanofiltration		Microporous	Diffusion	Polymer, ceramic	0,5-5
Reverse osmosis		Dense	Diffusion	Polymer	<1
Dialysis	Concentration gradient	Dense, microporous	Diffusion	Polymer	<1
Electrodialysis	Electrical potential gradient	Dense, with electric charges	Diffusion; Selective ion-transport according to electric charge	Polymer	<1
Supported liquid membrane	Concentration gradient	Microporous	Solution-diffusion	Polymer	<1
Gas separation	Pressure gradient	Dense/porous	Diffusion; Knudsen	Polymer, ceramic	<1
Membrane distillation	Temperature gradient	Microporous	Vapour transport	Polymer, ceramic	<1
Pervaporation	Vapour pressure gradient	Dense	Diffusion	Polymer, ceramic	<1

Table 4: Pressure-Driven Membrane Separation Processes [1]–[3], [11], [13], [14], [18], [19]

Membrane process	Transmembrane pressure [bar]	Water permeability [L/m ² /h/bar]	MWCO [Da]	Components removed	Pore size [nm]	Permeate
Microfiltration	0,1-2	>500	-	Bacteria, algae, suspended solids	50-10000	Substances dissolved in solution, water
Ultrafiltration	1-5	20-500	1000-300000	Bacteria, viruses, colloids, proteins, macromolecules	1-100	Small molecules, water
Nanofiltration	5-20	5,0-50	>100	Di- and multivalent ions, molecules of low molecular weight, dissociated acids, natural organic matter, small organic molecules, micropollutants	0,5-5	Monovalent ions, nondissociated acids, water
Reverse osmosis	10-100	0,5-10	>10	dissolved ions, hardness	<1	Water

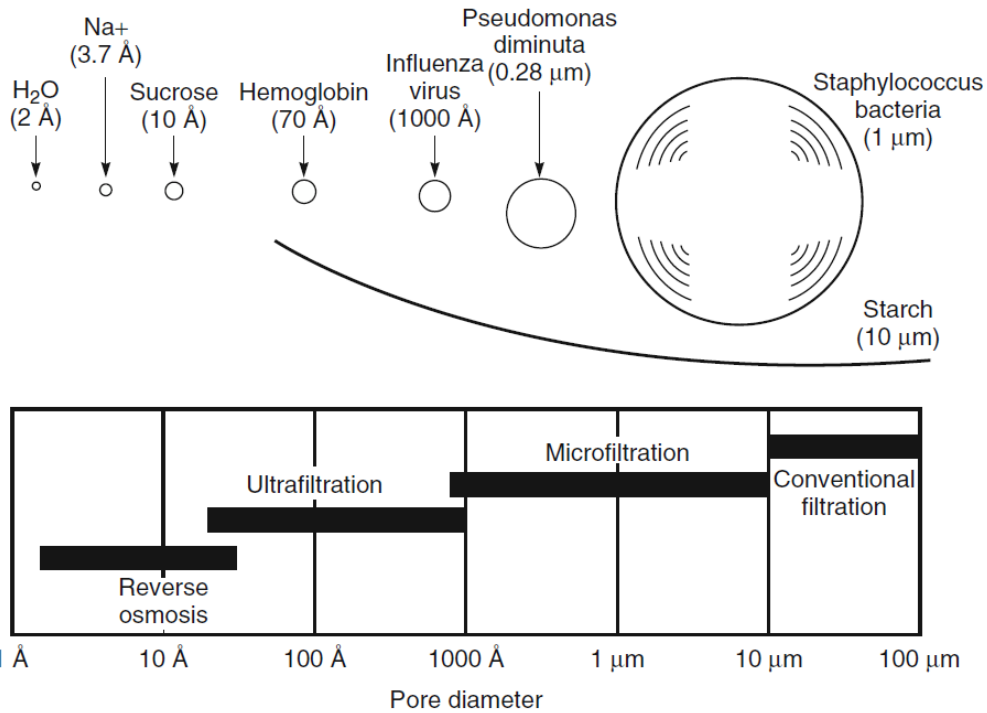


Figure 11: RO, UF, MF and filtration are similar pressure-driven processes, basically differing in the average pore size of the membrane. Discrete pores do not exist in RO membranes, and therefore mass transport happens through statistically distributed free volume areas [1]

The pore-flow model describes the transport of the permeate through pressure-driven convective flow through the pores of the membrane matrix. In contrast, the solute diffusion model depicts the concentration-driven permeate transport as the dissolution and diffusion of the molecules in the membrane matrix. While in the former model, separation occurs due to the filtration of some of the components from some of the pores in the membrane matrix. In the latter, separation occurs due to differences in solubilities and rates of diffusion of each component through the membrane [1].

It is imperative to understand that such models have been mathematically/empirically tested and, as such, have been derived from extensive experimentation, mathematical modelling, and simulation. Laws of conservation for mass, impulse, energy, components etc., are crucial for the design and optimisation of membrane processes. These equations need to be used in their differential form to account for local changes in temperature, concentration, and mass flows. They are not enough to design a membrane process accurately. Other equations and relationships describe the dependence of material transport through the membrane on operating conditions such as pressure, temperature, concentration, and external conditions, e.g., velocity [11].

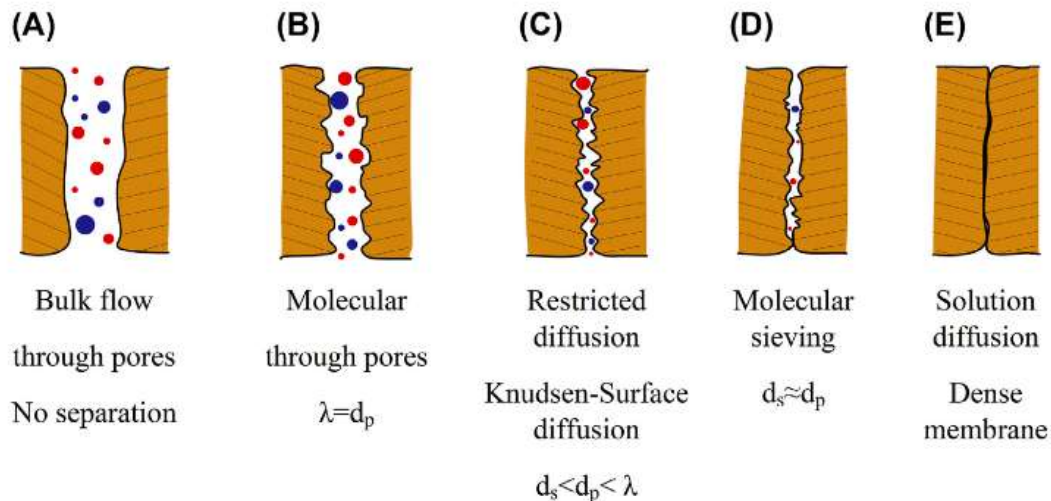


Figure 12: Differing transport mechanisms dependent on pore size within the membrane matrix [17]; d_p : pore diameter; d_s : molar size of solute; λ : free path of solute molecules

As this thesis focuses on UF membranes and their manufacture and application, the transport mechanisms involved will be expressly focused on transport models through porous membranes. Unlike the unified view and approach that has been vastly researched for dense membranes for use cases like reverse osmosis, pervaporation and gas separation, there is. Unfortunately, no singular direction to porous membranes as these sorts of membranes vary vastly in their heterogeneous nature, porous structure, and separation mechanism [1]–[3]. This is evident in Figure 13, where the different models are necessary for differing pore geometries.

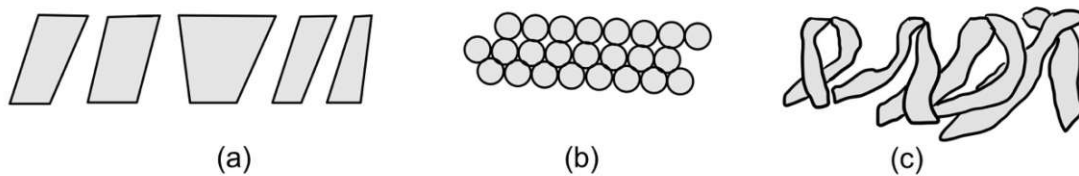


Figure 13: Characteristic pore geometries found in porous membranes [3]

Numerous assumptions need to be considered to determine the pore size and geometry. This characteristic of a membrane can wildly vary between the membrane matrix itself and among UF membranes. Initially, certain phenomena like pore blockage and creation of a top skin layer (the retained components build a deposit on the membrane that directly affects the flow and separation characteristics of the membrane) are to be neglected in this case to be able to model an ideal process [3], [11]. [3], [11].

Additionally, two key parameters utilised to describe the porous membranes are not always able to perfectly describe the complexities of the membranes. One such parameter is membrane porosity, ε defined by the porous fraction of the total membrane volume. Typically, parts of the membranes are weighed before and after their pores are filled with an inert liquid such as water, isopropanol etc. Such membranes used for UF purposes depict average porosities of 0,3-0,7. However, this provides a somewhat flawed impression of the membrane's porosity, as the porosity can vary from place to place on the membrane. Additionally, in asymmetric membranes, the porosity of the selective layer (skin layer) can be magnitudes smaller than the porous structure underneath. The second parameter is the membrane

tortuosity, τ which expresses the ratio of the average pore length to the membrane thickness. Cylindrical pores at right angles to the membrane surface naturally have a tortuosity of 1, which is rather uncommon as most pores do not perfectly go parallel down the membrane but rather wander their way through the matrix. Typical tortuosities range from 1,5 to 2,5 [1].

Among porous membranes, there are two general categories in how the solute molecules are filtered. The first category is the surface/screen filter, where the surface pores of the membrane are smaller than the molecules to be retained. Anisotropic membranes are a classic member of this category as they have a fine porous skin layer supported by an open porous support layer. Particles that pass through the selective skin layer usually pass through the porous support structure with little to no resistance. Particles larger than the pores on the skin layer are retained and accumulate on the membrane surface. The second category is defined by the fact that the particles to be retained remain in the inside of the membrane. Such membranes are called depth filters, and the average pore diameter is usually ten times the diameter of the smallest porous particle. While depth filters are usually microfiltration membranes, most screen filters are ultrafiltration membranes [1].

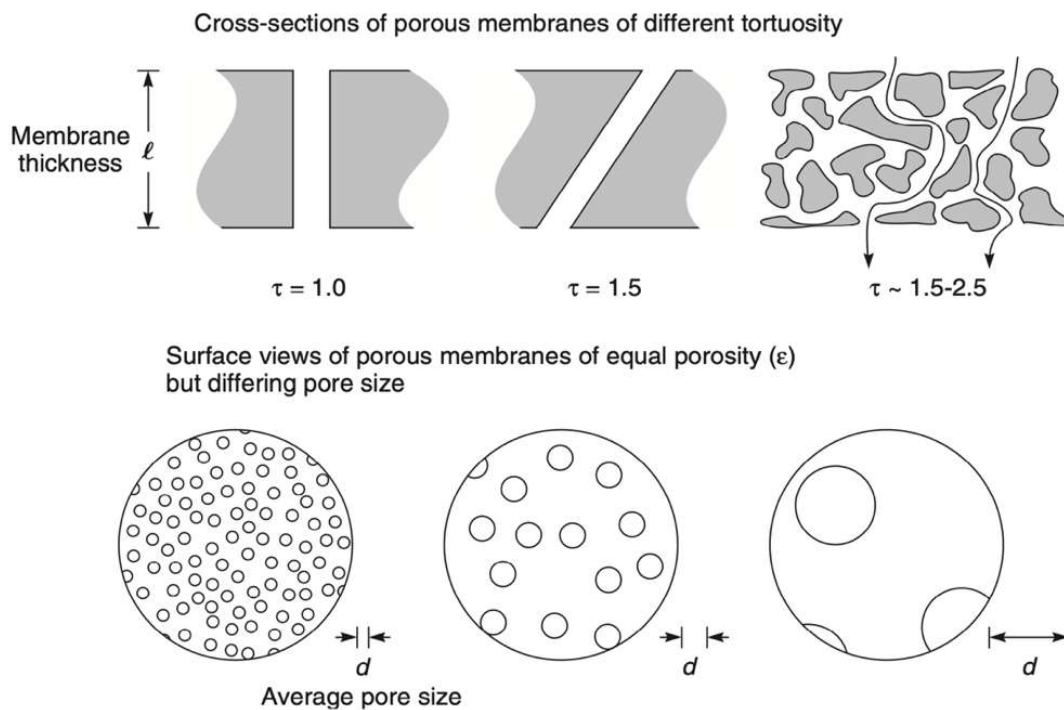


Figure 14: Porous membranes characterisation by their tortuosity, porosity, and average pore diameter [1]

As shown in Figure 13a, the most straightforward representation is where the membrane consists of multiple parallel cylindrical pores perpendicular or oblique to the membrane surface. The length of the pores is analogous to the membrane thickness. Using the Hagen-Poiseuille equation, the volume flux through the pores can be described by [3]:

$$J = \frac{\epsilon r^2 \Delta P}{8\eta\tau \Delta x}$$

Equation 15: Volume flux through cylindrical parallel pores perpendicular or oblique to the membrane surface; ϵ : surface porosity; r : pore radius; η : viscosity; τ : pore tortuosity; $\frac{\Delta P}{\Delta x}$: pressure difference across a membrane of

thickness Δx [3], [6]: Volume flux through cylindrical parallel pores perpendicular or oblique to the membrane surface; ε : surface porosity; r : pore radius; η : viscosity; τ : pore tortuosity; $\frac{\Delta P}{\Delta x}$: pressure difference across a membrane of thickness Δx [3], [6], [9], [13]

Surface porosity ε_s is defined by the ratio of the pore area to membrane area, multiplied by the number of pores [3]:

$$\varepsilon_s = n_p \frac{\pi r^2}{A_m}$$

Equation 16: Surface porosity; n_p : number of pores; A_m : membrane area [3]

However, unfortunately this has to be differentiated from membrane porosity, also ε , which in several other literature [1], [2], [11] is defined as the ratio of the volume of pores to total membrane volume.

It is, however, very rare to find membranes that have a consistent pore structure, as in Figure 13a. Membranes with a pore structure consisting of closely packed spheres (Figure 13b) can usually be found in sintered membranes or phase inversion membranes consisting of a nodular skin layer. Volume flux of such membranes can be calculated using the Carman-Kozeny relationship [3], [11]:

$$J = \frac{\varepsilon^3}{K\eta S^2(1-\varepsilon)^2} \frac{\Delta P}{\Delta x}$$

Equation 17: Volume flux of membranes consisting of a pore structure with closely packed spheres can be best described by the Carman-Kozeny relationship; J : volume flux; S : internal surface area; K : Carman-Kozeny constant (dependant on pore shape and tortuosity); ε : pore volume fraction [3], [11], [13]

The mathematical modelling of screen filters (usually used in ultra- and microfiltration) has been extensively researched and is a relatively simple model. The molecular weight cut-off is an imperative characteristic of UF membranes and thus are relevant for UF applications. In filtration processes, the smallest particles (significantly smaller than the smallest pores) permeate through the membrane, whereas particles much larger than the largest pores are retained. Particles whose sizes lie between the smallest and largest pores are also retained, depending on the pore size distribution of the membrane. Therefore, it is beneficial for such membranes to have very narrow pore size distributions to ensure a sharp MWCO. However, even in membranes that have identical pore sizes, the observed MWCO is not a sharp cut-off, as the entire pore cross-section area is available for transport for particles much smaller in diameter than the pore diameter. Larger particles with similarly/slightly smaller diameters as the pore diameters only have a smaller portion of the pore cross-section area available to them, as seen in Figure 15 [1], [2].

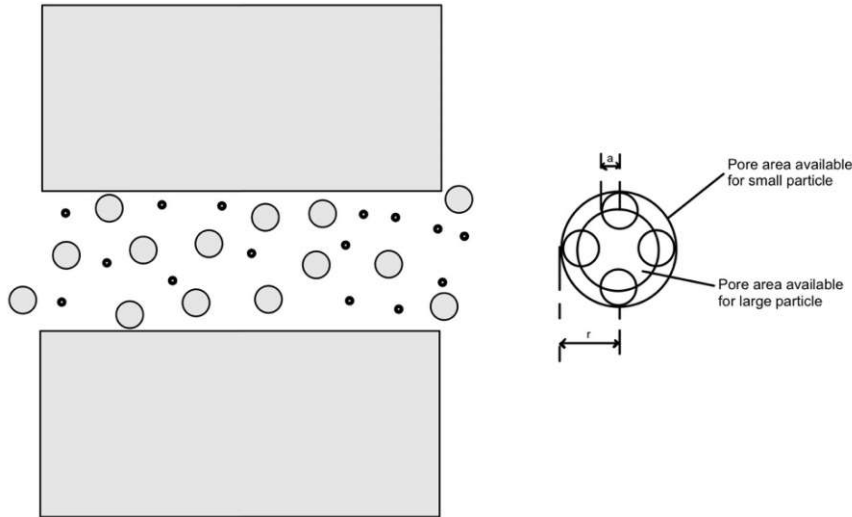


Figure 15: Transport of spherical particles of two different components through a circular pore; a: radius of a particle; r: pore radius; adapted from [2]

The pore cross-section area available for the small particle transport can be given as:

$$\varepsilon_p = \pi r^2$$

Equation 18: Pore cross-section area available to the transport of the small particle [2]

The pore cross-section area available for the large particle transport can be given as:

$$\varepsilon_a = \pi(r - a)^2$$

Equation 19: Pore cross-section area available to the transport of the large particle [2]

Thus, the concentration of the large particle in the feed and permeate can be calculated by utilizing the ratio of the membrane pore area available for a particle with radius a to the membrane pore area:

$$\frac{\varepsilon_a}{\varepsilon_p} = \frac{(r - a)^2}{r^2} = \frac{C_p}{C_f}$$

Equation 20: Relationship between the ratio of the area available for a particle with radius a to membrane pore area and the ratio of the concentrations in permeate and feed respectively [2]

Using the rejection of a membrane, we can obtain:

$$R = \left(1 - \frac{C_p}{C_f}\right) = 1 - \frac{(r - a)^2}{r^2}$$

Equation 21: Relationship between the rejection of a membrane and the ratio of the two areas in question as well as the ratio of the concentrations in feed and permeate [2]

Later, Renkin modified Equation 21 to take into account the parabolic flow velocity profile of the particle as it passes through the pore:

$$\frac{\varepsilon_a^*}{\varepsilon_p} = 2\left(1 - \frac{a}{r}\right)^2 - \left(1 - \frac{a}{r}\right)^4$$

Equation 22: Ferry-Renkin model with a parabolic flow velocity of the particle through a pore [2]

The Ferry-Renkin model can be further modified to consider the feed flow velocity profile of the particle in a uniformly shaped cylindrical pore:

$$R = \left[1 - 2\left(1 - \frac{a}{r}\right)^2 - \left(1 - \frac{a}{r}\right)^4 \right]$$

Equation 23: Ferry-Renkin model and rejection of a membrane [2]

Until this point, the top layer characteristic of UF membranes have not been taken into account. In literature [1]–[3], [6], [11], UF membranes can also be utilised for gas permeation if the pores diameters $\geq 0,1 \mu\text{m}$, gas molecule transport can be described by convective flow (Hagen-Poiseuille's law). The mean free path is the average distance the gas molecules travel before colliding with another molecule. The mean free path λ of the gas molecules decreases as the pore radius r decreases, and therefore the ratio of pore radius to mean free path falls under 1. This means that more collisions between gas molecules and the walls are likely to occur than between gas molecules themselves. When the ratio $\frac{r}{\lambda}$ is more significant than 1, Hagen-Poiseuille flow dominates within the pores. Knudsen flow usually predominates at lower pressures and pore radii of less than 500 Angstroms.

This phenomenon is called Knudsen diffusion. Knudsen diffusion can be neglected in liquids as the molecules are closer together than in a gas. The mean free path of liquid molecules is drastically smaller than the mean free path of gas molecules. The mean free path of gas molecules is dependent on pressure and temperature. λ increases as the operating pressure decreases, and the mean free path is directly proportional to the operating temperature at constant pressure.

$$\lambda = \frac{kT}{\pi p d_{gas}^2 \sqrt{2}}$$

Equation 24: Mean free path of gas molecules; d_{gas} : diameter of the gas molecule; p : pressure; T : temperature; k : Boltzmann constant [1]–[3]

In this regime, the volume flux can be written as:

$$J = \frac{nr^2 D_k \Delta p \pi}{RT \tau l} ; D_k = 0,66r \sqrt{\frac{8RT}{\pi M_w}}$$

Equation 25: Volume flux in Knudsen flow; J : volume flux; n : number of pores in a unit area of the membrane; r : pore radius; Δp : pressure difference; l : the thickness of the membrane; τ : tortuosity; D_k : Knudsen diffusion coefficient; M_w : molecular weight [2], [3]

However, before the molecules pass through the pores with the several models described above, the molecules need to transport through the selective surface layer. This step is the rate-determining step [2], [3].

Another method commonly utilized to describe mass transport is the friction model. This method examines the transport of the molecule through the pores of the membrane by Poiseuille flow and diffusion [3]. As shown in Figure 12, multiple models have been experimented with and utilized to describe mass transport and transport model in membranes of different pore sizes.

Other models have also been utilized in literature [2], [11] that describe the mass transport in UF membranes. UF processes have been described as controlled by the top layer (retained molecules deposit on the membrane surface), and such diffusive effects also need to be considered. Many diffusion models have been widely utilised- gel permeation and osmotic pressure models, among others. Figure 12 depicts multiple different models- surface diffusion and molecular sieving etc.

2.1.6 Classification Based on Production Process and Materials

2.1.6.1 Membrane Materials

Returning to membrane classification, one more classification method is the materials that are applied to produce membranes. Figure 3 illustrates the classification of membranes into synthetic and biological membranes. Another way to sort out the synthetic membrane category is by division into organic and inorganic membranes. Assessing a membrane based on its materials gives more insight into membrane separation, nature, and magnitude of the relationship between the feed, permeates, and membranes. Materials utilised for membrane production dictate the packing density and the polymer chains' segment mobility making up the membrane's solid parts. The choice of a particular material for a membrane and membrane separation process depends on the specific properties of the materials chosen. Two of the most important membrane properties- permeation and selectivity are determined by intrinsic chemical properties of the material (in this case, a polymer), such as the glass transition temperature, hydrophobic/hydrophilic nature of the material, pore size and pore size distribution of the membrane structure [2], [3], [20].

The most technically and commercially relevant membrane materials for membrane production are polymers. Other materials like metals, ceramics and glasses are typically only utilised for unique applications, e.g., pure hydrogen production, isotope separation at elevated temperature [2], [16], [20].

Polymers consist of long chains that are made up of smaller basic units called monomers. These monomers are essentially building blocks of the same or lower molecular weight. Their chemical structure, molecular weight, the number of these building blocks in a polymer chain, and the relationship between the building blocks in the polymer chain determine the chemical and mechanical stability of the polymer and the sorption of low molecular weight organic/inorganic compounds. The molecular weight of a polymer molecule is dependent on the degree of polymerisation, which is the number of monomers linked together to form the polymer molecule. Monomers are connected into long chains through covalent bonds [2], [3], [20].

Other important physical properties of a polymer are heavily influenced by the polymer chains' size and length. Melting and boiling points, impact resistance, and melt viscosity tend to rise as chain length increases. On the other hand, increasing chain length decreases chain mobility and increased strength, toughness, and higher glass transition temperatures due to increased chain interactions. Another essential characteristic is the architecture of polymer- whether it is linear or branched. Branched polymers typically include a main chain with many substituent branches. The architecture of a polymer is responsible for affecting many physical characteristics such as melt and solution viscosity, solubility in solvents, glass transition temperature and the size of each polymer coil in solution [2], [3], [9].

Some common polymers utilised for membrane production and process are listed in Table 5.

In this thesis, polyethersulfone was chosen due to its simple handling and convenient widespread use in the biomedical field. PES is widely used to produce micro- and ultrafiltration membranes through a phase inversion process [21]. Polyethersulfone is a pale yellow, glassy, amorphous thermoplastic polymer that is very temperature and chemical resistant. Its widespread use in membrane separation fields is validated by its excellent oxidative, thermal, hydrolytic, and mechanical stability. It is widely commercially available (thus easier to obtain and purchase) and exhibits exceptional biocompatibility, selectivity, and permeability characteristics. PES membranes find their application in several fields- especially the biomedical field- where such membranes are utilised as artificial organs and blood purification devices, e.g., haemodialysis, plasma collection etc. PES membranes display a hydrophobic property - thus having the disadvantage of being easily fouled [9], [21], [22].

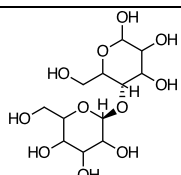
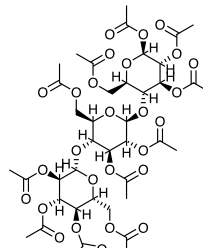
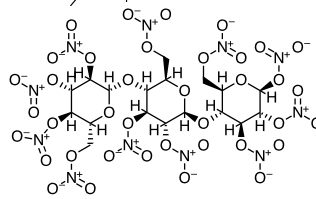
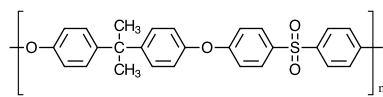
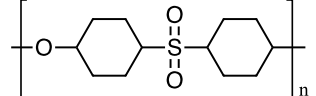
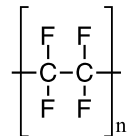
Membranes can be produced using inorganic compounds as well. These membranes usually find their application in high-temperature industrial chemical processes due to their high thermal and chemical stability [1]–[3], [11], [20].

2.1.6.2 Membrane Preparation

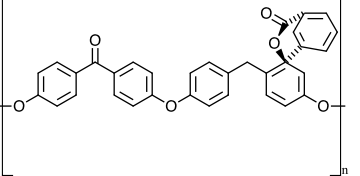
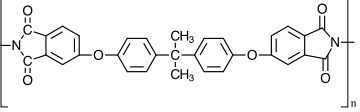
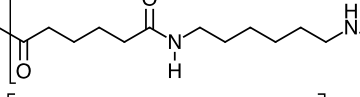
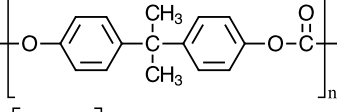

Depending on the function the membrane is supposed to fulfil, the structure and pore distribution, separation properties, different methods can be used to create a membrane suited to the task. Many technologies exist and are widely used- simple sintering of polymeric/ceramic powders, template leaching, interfacial polymerisation, stretching, track-etching, electrospinning, phase inversion and many more subcategories of each technology. Amongst these various technologies, the most common technology is phase inversion [2], [3], [13].

Separating a homogenous polymer describes phase inversion into two different and distinct phases, a polymer-rich that forms the basis of the solid membrane matrix and a polymer-lean phase that includes the membrane pores. It is generally a thermodynamically driven process. Phase inversion is incredibly versatile, as it can be used with any polymer that exists in a specific composition in a homogenous solution and that shows a decomposition in two phases due to an alteration in the free energy of mixing of the system, which in part is due to the change in temperature/composition. Therefore, a wide range of polymers are applicable and fit the description. Moreover, phase inversion can lead to a membrane with a wide range of pore size variations and a high level of filtration rate. Phase inversion processes have widely found their function in the production of polymer membranes for water purification, MF; UF, NF, reverse osmosis, gas separation and other chemical, pharmaceutical, medical and food applications [2], [3], [9], [15], [18], [19], [23].

Table 5: An overview of polymers utilized for membrane production [2], [3], [6], [9], [14]–[16], [19], [21], [24]

Polymer	Melting point [°C]	Young Modulus [GPa]	Membrane process	Structure
Regenerated cellulose			UF, MF, dialysis, membrane chromatography, virus filtration	
Cellulose acetate (CA), cellulose diacetate and cellulose triacetate (CTA)	210	1,4	UF, MF, gas separation, reverse osmosis, dialysis	
Cellulose nitrate (CN)	240	1,4	UF, MF	
CA/CN blends	210-240	1,4	UF	-
Polysulfone (PSf)	200	2,61	UF, MF, gas separation	
Polyethersulfone (PES)	360	2,5	UF, MF, membrane chromatography, virus filtration	
Polytetrafluoroethylene (PTFE)	325	0,5	UF, MF	

Polyvinylidene fluoride (PVDF)	171	1,5	UF, MF	
Polyethylene (PE)	135	0,7	UF, MF	
Polypropylene (PP)	175	1,3	UF, MF	
Polyvinylchloride (PVC)	160	3,4	UF, MF	
Polyacrylonitrile (PAN)	322	10	UF, MF, dialysis, membrane chromatography	
Polyimide (PI)	-	2-2,5	UF, MF, gas separation	
Polyetheretherketone (PEEK)	350	3,6	UF, MF	

Modified polyetheretherketone (PEEK-WC)	400	-	UF, MF	
Polyetherimide (PEI)	204-232	2,3-12,5	UF, MF	
Polyamide (PA)	215	2,7	UF, MF, NF, reverse osmosis, dialysis	
Polycarbonate (PC)	155	0,055-0,075	UF, MF, gas separation, dialysis	
Poly(lactic acid) (PLA)	175	4,8	UF, MF, gas separation	

Based on this definition, there are multiple different sub-technologies of phase inversion [2], [3], [9], [15], [18], [19]:

- i. Diffusion-induced phase inversion/separation (DIPS): demixing and precipitation occur by immersing the dope solution in a nonsolvent bath. This is also sometimes referred to as nonsolvent induced phase inversion/separation (NIPS), immersion precipitation or, more uncommonly as solvent-induced phase inversion/separation (SIPS). This technique is the one this thesis puts a particular focus on.
- ii. Temperature-induced phase inversion/separation (TIPS): also known as 'melt casting'; demixing of the two phases and precipitation occurs due to a temperature change. The process is based on the concept that the solvent acts as a suitable solvent at temperatures close to the polymer's melting point but acts as a nonsolvent at lower temperatures.
- iii. Evaporation induced phase inversion/separation (EIPS): demixing and precipitation occur due to the evaporation of a volatile solvent from the dope solution. This also refers to preparing a homogenous mixture of the polymer and two solvents, followed by precipitation into two phases. The polymer-rich phase is solid if one of the solvents present in the solution evaporates.
- iv. Vapour-induced phase inversion/separation (VIPS): also known as 'dry casting' or 'air casting'; nonsolvent that is present in the surroundings of the dope solution (water, nitrogen, oxygen etc.) is adsorbed from a vapour phase, affecting the porosity of the cast membrane.
- v. Pressure-induced phase inversion/separation (PIPS): also known as 'pressure casting'; a porous structure is induced by reducing the pressure/increasing the temperature to expand the saturated dissolved gas cells within the dope solution.
- vi. Reaction-induced phase inversion/separation (RIPS): demixing and precipitation occur by a reaction between monomers in the dope solution due to increased molecular weight or nonsolvent production.

Most of the phase inversion processes described above are thermodynamically driven, and the demixing and precipitation processes can be visually described using a ternary phase diagram [9]. A detailed approach is described in 2.2.1.

2.2 The NIPS-Process

2.2.1 Thermodynamic Principle

As described above, the NIPS process is one of the most widely used phase inversion processes to produce membranes. Usually, the resulting membrane from this technique is asymmetric in its structure and can be utilised in various applications. Using the NIPS process, membranes can be prepared to be either flat or tubular (hollow fibres) [3].

Before going in-depth to the ternary phase diagrams, it is necessary to comprehend the thermodynamics behind the phase inversion. Generally, all phase inversion processes begin with a thermodynamically stable homogenous solution that undergoes demixing for one cause or another. Therefore, all phase inversion processes stem from the same thermodynamic principles. Two different but

fundamental approaches describe the phase inversion process. A qualitative approach to describing polymer solubility is the solubility parameter theory. A quantitative approach to explaining the phase inversion process is given by the Flory-Huggins theory [3], [9], [23].

Firstly, the thermodynamic principles for mixing and demixing need to be established. The state of any closed system can always be described using the relationship between the Gibbs free enthalpy change (ΔG), enthalpy change (ΔH), the absolute temperature and the entropy change (ΔS) during the process [3], [9], [18]:

$$\Delta G = \Delta H - T\Delta S$$

Equation 26: Gibbs free enthalpy change for a closed process at constant temperature [3], [18]

For a pure substance, the thermodynamic properties are functions of temperature and pressure. However, things get a little more complicated when a mixture is considered. The composition, number of moles of the components, intermolecular forces, activity, the chemical potential of the polymer are imperative to determine the thermodynamic properties of the system. To describe the mixing or a chemical reaction of two or more components, the free change of enthalpy ΔG is changed to [3], [9], [18]:

$$\Delta G_m = \Delta H_m - T\Delta S_m$$

Equation 27: Gibbs free enthalpy change for a dissolving process, where the subscript m refers to mixing [3], [9], [18]

The Gibbs free enthalpy change for a mixing process can also be written as:

$$\Delta G_m = G - \sum_i n_i G_i^0$$

Equation 28: Gibbs free enthalpy change at constant temperature and pressure for a mixing process; n_i : number of moles of component i; G_i^0 : Gibbs molar function of the pure component [9]

The dissolving process occurs spontaneously if the Gibbs free enthalpy change for mixing ΔG_m is negative ($\Delta G_m < 0$). For mixtures where one of the components to be dissolved is a polymer, the free entropy change during the process is much smaller than the enthalpy change. Thus, the deciding factor for the spontaneous dissolution of the components relies heavily on the enthalpy change of mixing. Assuming that the system in mind is a binary system, and for small apolar solvents, the enthalpy of mixing can be described by the Hildebrand expression [3], [9], [18]:

$$\Delta H_m = V_m \left[\left(\frac{\Delta E_1}{V_1} \right)^{0,5} - \left(\frac{\Delta E_2}{V_2} \right)^{0,5} \right]^2 \phi_1 \phi_2$$

Equation 29: Hildebrand expression to describe the enthalpy change of mixing; V_m , V_1 , V_2 : molar volume of the solution, component 1 and 2; ΔE : energy of vaporisation; ϕ_1 , ϕ_2 : volume fractions of components 1 and 2 [2], [3], [9], [18]

The term $\frac{\Delta E}{V}$ can be referred to as the cohesive energy density (CED) and an important parameter, the solubility parameter δ can be written as:

$$\delta = \sqrt{CED} = \sqrt{\frac{\Delta E}{V}}$$

Equation 30: Solubility parameter δ [2], [3], [9], [18]

Cohesive energy density refers to the energy needed to remove a molar volume of molecules from the bulk. Equation 30 can be rewritten as:

$$\Delta H_m = V_m [(\delta_1) - (\delta_2)]^2 \phi_1 \phi_2$$

Equation 31: Hildebrand expression, rewritten [2], [3], [9], [18]

The value of enthalpy change of mixing approaches zero when the solubility parameters for components 1 and 2 are very similar. Since the entropy change of mixing can never be smaller than zero, thus it can be deduced that the Gibbs free enthalpy change is more than likely to be negative. Therefore, it can be concluded that a spontaneous dissolution is more probable to occur when the solubility parameters of the components are nearly the same as each other [3], [9], [18].

As the solubility parameters of the components in question start to differ broadly, this, in turn, implies that the affinity between the polymer and solvent also decreases. To create a more accurate depiction of such a phenomena, Hansen broke the solubility parameter into contributions of different intermolecular forces [3], [18]:

$$\delta^2 = \delta_d^2 + \delta_p^2 + \delta_h^2$$

Equation 32: Solubility parameter; subscripts d, p and h refer to dispersion forces, dipole-dipole forces and hydrogen bonding [3], [18]

The difference in solubility parameters between polymer and solvent can be expressed as:

$$\Delta = [(\delta_{d,p} - \delta_{d,s})^2 + (\delta_{p,p} - \delta_{p,s})^2 + (\delta_{h,p} - \delta_{h,s})^2]$$

Equation 33: The three-dimensional solubility parameters can be considered as three vectors along orthogonal axes where the solubility parameter is the end-point of the vector [3], [18]

With reducing values of Δ (as it approaches null), the affinity between the polymer and solvent increases [3].

Having described the solubility parameter model, it is vital to consider the limitations of this model. The solubility parameter described by Hansen and Hildebrand only considers certain intermolecular forces (van der Waal's bonding) and thus is negligent of other intermolecular forces. This is why the splitting of the solubility parameter by Hansen and Hildebrand [3], [18].

A second but more critical and more commonly-used model is the Flory-Huggins model [23]. The Flory-Huggins model takes the sizeable molecular size difference between the polymer and solvent into consideration. Based on this assumption, ΔG_m , ΔS_m and ΔH_m for binary and ternary systems can be expressed [3], [9], [18], [23].

Considering that the surface of the mixture consists of homogenous molecules and that the total number of moles N in the system is known, the probability of a small molecule encountering the solvent molecule depends on the molar fraction of the solvent. However, when a polymer is utilised, the likelihood that a macromolecule

occupies the same space is higher as the concentration and molar mass of the polymer increase. This is shown in Figure 16. Thus, the enthalpy of mixing can be expressed as a function of the volume fraction [9]:

$$\Delta H_m = n_1 \phi_2 N_{av} z \Delta \epsilon_{12} = RT n_1 \phi_2 \chi_{12}$$

Equation 34: Enthalpy of mixing as a function of volume fraction; n : number of moles; N_{av} : Avogadro's number; χ_{12} : Flory-Huggins interaction parameter [3], [9]

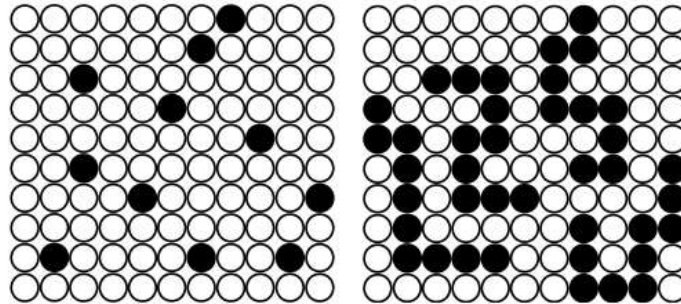


Figure 16: Flory-Huggins lattice model: molecular distribution in a binary system of (a) monomers and (b) polymers in a solvent [9]

For ideal solutions, $\Delta H_m = 0$, and ΔG_m is only determined by ΔS_m . In a binary solution, each solute molecule is surrounded by z number of particles. The ability of the solute molecule to move in the system is related to the parameters responsible for the definition of the entropic degree of disorder- translation, rotation and vibration. In an ideal system, the entropy of mixing arises due to the molecular disposition of the molecules in space, and therefore the only entropic contribution to be taken into account is the entropy of configuration S [9]:

$$S = K \ln W$$

$$S = -R(n_A \ln x_A + n_B \ln x_B)$$

Equation 35: Entropy of configuration S as a function of the Boltzmann constant K and W , dependent on how the solute molecules (A ; N_A) arrange concerning the solvent B , is the number of all possible solutions microscopic states. This entropy can be rewritten by expressing the number of molecules as a function of the molar fraction of the particles and the number of moles of the components [3], [9]

Assuming, as it is in our case, that the solute is a polymer/macromolecule, the degree of motion of the molecules is severely lessened due to the dimension and concentration of the macromolecules in the solution. Therefore, by assuming that the polymer is linear and composed of σ segments, the entropy can be alternatively illustrated in terms of the volume fraction. The total number of molecules in a binary system with monomers would be $n_t = n_1 + n_2$. However, since a macromolecule is a solute here, the lattice site is not occupied by a complete molecule but by a segment. Therefore, the total number of molecules changes to what is used in Equation 36 [3], [9]. These can be expressed as:

$$\phi_1 = \frac{n_1}{n_1 + \sigma n_2} = \frac{n_1}{n_t}; n_1 = \left(\frac{\phi_1}{\sigma_1}\right)n_t$$

$$\phi_2 = \frac{n_2}{n_1 + \sigma n_2} = \frac{n_2}{n_t}; n_2 = \left(\frac{\phi_2}{\sigma_2}\right)n_t$$

Equation 36: Volume fraction for a polymer/solvent system in terms of the number of molecules for 1 (solvent) and 2 (polymer) and the total number of molecules n_t [3], [9]

Thus, the entropy of mixing can be alternatively written as:

$$\Delta S_m = -R(n_1 \ln(\phi_1) + n_2 \ln(\phi_2))$$

Equation 37: Entropy of mixing in a polymer/solvent mixture [3], [9]

The Gibbs free energy of mixing for a polymer/solvent system can thus be expressed as:

$$\Delta G_m = RT(n_1 \ln(\phi_1) + n_2 \ln(\phi_2) + n_1 \phi_2 \chi_{12})$$

Equation 38: Gibbs free energy of mixing for a polymer/solvent system under the Flory-Huggins model [3], [9], [18], [23]

Next, since the NIPS process in this thesis is based on a ternary system (PES, NMP and water), a ternary system is observed. There are multiple factors to keep in mind here: the stability and demixing behaviour of the solution now also depends on this third element (in this thesis's case: water as nonsolvent). The Flory-Huggins model describes the Gibbs free energy of mixing for a ternary system [3], [9], [18], [23]:

$$\Delta G_m = RT(n_1 \ln(\phi_1) + n_2 \ln(\phi_2) + n_3 \ln(\phi_3) + n_1 \phi_2 \chi_{12} + n_3 \phi_1 \chi_{13} + n_3 \phi_2 \chi_{23})$$

Equation 39: Gibbs free energy of mixing for a ternary system [3], [9], [18], [23]

Before moving on, a short description of the Flory-Huggins interaction parameter is maybe necessary. This parameter is defined as the measure of interaction between and two components in the solution. When the parameter is positive, the two components show a repulsive behaviour to one another. The relationship between the interaction parameter and the Gibbs free energy of mixing can be observed and graphed in [3], [18]. This can be seen in Figure 17(a). At low χ , a concave ΔG_m is expected whereas, with higher χ , the curve begins to show a convex

behaviour in the middle of the curve, and this is precisely the part where mixing becomes more and more unfavourable [9], [18].

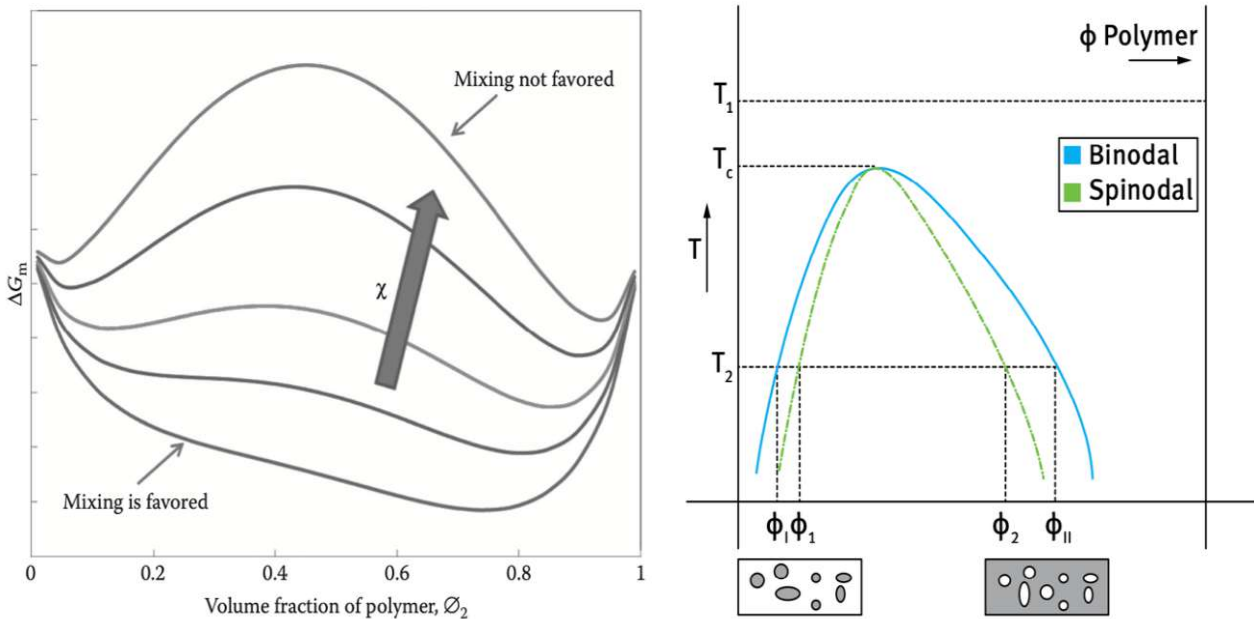


Figure 17: (a) Dependence of ΔG_m on χ (left) (b) Binodal and spinodal curves illustrated for a polymeric solution as a function of the volume fraction (right) [9], [18]

2.2.2 Demixing Processes

Demixing of a thermodynamically stable homogenous solution occurs when there are specific changes to the system's energy or temperature. The Gibbs free energy of the system decreases as phase separation occurs to provide stability to the system. The free energy after demixing ΔG_{sep} is smaller than the free energy of the homogenous system ΔG_0 . Starting with a binary mixture and utilising the inflexion points and the minima for a polymeric solution, the binodal and spinodal curves can be graphed as a function of the volume fraction and a temperature/composition graph be obtained, as Figure 17(b) depicts. The type of demixing and the structure of the resulting membrane is determined by the binodal curve [23], whereas the spinodal curve represents the boundary between the stable and metastable regions [1].

All compositions that are at a temperature lower than the critical temperature T_C are thermodynamically stable. T_C is the critical temperature where the binodal and the spinodal curves meet. Above this temperature, one will always obtain a homogenous solution and a negative Gibbs free energy of mixing. Once the temperature is decreased to T_2 , demixing of the solution occurs when the binodal curve is reached, thus resulting in liquid-liquid demixing [3], [9], [18].

Assuming that the temperature decreases from T_1 to T_2 and the polymer concentration increases, the binodal curve (ϕ_I) is reached. Between ϕ_I and ϕ_1 , nucleation occurs where the solution contains tiny drops of polymer dispersed through the solution. The system in this region is stable and at equilibrium due to an absence of destabilising driving forces. The opposite effect is observed in the region ϕ_{II} - ϕ_2 , where instead of the polymer being dispersed through the solvent, the solvent is dispersed through the polymeric phase. Both these regions are metastable and highly crucial for membrane preparation through phase inversion. If a polymer/solvent

solution is utilised, whose composition lies within the two phases mentioned above and if the droplets agglomerate before the polymer solidifies after precipitation, this leads to an open porous system. However, if the composition of the solution is in the spinodal curve range (ϕ_1 - ϕ_2), then demixing occurs as the dispersed drops grow to form two different phases- a polymer-rich and a solvent-rich phase and the Gibbs free energy of the system is decreased to bring stability to the system [3], [9], [18].

Figure 18(a) depicts the convex curve of ΔG_m , characterised by a low χ value. The Gibbs free energy increases if a homogenous solution with a composition ϕ_0 is separated into two phases with compositions ϕ_I and ϕ_{II} . This case shows that the solution is stable, and no phase separation will occur as mixing is favourable. If the Flory-Huggins interaction parameter is high and dependent on the solution composition, a solution could be either stable, unstable, or metastable. In Figure 18(b), an unstable state is illustrated. If the solution's composition is at the concave-down part of the curve, even a small alteration will lead to a decrease in the Gibbs free energy. This region (ϕ_1 - ϕ_2) can be characterised by [3], [9], [18]:

$$\frac{\partial^2 \Delta G_m}{\partial \phi^2} < 0$$

Equation 40: Concave-part interval in the ΔG_m [3], [9], [18]

Once demixed, the solution will spontaneously separate into two phases until each one of these phases reaches ϕ_I' and ϕ_{II}' . At these volume fractions, the solution is at its most stable [3], [9], [18].

The third major case is the metastable state, which is shown in Figure 18(c). if the solution's composition finds itself outside of the concave-down interval but within the communal tangent line, any minor change from ϕ_0 to ϕ_I and ϕ_{II} results in a rise in the Gibbs free energy. This means that the demixing is not instantaneous. However, a minimisation of the Gibbs free energy can be achieved by phase separation into two phases with compositions ϕ_I' and ϕ_{II}' . Demixing of a homogenous solution that is in a metastable state can only be separated if a composition change is significantly and sufficiently large [3], [9], [18].

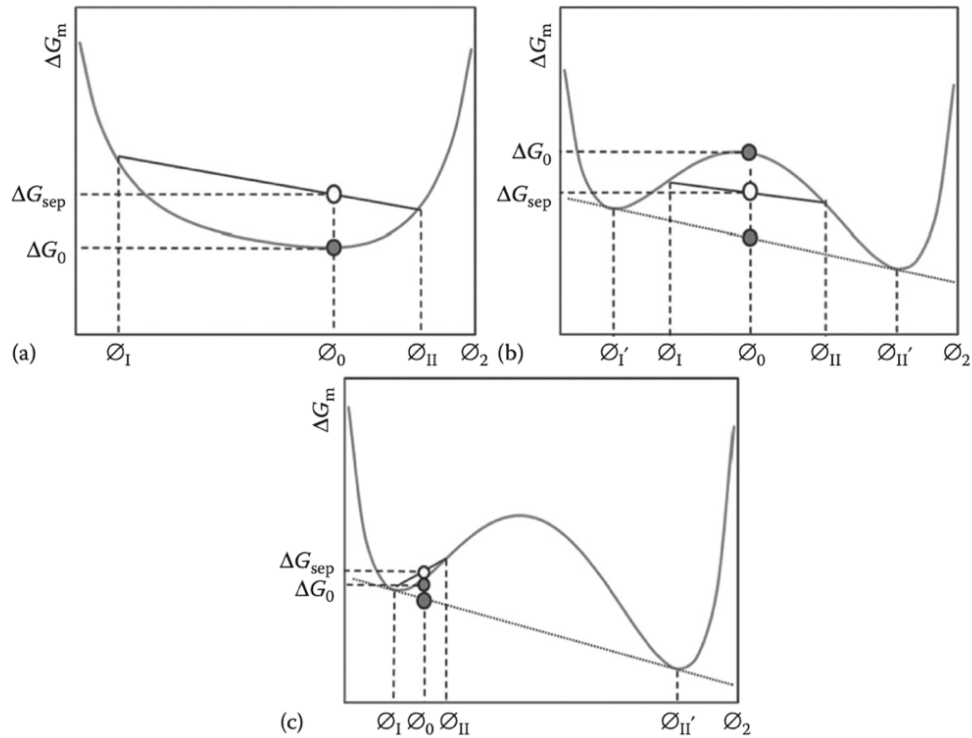


Figure 18: (a) Stable (b) unstable (c) metastable states of polymer/solvent mixture [18]

Additionally, the phases in a separated system have the same chemical potential if the system is in equilibrium. The chemical potential difference of a component i after mixing can be expressed as [3], [9], [18]:

$$\Delta\mu_i = \frac{\partial\Delta G_m}{\partial n_i}$$

Equation 41: Chemical potential difference of component i after mixing [3], [9], [18]

The chemical potentials of all the components in the solution can be obtained by the tangent line, as shown in Figure 19(a). The chemical potential difference at phase equilibrium in a separated binary system can determine the binodal. This is expressed as [3], [9], [18]:

$$\Delta\mu_i^I = \Delta\mu_i^{II}$$

Equation 42: Chemical potential difference of component i after mixing; superscripts I and II represent the two phases in a system [3], [9], [18]

Figure 19(b) depicts the curve's stable, metastable, and unstable regions, with the binodal and spinodal lines separating the particular areas. The binodal line is the boundary between the stable and metastable states, whereas the spinodal line depicts the border between the unstable and stable/metastable states. The binodal compositions can be found using the two points connected to the communal tangent line, whereas the spinodal boundary is defined by [3], [9], [18]:

$$\frac{\partial^2 \Delta G_m}{\partial \phi^2} = 0$$

Equation 43: Spinodal boundary [3], [9], [18]

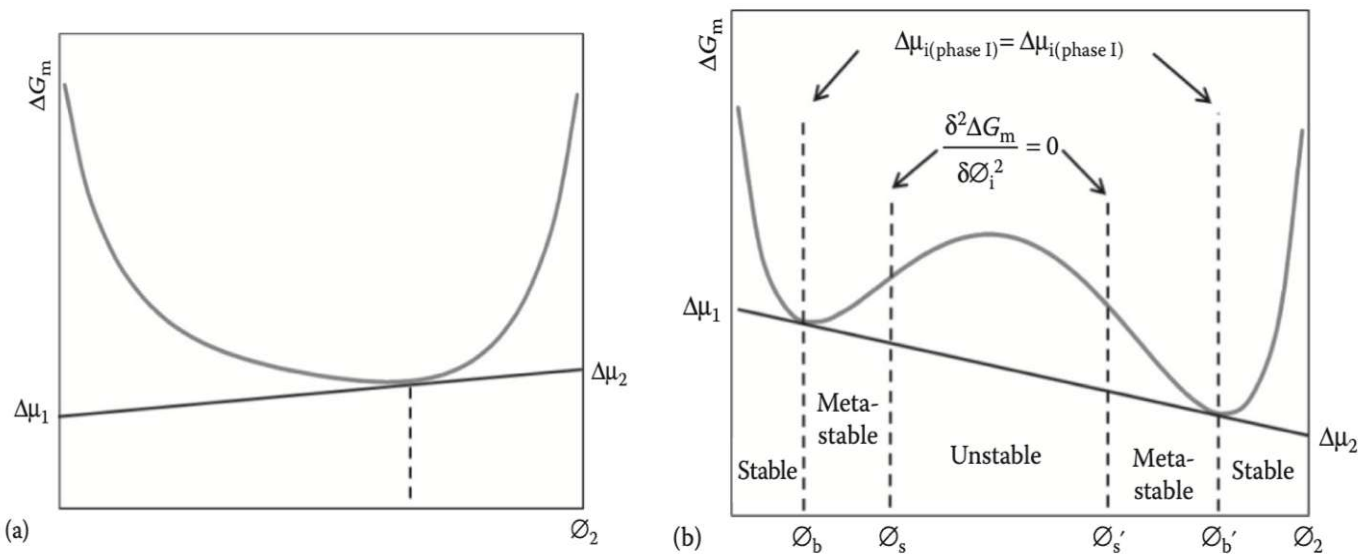


Figure 19: (a) Chemical potential (b) stable/metastable/unstable regions in ΔG_m graph [18]

This becomes much more complicated as a ternary system is considered. The system is dependent on three parameters, and the temperature/composition graph becomes a 3D graph. The same concept applies here: the critical point is again determined by the binodal and the spinodal meeting. At all temperatures higher than the critical temperature (at the crucial moment), all compositions of the three elements are possible and create a thermodynamically stable mixture. Travel lower than the critical temperature, demixing occurs, leading to phase separation. Travelling transversely along the diagram, the binodal and the spinodal can be represented in a 2D form. In this way, the thermodynamic behaviour of the solution can be further examined at a given constant temperature. This is called an isothermal system, and this concept, along with the ternary temperature/composition graph, can be applied to form the ternary phase diagram [3], [9], [18].

2.2.3 The Ternary Phase Diagram

Now that the most critical thermodynamic principles and concepts have been thoroughly discussed, the idea of the ternary phase diagram can finally be examined. The NIPS process can be depicted using the ternary phase diagram to show the course the phase separation takes, resulting in membranes with different properties. The ternary diagram is a triangle with each corner representing the three components to be mixed. On the corners, the three components are at their maximum concentration (100%). Any point on any side of the triangle represents a particular composition and a determined ratio between the two components on the corners of the same side. Any point within the triangle depicts a special specific composition of all three components [2], [3], [9], [13], [18].

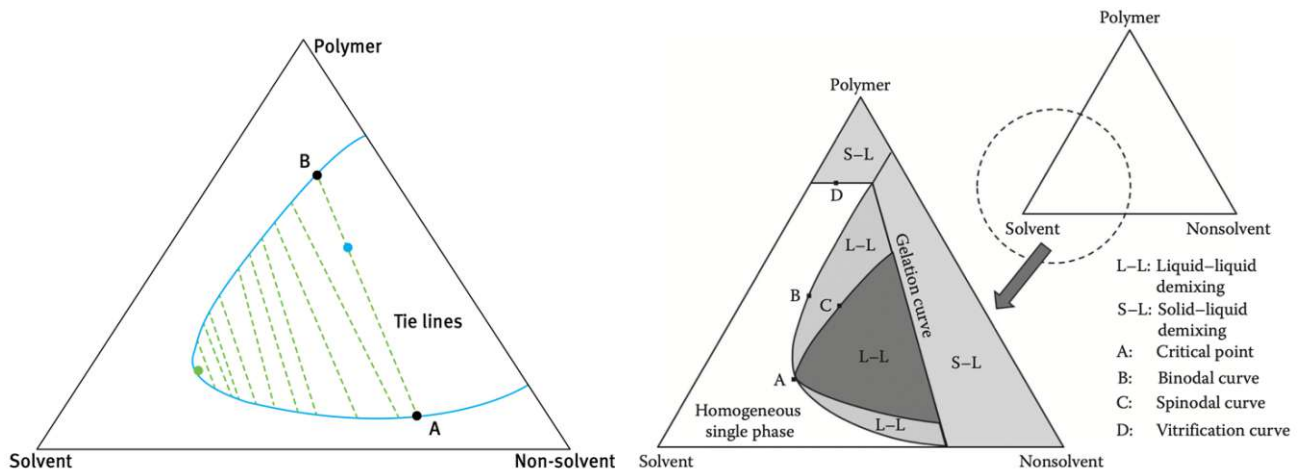


Figure 20: Left: tie lines for an isothermal graph: A and B lie on the binodal for a specific composition of the solution in consideration (blue point); right: ternary phase diagram for a NIPS process [9], [18]

The binodal and spinodal curves are plotted in a ternary phase diagram, the metastable and unstable regions, and the gelation, crystallisation, and vitrification curves, as shown in Figure 20.

The spinodal and binodal curves bound the metastable regions. This is where analogous to the binary system, the solution consists of specific volume fractions where nucleation occurs- either the solvent and nonsolvent are found to be in droplets in a polymer-rich phase or vice versa. When these droplets start to grow and agglomerate, then after solidification of the continuous phase, a porous membrane is the result. Under the spinodal curve, demixing occurs. When a point is chosen (as in Figure 20) under the binodal curve, two points (A and B) can be located on the binodal curve itself. These points refer to the phase composition at equilibrium and create a tie line if joined together. A set of tie lines can be illustrated for each ternary phase diagram, and a plait point can be observed at the top of the binodal, where the composition of the two phases is the same [3], [9].

The tie lines come in handy when the composition of the polymer-rich and -poor phases need to be determined. The two phases of the solution are always in thermodynamical equilibrium, and thus the composition of both phases can be calculated with this method. As shown in Figure 21, a tie line is defined by its point a and b. That means that the polymer-rich and -poor phase have a composition given by points b and a, respectively when the solution is at a state β . The volume fraction of each of these phases can be calculated from the phase diagram using the lever rule [2], [18]:

$$X_{polymer-rich} = \frac{\text{length of } a\beta}{\text{length of } ab}$$

Equation 44: Utilizing the lever rule to calculate the volume fraction of the polymer-rich phase; $X_{polymer-rich}$: volume fraction of the polymer-rich phase [17]

The ternary phase diagram consists of two regions as well [2], [9], [13], [18]:

- i. Single-phase region where all three components are miscible

- ii. A miscibility gap where a two-phase region is formed- a polymer-rich phase (the membrane itself) and a polymer-poor phase (the liquid within the pores of the membrane)

Additionally, the three curves (gelation, crystallisation, and vitrification curves) can also be observed. These curves symbolise the border where a polymer solution solidifies through various mechanisms [3], [18]:

- i. Crystallisation: The process of immobilisation of the polymer chains due to creating an ordered crystalline phase.
- ii. Vitrification: The process of immobilisation of the polymer chains when the glass transition temperature is passed.
- iii. Gelation: reduction of the polymer chains' mobility due to the creation of a 3D network by physical cross-linking.

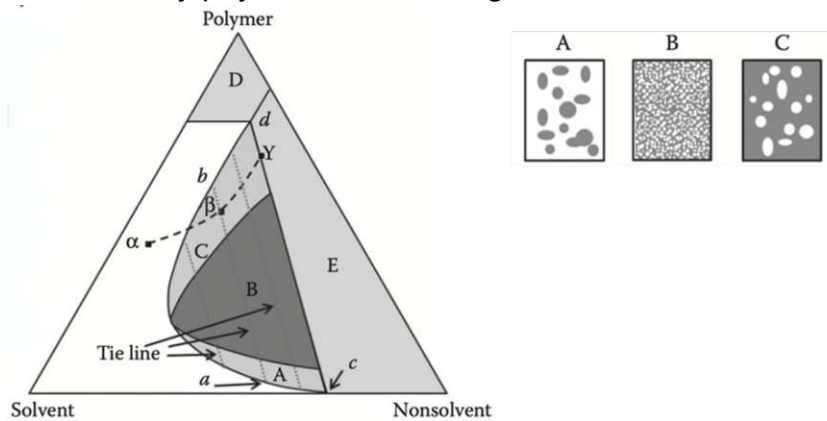


Figure 21: Membrane formation through the NIPS process [17]

Membrane formation is heavily dependent on the path the NIPS process takes in the ternary phase diagram. In the initial stages, the solution in question is found in the single-phase thermodynamically stable miscible homogenous region, in Figure 21 defined as the path starts α . As the solution is immersed in a nonsolvent coagulation bath (the most utilised component here being water), the solvent-nonsolvent exchange is initiated, as the solvent within the solution diffuses out into the bath. In contrast, the nonsolvent diffuses into the other direction into the solution. The path illustrates this diffusion α - β And the solution is now brought into either a metastable (A or C) or unstable region (B) due to the change in composition. Liquid-liquid demixing is bound to happen in this region, and the solution separates into two phases- a polymer-rich and a polymer-poor phase [2], [3], [18].

The mechanisms by which L-L (liquid-liquid) demixing occur differs from when the path travels in the metastable or unstable regions. When the solution enters the region C through the path α - β , L-L demixing occurs due to polymer-poor nuclei's growth within the continuous polymer-rich phase. This path results in a nascent membrane with a continuous polymer matrix and dispersed pores. The opposite occurs when the path leads to region A instead. There the polymer-rich nuclei grow within a continuous polymer-poor phase. The membrane formed through this path is not very practically viable, as they consist of a low-integrity structure with powdery agglomerates. This mechanism is called nucleation and growth [2], [3], [18].

However, if the path the solution takes travels through region B, no nuclei are formed, and therefore L-L demixing occurs using a different mechanism. Solutions from such a region separate into an interpenetrating network of polymer-rich and -poor

phases. This phase separation mechanism is called spinodal decomposition, and the membrane formed through this path shows an interconnected polymer matrix and pores [2], [3], [18].

Lastly, if the further exchange between the solvent and non-solvent is allowed to occur, the solution will travel from β to γ . At this state, the polymer-rich phase is solidified, and the structure of the membrane is 'frozen and fixed at this stage [2], [3], [18].

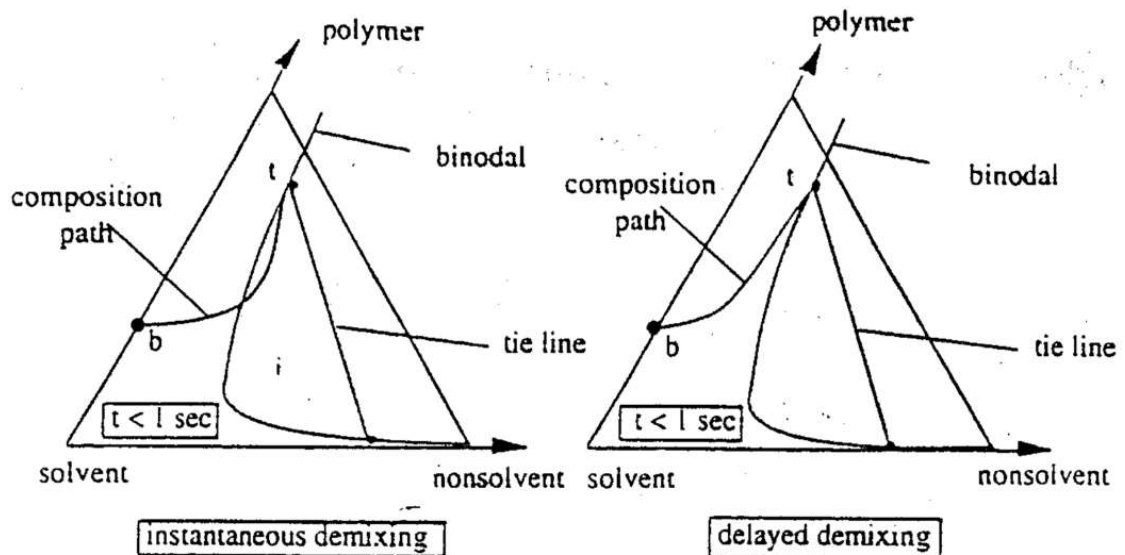


Figure 22: Schematic representation of the solution composition path immediately after immersion; t: top of the film; b: bottom of the film. Left: instantaneous demixing; right: delayed demixing [3]

Additionally, the morphology of the resultant membranes depends highly on the time it takes between immersion and L-L demixing. Two types of demixing have been described (Figure 22) [2], [3], [18]:

- i. Instantaneous demixing: phase separation takes place almost immediately after immersion of the solution into the coagulation bath, resulting in membranes with top dense skin layer and macrovoid-rich substructure. Such demixing is more likely to happen when the initial composition of the homogenous solution lies close to the metastable/unstable state, as only a tiny amount of nonsolvent is needed to induce phase separation. Kinetically speaking, the solvent-nonsolvent exchange occurs almost instantaneously.
- ii. Delayed demixing: this is the opposite of instantaneous demixing; membranes due to this type of demixing show spongy structures with a loose top layer. Observing the process through the kinetics of the process, if the rate of the solvent-nonsolvent exchange is slow, delayed demixing can occur, even though the initial solution lies close to its metastable/unstable state.

Before moving on to the practical aspects of the NIPS process, a few limitations need to be stated. While this thermodynamic equilibrium shown in the ternary phase diagrams can help predict the temperature and composition conditions under which a solution will separate into the two phases and the ratio of the two phases (overall porosity). However, this model cannot give any insight into the structural variations within the membrane cross-section and the skin layer. As stated previously, these

parameters are dependent on the kinetics of the process, the diffusivities of the components in the solution, the viscosity, and the chemical potential gradients of the components that act as driving forces for the diffusion of the components in and out of the solution. Due to the constant change of these parameters throughout the phase separation process, a quantitative description of membrane formation is close to impossible [2].

2.2.4 Spinning Process of Hollow Fibre Membranes

Moving on to the practical aspects of L-L demixing and phase separation, the reality, while based on the thermodynamic and kinetic principles described above, looks very different. As mentioned above, there are multiple methods to produce membranes, and each of these methods relies on a thermodynamic principle and ternary phase diagram that differs from each other. This thesis examines and applies the NIPS process and the spinning process to create hollow fibre membranes.

As stated in the units above, in a traditional NIPS process, the dope solution (usually a composition of polymer/solvent, can, however, include other additives and nonsolvent) is led through a small orifice (cast into a hollow fibre shape) before it is immersed into either first air (airgap; dry-jet spinning) and then the coagulation bath or directly in the coagulation bath (usually a nonsolvent like water; wet spinning). A liquid is also released through a smaller orifice in the centre that acts as an internal coagulant (usually a nonsolvent like water, called a borefluid) to create the hollow fibre shape. In the coagulation bath, precipitation occurs as the polymer-rich precipitates and starts to solidify, and the polymer-poor phase is responsible for pore formation. This is also where diffusion of the solvent and nonsolvent occur in opposite directions. Phase separation occurs faster in the surface as compared to the inner part, and this phenomenon is responsible for the asymmetrical structure of the membrane [1]–[3], [18], [19].

The orifices mentioned above is part of an integral part of the spinning unit- the spinneret. A gear pump pumps the dope solution through the outer nozzle and the bore fluid is pumped through the inner nozzle [2].

At this point, the precipitated fibre is rolled onto deflection rollers in the coagulation bath, rinsed and then taken up onto a drum/winder, ready for further processing, post-treatments, coating etc., as shown in Figure 23. The fibres are then stored and soaked for several days in water to extract and finish any remaining solvent exchange [1]–[3], [18], [19].

2.2.5 Influence of Spinning Parameters on the Hollow Fibre Membranes

As is abundantly clear from the sections above, multiple parameters influence and affect the final fibre structure, morphology, pore distribution, and finally, the permeability and selectivity of the hollow fibres.

As shown in Figure 24, it is quite a task to keep in mind all the parameters of the spinning process to produce hollow fibres that show promising results. It is evident that the theme of spinning hollow fibres is vast and is still in research and development. While these parameters influence the spinning process and the hollow fibres, much more pre-and post-treatments, coatings etc., can be performed for the preparation of unique hollow fibre membranes.

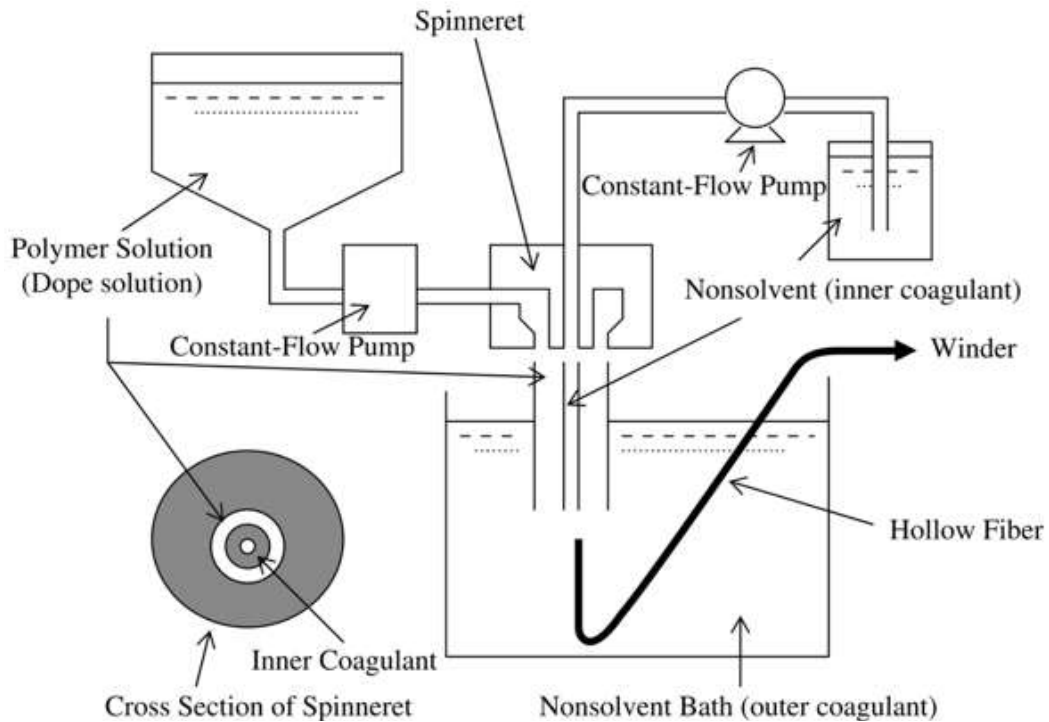


Figure 23: An example of a spinning unit to spin hollow fibres [19]

In the subsequent few units, a brief description from literature and research will be utilised to describe and examine each of the parameters that influence the spinning of hollow fibres. This thesis, however, only deals with a few parameters and explores their influence on the hollow fibre morphology, permeance and selectivity.

Conclusively, the aim is to create integrally skinned membranes. these can be characterised by:

- i. Thin and defect-free top layer
- ii. Open and mechanically stable sublayer with negligible resistance

2.2.5.1 Polymer

As mentioned above, a homogenous and stable dope solution is the starting point for the process. For phase inversion hollow fibre membranes, this solution typically consists of an appropriate polymer and a solvent for that polymer. Additives, nonsolvent etc., are added to improve the characteristics of the solution to produce membrane fibres fitting to the task at hand. Polymers utilised in UF processes should be resistant to chemical, mechanical, and thermal stresses and need to have the ability to dissolve quickly in a multitude of solvents. The choice of polymer utilised also plays a role in the fouling behaviour of the membranes, which, however, is not discussed in this thesis [2], [3], [18].

Polymer concentration is a heavy factor in the hollow fibre membranes produced using the NIPS process. A lower porosity and lower flux of the hollow fibre membranes may be observed when the polymer concentration in the dope solution is relatively high. This leads to a much higher polymer concentration at the interface and subsequently a higher polymer volume fraction [3], [18].

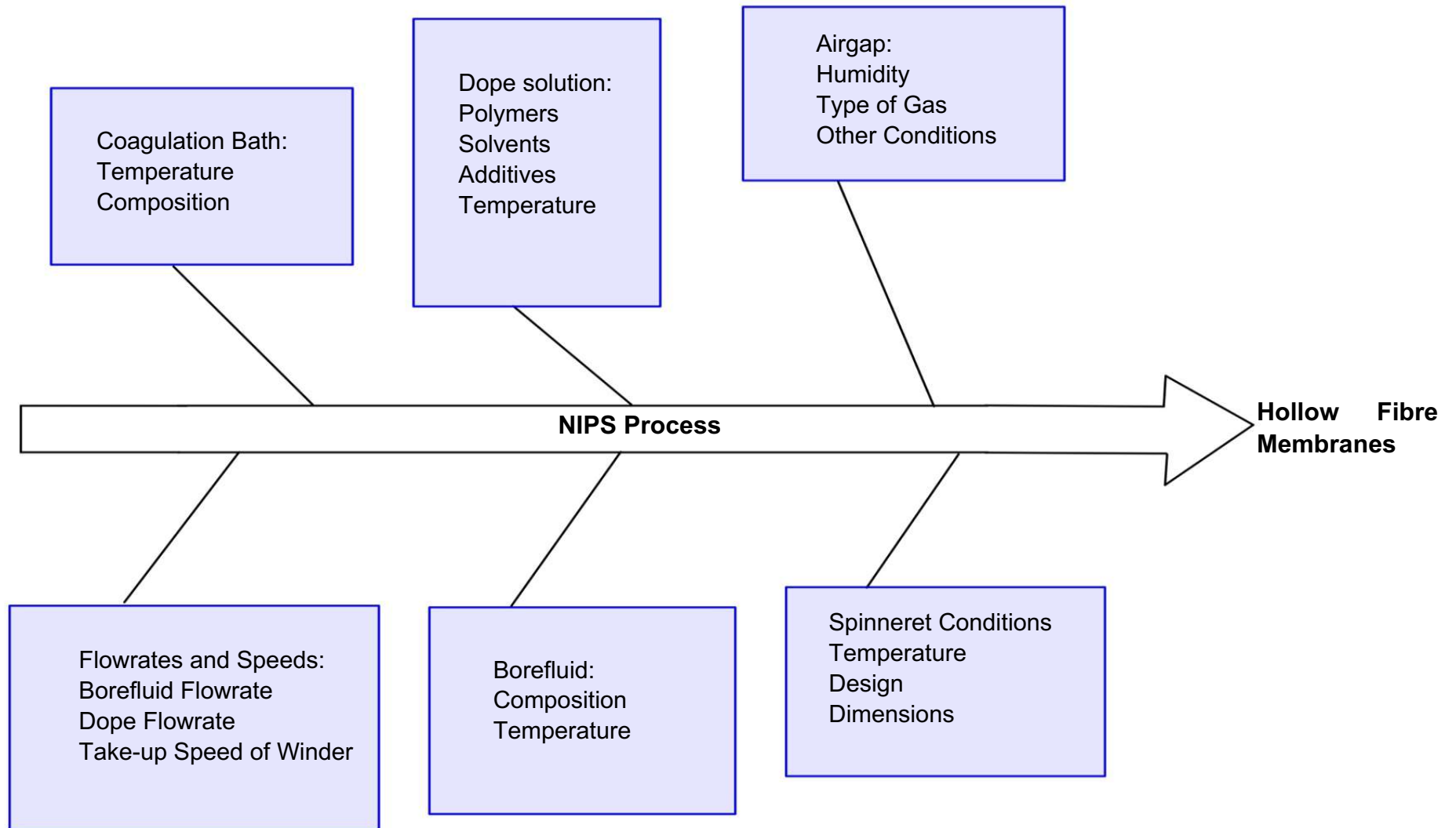


Figure 24: Influence of parameters on the spinning of hollow fibres membranes

A higher polymer concentration also means that a lower solvent volume fraction is used, and thus, less nonsolvent is necessary to achieve phase inversion. Polymer concentration, which plays a prominent role in the dope viscosity, also affects the kinetics of membrane formation and the solvent-nonsolvent exchange. Higher polymer concentration results in thicker skin, which can significantly delay the time it takes for the inner structure to coagulate. With higher polymer concentrations in the dope solution, the phase inversion process's thermodynamics are heavily influenced, as can be seen when the binodal curve in the ternary phase diagram for PEEK-WC hollow fibres shifts towards the polymer-solvent axis. This is a clear indication of a decreased nonsolvent tolerance [18].

Another interesting relationship with polymer concentration is its effect on the dope viscoelastic properties, as observed with PVDF hollow fibres. These properties influenced fibre morphology and macrovoid formation due to increased shear and elongation viscosities, as observed in a greater chain entanglement degree. This higher degree of chain entanglement led to reduced nonsolvent penetration during coagulation [18].

As mentioned above, the dope viscosity increases significantly as polymer concentration in the dope solution increases. A higher chain entanglement with a more significant presence of macromolecules is responsible for this phenomenon. An increase of polymer concentration in the dope solution also acts as a suppressant for macrovoid formation. It causes the long, open channel-like macrovoids to turn into finger- and tear-like structures intermitted by sponge-like areas [3], [18], [25].

2.2.5.2 Solvent

Analogously, a solvent must show a particular affinity to the polymer to obtain a homogenous solution. The Hansen solubility parameter can assess this choice, which has been discussed in the previous unit.

The choice of solvent heavily influences the membrane structure, as can be seen from the study performed by Bottino et al. [26], which studied the effect of eight different typically used solvents- N,N-dimethylacetamide (DMAc), N,N-dimethylformamide (DMF), dimethylsulfoxide (DMSO), N-methyl-2-pyrrolidone (NMP), hexamethylphosphoramide (HMPA), tetramethylurea (TMU), triethyl phosphate (TEP) and trimethyl phosphate (TMP)- on the morphological structure of PVDF flat membranes. It was observed that different solvents shifted the binodal curve in the ternary phase diagram and therefore played a deciding role in the path that was taken for L-L demixing to occur. Strong solvents for PVDF (e.g., DMSO) shift the binodal curve towards the solvent corner, whereas weak solvents for PVDF (e.g., HMPA) shift the binodal curve away from the solvent corner. Thus, it is to be concluded that less (with strong solvents) or more (with weaker solvents) nonsolvent is needed to initiate phase separation. The solvent-nonsolvent diffusivity is a deciding factor for the overall porosity of the membranes.

Macrovoid formation is also closely linked to the solvent-nonsolvent system. It has been observed that a solvent-nonsolvent system that shows good miscibility with each other results in membrane structures abundant in the channel- and finger-like pores, whereas a system with bad miscibility leads to spongy membrane structures. Barzin and Sadatnia [25] analysed PES flat membranes' morphology and macrovoid formation with a water/NMP and a water/DMAc system. They discovered that despite

the excellent miscibility between DMAc and water, this system produced membranes with spongy structures. They found that this was because the vitrification boundary intersects the binodal curve in lower polymer concentration compared to the NMP/water system. This leads to earlier vitrification of the polymer-rich phase of the water/DMAc/PES system compared to the water/NMP/PES system. Similar behaviour was observed with PVDF hollow fibre membranes as well [27].

Table 6: Classification of solvent-nonsolvent pairs [3]

Solvent	Nonsolvent	Membrane Type
DMSO	Water	Porous
DMF	Water	Porous
DMAc	Water	Porous
NMP	Water	Porous
DMAc	n-propanol	Nonporous
DMAc	i-propanol	Nonporous
DMAc	n-butanol	Nonporous
trichloroethylene	Methanol/ethanol/propanol	Nonporous
chloroform	Methanol/ethanol/propanol	Nonporous
dichloromethane	Methanol/ethanol/propanol	Nonporous

The influence of the solvent-nonsolvent system is observed on the type of demixing that occurs in the NIPS process (instant/delayed demixing). A general trend is seen here- polymers used in a system of THF or acetone with water produce dense membranes due to delayed demixing. When DMSO and DMF are used in a system along with water, porous membranes are the result, ideal for UF processes, as shown in Figure 25. As shown in Table 6, a porous membrane is the result of a system where the solvent and nonsolvent have a high mutual affinity to each other. When the solvent and nonsolvent have a low mutual affinity to each other, a nonporous or an asymmetric membrane with a dense skin layer is obtained.

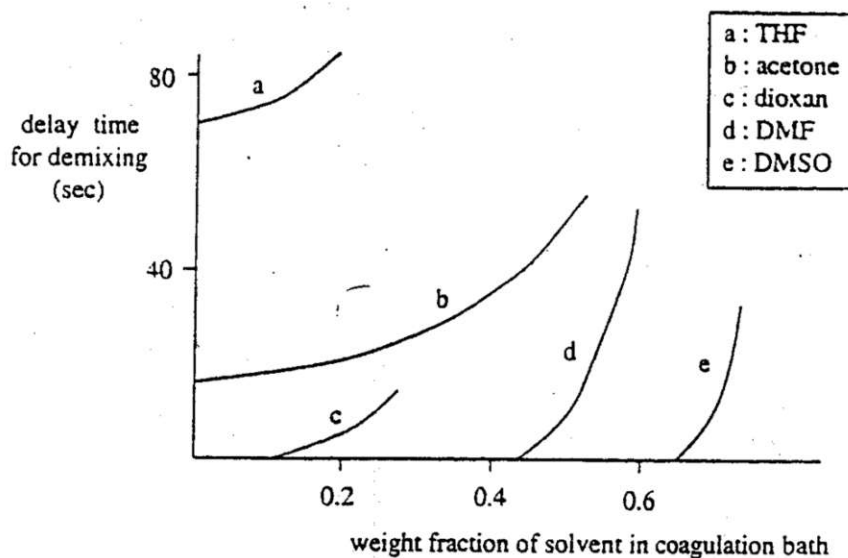


Figure 25: Delay time of demixing for 15% cellulose acetate/solvent solutions in water [3]

2.2.5.3 Additives

Additives can be added to the dope solution to improve several properties of the dope solution and the membrane produced from the dope solution. The utilisation of additives can be one of the most efficient ways to control membrane formation in the NIPS process. Pore-forming additives like polyvinylpyrrolidone (PVP) and polyethylene glycol (PEG) have been found to alter the balance between the kinetics and thermodynamics of membrane formation. High molecular weight additives are typically retained within the fibre structure, thereby changing the hydrophilicity/hydrophobicity behaviour of the membrane. One study [28], analysed that the macrovoid formation was suppressed by PVP addition. Simultaneously, however, the porosity and water permeability were observed to decrease, whereas dextran rejection and mechanical strength increased.

PEG and PVP utilised as additives can also induce thermodynamic instability and therefore promote instantaneous demixing. The result is membranes with high porosity. A number of varying additives have been found to prove useful in NIPS-processes [18]:

- i. Polymeric additives (e.g., PEG, PVP etc.)
- ii. Organic molecules (e.g., ethylene glycol)
- iii. Amphiphilic additives
- iv. Pluronic copolymers (triblock copolymers of polyethylene oxide (PEO) and polypropylene oxide (PPO))
- v. Inorganic molecules (e.g., lithium chloride)
- vi. Weak co-solvents (e.g., ethanol)
- vii. Strong nonsolvents (e.g., water)

Polymeric additives like PEG and its effects on fibre morphology and performance has also been studied. Alsahy et al. 2014 [29] observed that the addition of PEG to a PES/gamma-butyrolactone (GBL) solution increased its viscosity and led to a reduction in the solvent-nonsolvent exchange. This in turn led to a delayed demixing and a spongy membrane structure. An increase in PEG concentration increased the wall thickness of the hollow fibres. The study attributes this to an increase in the dope solution viscosity. As the viscosity increases, the effect of gravity on the fibre reduces during the airgap. As mentioned before, the PEG additive significantly increased the porosity of the hollow fibres. It is worth mentioning the increase in the PEG concentration in the dope solution increases pore size and the pore size distribution becomes narrower. Pore density showed a maximum at 10 wt% PEG. This can be explained by the fact that PEG is the deciding factor of the solvent-nonsolvent exchange and that after a certain weight percentage the dope solution is too viscous. Additionally, the PWP (pure water permeability) reaches a maximum at 10 wt% PEG with no significant increase of the BSA rejection. An increase in PEG concentration led to a decrease in the mechanical properties of the hollow fibres (elongation at break, tensile strength and Young's modulus). This is due to the high porosity induced by the PEG addition.

In contrast, Torrestiana-Sanchez et al. 1999 [30] researched the effect of PEG addition to PES/NMP fibres. Even at low PEG concentrations in the dope solution, a cross-section complete with finger-like macrovoids was seen, despite that PEG addition drastically increased the viscosity of the dope. This is indicative of

instantaneous demixing. In this study, PEG was a more optimal additive as compared to water or PVP, as fibres with PEG showed higher PWP. Changes in PWP are mostly dependant on surface porosity. It can be observed that with PEG, the fibres showed a higher PWP and thus higher surface porosity.

Different polymers may behave differently with different additives, as seen in the study by Liu et al. 1992 [31]. PES and PSf fibres with a PVP additive were spun. Both showed different fibre dimensions as well as different PWP and solute rejection rate. This is because PES and PSf consist of different morphologies that are in part due to the differing kinetics of the solvent exchange during membrane formation. PVP was shown to increase the outer/inner diameter ratio, decrease solute rejection and increase PWP. This points to a larger pore size on the lumen side. PVP addition to PSf dope composition led to a smaller outer/inner diameter ratio, decreased solute rejection and increased PWP.

Weak nonsolvents like aliphatic alcohols (methanol, ethanol and n-propanol) can also be utilised as additives to the dope solution. It was seen that the morphology changes from long and wide finger macrovoids to a spongy structure as the ethanol concentration was increased. PWP increased while solute rejection rates of multiple different solutes showed a slight rise before decreasing with increasing ethanol concentrations. This can be explained by larger pore sizes as ethanol concentrations increase [32]. Wang et al. 1996 [33] analysed five aliphatic alcohols (methanol, ethanol, 1-propanol, 1-butanol and 1-pentanol) and two polyhydric alcohols (ethylene glycol and diethylene glycol) and their effects on permeation fluxes of four gases (helium, oxygen, carbon dioxide and nitrogen) and the fibre structure. Ethanol was discovered to be the superior nonsolvent additive, with high permeabilities and selectivities.

Despite water being a strong nonsolvent for a multitude of polymer solutions, a dope solution can contain a small amount of water. Water in the dope solution brings the dope solution closer to its metastable/unstable state. This promotes and facilitates instantaneous demixing during membrane formation. Water addition also suppresses macrovoid growth. When the amount of water in the dope solution exceeds a certain critical amount, the entire system can be brought closer to the gelation point. At this point, macrovoid growth is suppressed as the nuclei are unable to develop [18], [28], [34], [35]. Water as a nonsolvent additive has also been observed to increase the viscosity of the dope solution.

2.2.5.4 Air Gap Length

The air gap length is a critical parameter in the dry-jet wet-spinning process. The air gap length is defined as the length between the spinneret end (where the fibre leaves the nozzle) and the coagulation bath. This length that the fibre spends in the air is crucial for fibre morphology and outer skin porous structure. Many studies have tried to investigate the relationship between the airgap length and the fibre morphology, performance selectivity/rejection rate and permeability.

However, there are contradicting observations amongst the studies themselves. Khayet 2003 [36] reported that airgap length had no effect on the permselectivity and performance properties of the polysulfone fibres. However, other studies [31], [37] reported that the water flux follows a particular trend. In Kim et al. 1995 [37], the water flux increases with increasing air gap length reaches a maximum and then decreases

with further increase in the air gap length. In Liu et al. 1992 [31], the water flux trend had two maxima separated by a minimum. An increase in the air gap length leads to stretching and elongating of the fibre by its own weight. The polymer aggregates move closer together and rearrange themselves into a state of higher stability. This leads to a decrease in the aggregate pore size and uniform distribution of the pores on the membrane surface on the bore fluid side. This phenomenon is the reason for the observed trend in water flux. Liu et al. 2003 [35] shows that with increasing air gap lengths, the pore size of the outside skin-layer increases and thus the water flux is also seen to increase. On the other hand, the bovine serum albumin (BSA) rejection decreases. This behaviour is due to the longer amount of time it takes until the outer skin surface separates. As soon as the nascent fibre enters the coagulation bath, instantaneous demixing occurs. The nascent fibre is penetrated by the humidity in the air and nuclei develop and expand until phase separation arrests the structure at the coagulation bath.

As already mentioned, an asymmetric membrane consists of an outer skin layer that is the selective layer and the substructure that functions as a support for the selective layer. The air gap length heavily influences the pore structure of the shell layer. Chung et al. 1997 [38] investigated the difference between PES/NMP fibres spun through dry-jet wet (air gap > 0 cm) and wet spinning (air gap = 0 cm). The study investigated that the nascent fibre experiences two different processes under the two different spinning procedures. In the dry-jet wet spinning process, the nascent fibre goes through two coagulation paths. Firstly, the fibre experiences a 'convective-type' internal coagulation followed by a 'non-convective-type' external coagulation in the air region. When the fibre is finally immersed into the coagulation bath, then rapid solvent-exchange can take place. In the wet spinning process, the fibre undergoes 'convective-type' coagulations simultaneously at the internal and external surfaces. The 'convective' term refers to the vigorousness of the coagulation process. This can be seen in Figure 26.

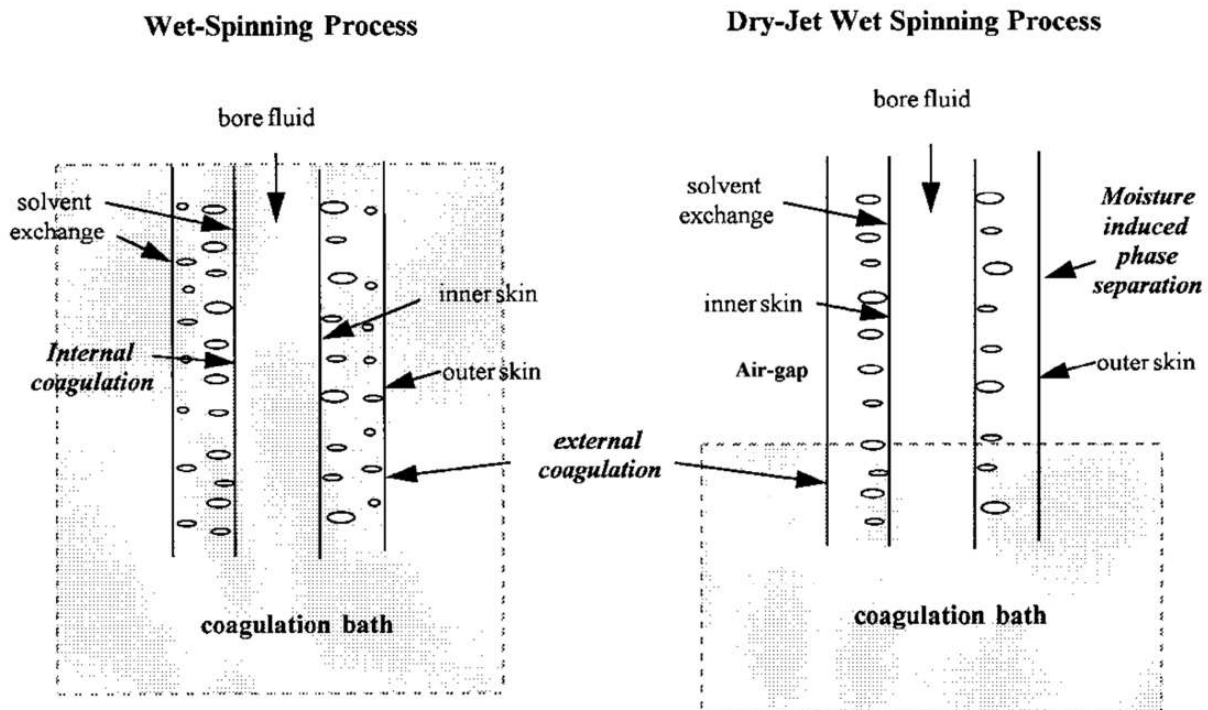


Figure 26: Precipitation in the dry-jet wet and wet spinning process [38]

The dry-jet wet spinning process is a slower process than the wet spinning, but this has a significant and irreversible effect on the fibre morphology and performance [38]. As mentioned, the dry-jet wet spinning consists of two processes in the airgap-orientation and phase separation. This study also found out that the inner and outer diameters of the fibres decrease as the airgap increases. This phenomenon is due to the elongational stresses that the fibres experience during the airgap. Gravity is responsible for such elongational stresses. A high elongational stress can pull molecular chains or phase-separated areas apart in the early stages and thus create porosity. A medium level of stress may promote molecular orientation and thus reduce molecular porosity and free volume. Permeance in this study was observed to decrease with increasing airgap lengths. This observation can also be described through the chain conformation in a ternary solution. In a solvent that has a high affinity with the polymer, the polymer chains exist as fully swollen or extended. When a nonsolvent is added to the solution, the chains contract to reduce the Gibbs' free energy. The speed of the chain contraction depends on the solvent-exchange rate and the amount of nonsolvent added into the solution. In a wet-spun fibre, the coagulation at both surfaces occurs so instantaneously, that the extended polymer chains contract suddenly and just as instantaneously. A significant amount of the solvent and nonsolvent are trapped within the contracted chains. Both inner and outer skin layers may consist of a long-range random and unoriented polymeric chain entanglement structure with some intermolecular voids [38].

On the other hand, in the dry-jet wet spinning process, the precipitation process in the airgap slows the chain contractions down. This gives the chains enough time to rearrange to a given conformation. The outer layer from such a process may depict short-range random chain entanglement in circumferential and lateral directions as well as a more oriented and stretched structure in the axial direction [38].

In other studies [39], [40], the increase in the air gap was observed to lead to a thicker outer surface. The study observed a certain balance in the airgap length. The spinning process became much harder when the airgap length was excessively long (>30 cm). The frequency of the fibre membrane breaking increased significantly.

Other studies [36], [41], [42] reported a decrease in permeance and increasing selectivities with increasing airgap lengths. Khayet 2003 [36] observed this effect with a dope solution of PVDF/ethylene glycol/DMAc with ethanol aqueous solution as the bore fluid and external coagulant. The skin layer thickness affects the membrane performance. Solvent evaporation during the airgap and solvent-nonsolvent exchange is responsible for the behaviour of the skin layer formation during the dry-jet wet and wet spinning processes respectively. Fibres spun with higher airgaps (>45 cm) depict a tighter cross-section as compared to fibres spun with lower airgaps. The behaviour of the outer skin layer and the polymer chain entanglement conformation occurs in the same way as described by Chung et al. 1997 [38]. The UF experiments performed in the study illustrate that a higher airgap length leads to hollow fibre membranes with smaller pore sizes. A greater molecular orientation and tighter molecular packing are responsible for such a membrane. Thus, permeability decreases but the separation performance increases. This observation also illuminates the fact that both surfaces of the hollow fibre play a role in the UF performance.

Wang et al. 2002 [41] studied hollow fibre membranes produced from PSf (polysulfone) with an NMP (N-methyl-2-pyrrolidone)/water and an NMP/ethanol

system. Water was utilised as the external coagulant. Gas separation was used as a test for performance. Airgaps of 5 or 10 cm show high selectivities but low permeabilities. Wienk et al. 1995 [42] also report the effect of gravity on the nascent fibre to be more pronounced as the airgap length increases. The dimensions of the fibre decrease as the air gap increases. However, Alsalhy et al. 2014 [29] states that the presence of an air gap tends to reduce the dimensions of the nascent fibre and increase porosity.

However, as mentioned, many studies on the effect of the air gap length on fibre morphology and performance conflict with each other. Another study [43], investigated hollow fibres made from a PES and PI blend and the effect of the air gap length on the hollow fibre structure and performance. The permeances of nitrogen and carbon dioxide were tested for uncoated and PDMS-coated fibres. An increase in air gap length, in this study, was observed with higher permeances of both gases for the uncoated fibres. The same was observed for the coated fibres, albeit the increase was a lot less significant. Selectivity here showed a decrease with airgap for the uncoated fibres. The decrease was, similarly, less significant for the coated fibres. This behaviour in the study was explained to be due to the porous and loose skin layer with increasing airgap lengths.

Lastly, an air gap is observed to have three primary effects on hollow fibres [44]:

- i. Creating phase instability
- ii. Promoting phase separation
- iii. Generating orientation

It is evident from most studies that the water flux and the solute rejection go hand-in-hand with each other. A compromise needs to be struck between an optimum flux and selectivity. Airgap length is imperative in the fibre morphology of the shell surface and thus is an important parameter for permselectivity properties and performance.

2.2.5.5 Bore Fluid Composition and Flowrate

Two more important parameters that heavily influences fibre morphology, performance and mechanical structure of the fibres are the bore fluid composition and flow rate. The bore fluid acts as an internal coagulant to the hollow fibres. A very typical fluid utilised as the bore fluid is water. Other nonsolvents include ethanol, isopropanol and the same solvents can be utilised as the bore fluid as well. The type of bore fluid depends on the type of demixing and fibre morphology that is desired.

Hollow fibre coagulation is much more complicated than their flat-sheet counterparts- coagulation in hollow fibre production occur on two surfaces as an internal (bore fluid) and an external coagulant is necessary. The presence of two coagulants affects the thermodynamics and the kinetics of the phase separation. A few factors are crucial for the phase separation of the inner surface: nonsolvent power, mutual affinity between the nonsolvent and solvent, solubility parameter differences between P-NS and S-Ns, solvent and nonsolvent diffusivities dependent on molecular size and temperature [18].

Multiple studies [18], [29], [35], [39], [44]–[46] have investigated the effect of bore fluid composition and type on the fibres' morphology and structure. While the air gap length is primarily responsible for the morphology and pore structure on the shell side (outer skin-layer), the bore fluid composition, type and speed are primarily

responsible for the morphology and pore structure of the lumen side (inner skin-layer). Somewhat conflicting observations are reported again with this phenomenon. This points even more to the fact that the spinning NIPS process still requires much careful experimentation, modelling and development.

Typically, depending on the application of the spun hollow fibres, solvents or nonsolvents are utilised as bore fluids. The general trend in the literature [29], [39] shows that the stronger the nonsolvents (for the particular polymer and solvent; e.g., water), a dense inner layer with almost non-existent pores and thus decreased permeance and increased solute rejection is seen. With increasing concentrations of a non-solvent, the same trend [39], [45] is to be observed.

The opposite trend [18], [35], [45] is seen when solvents are used as bore fluids. With increasing concentrations of solvents in the bore fluid, a thicker but more open porous structure is observed on the lumen side and thus increased permeance and decreased solute rejection is seen. Bang et al. 2020 [45] studied the influence of the bore fluid composition, type and flow rate on the fibre morphology, pore structure, size and density and UF properties for PSf/NMP/PVP fibres with different bore fluids: deionized water and solutions of varying compositions of water with NMP, EG and glycerin (G).

The studies [35], [45], [47] have shown that a general increase of solvent concentration in the bore fluid leads to increasing pore sizes and porosities. This was attributed to the type of L-L demixing occurring during phase separation. As shown in Figure 27, the binodal was closer to the P-S axis, when water was used. Instantaneous L-L demixing occurred because the solubility parameters of P and NS were very different. As mentioned before, this implies that only a small amount of water is needed to bring about precipitation. Non-solvent tolerance was profoundly increased when NMP was added to the bore fluid. Adding a solvent like NMP moves the binodal away from the P-S axis, thus reducing the effectiveness of the NMP/water mixture as a nonsolvent. Increasing the solvent (NMP) concentrations moved the binodal even further away from the P-S axis, thus lowering the precipitation rate and delaying the L-L demixing. The same is observed for G and EG, whereby the NMP/water bore fluid delayed the demixing the most. Based on the results of [35], [47], the same can be concluded for a PEG/water and DMAc/water solutions as the bore fluids.

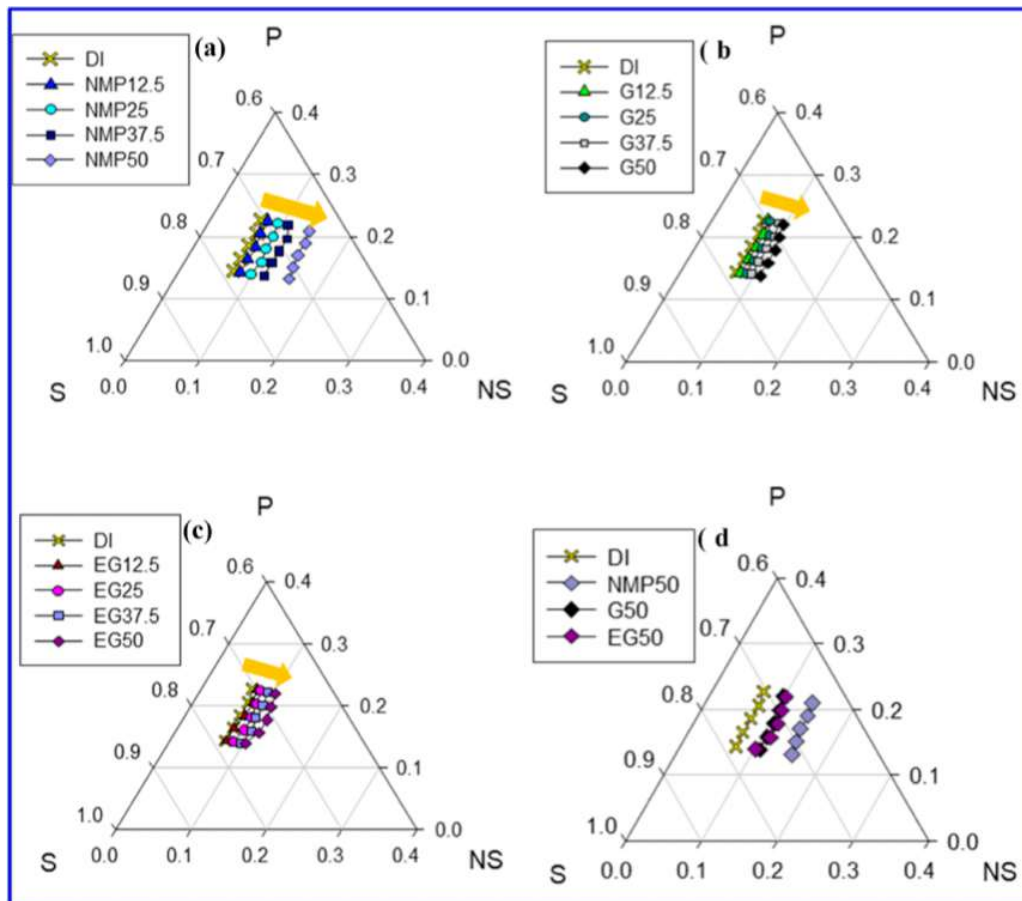


Figure 27: Effect of bore fluid composition on the ternary phase diagram: (a) NMP/water (b) G/water (c) EG/water and (d) comparison of the binodal for membranes made with different bore fluids [45]

Bang et al. 2020 [45] and Wang et al. 2000, 2002 [41], [46] discussed that with increasing concentrations of NMP, an irregularity with the circular form was to be observed due to the slower precipitation rates. It was also noticed that the viscosity of the bore fluid plays a factor in the irregular shape as well, as the effect was much more pronounced with G/water as bore fluid. Finger-like macrovoids were seen to be somewhat suppressed as the solvent concentrations in the bore fluid increased. The inner surface showed the biggest difference- for all solvents in the bore fluid a porous surface was observed. An increase in pore size and density and porosity was also detected for all solvents as well. Mechanical properties of the fibres showed a specific trend. The tensile strength and elongation upon breakage decreased but then showed a maximum at 50/50 NMP/water. Similar trends were noticed with the other solvents in the study. This is thought to be due to the increased thickness of the inner layer and the creation of a spongy structure just underneath. Water permeability increased with increasing solvent concentration, with 50/50 NMP/water showing the highest PWP. This is due to the delayed demixing, resulting in a porous and thick inner skin-layer.

An important compromise exists here between the pore size and the thickness of the inner layer. The thicker the inner layer, the more resistance there is towards the hydraulic pressure, thus decreasing water flux. A membrane with higher porosity, wide finger-like pores, a high surface pore size on the inner surface layer and no interface layer between the macrovoids might show less resistance to water permeance. Thus, resulting in higher water fluxes [45].

Moving on, the other aspect of bore fluid composition to be examined is the addition of other nonsolvents to the bore fluid. Typically, the bore fluid of choice is water and multiple nonsolvents like ethanol, isopropanol, acetone etc. can be added. Alsahy et al. 2014 [29] utilised different mixtures of water with ethanol and isopropanol, while Li et al. 2020 [39] utilised mixtures of water with isopropanol, ethanol and acetone. While both studies do not essentially contradict each other, Alsahy et al. 2014 [29] make a certain assumption to validate their results (spinning with a dope solution with a viscosity higher than 1250 cp and under a presence of a steam gap). There is little difference seen in the cross-sectional morphology. However, the biggest difference again can be seen on the inner surface. While similar results were reported for pure water, it was observed that a significant pore distribution, pore density and pore size was seen for the ethanol/water mixture. This is to be attributed to the fact that ethanol is a weak nonsolvent and the addition of ethanol to the bore fluid delays the demixing process and the diffusion rates between solvent in the dope solution and the nonsolvent in the bore fluid. The highest permeabilities were achieved with the ethanol/water mixture, and the lowest for pure water. However, solute rejection rates showed the opposite trend. In this case, thicker membranes were observed with pure water as the bore fluid and thus were the most mechanically stable. Here the opposite effect is observed as compared to adding solvents to the bore fluid.

The same study [29] utilised pure water at three different bore fluid flow rates to study its effect on fibre morphology, porosity, fibre dimensions, UF performance and mechanical properties. The flow rate had no significant effect on the structural morphology. However, a significant effect was noted on the dimensions of the fibres—increased outer and inner diameters with a diminished wall thickness. It was also noted that increasing bore fluid flow rates decreased the inner skin-layer thickness and the pore sizes of the inner layer. No real change in porosity was observed. However, pore sizes decreased due to the slow solidification of the inner surface that restricts water diffusion through the membrane wall. Pore density saw an initial decrease followed by a pronounced increase. This can be attributed to a reduction of closed-end pores with decreasing wall thickness.

UF here was carried out from the lumen side and the permeate collected from the shell side, as the layer to be tested was the inner skin-layer (lumen). PWP increased with increasing flow rates, due to the increase in pore density and decrease in wall thickness. The rejection ratio was seen to decrease. The PWP and solute rejection are primarily controlled, as mentioned before, by the pore density and wall thickness of the hollow fibre membranes. Mechanical strength here was predominantly controlled by the wall thickness, pore size and distribution.

2.2.5.6 Coagulation Bath Composition

Since two surfaces are involved in coagulation, both internal and external coagulants need to be examined and studied so that their effects on fibre morphology, pore structure, performance and mechanical stability can be analysed. Having closely examined the role of the inner coagulant (the bore fluid), the external coagulant (existent in the hollow fibre process as the coagulation bath) can be examined as well. The composition and type of the coagulant present in the coagulation bath has a profound effect on membrane morphology. Typically, water is used as the external

coagulant as it is a strong nonsolvent for many polymers. The phase separation here leads to conclusions similar to the previous unit.

2.2.5.7 Coagulation Bath Temperature

Along with the composition and type of coagulant used in the coagulation bath, the temperature of the coagulation bath plays an important role in the spinning of hollow fibre membranes. It is obvious that with higher temperatures of the coagulation bath, more humidity will be present in the air gap, thus greatly affecting fibres' morphology and surface structure. The temperatures of both the bore fluid and the coagulation bath effects the interdiffusion between the solvent and nonsolvent at the fibre walls. This phenomenon heavily affects the kinetics of phase separation [18]. Again, contradicting literature can be found regarding the effects of the coagulation bath temperature on hollow fibre spinning.

Wienk et al. 1995 [42] discussed this behaviour and the effect of such conditions on the spun PES/PVP fibres. Due to the higher coagulation bath temperature, more humidity and a higher temperature were evident in the air gap, thus resulting in greatly different fibres. At 44 °C, the fibre was observed to be more susceptible to stretching. Fibre dimensions at this coagulation bath temperature were also lower. Membranes produced with 44 °C coagulation bath temperature showed higher water fluxes with lower retention rates. As the temperature is higher in the coagulation bath, more vapour pressure is present in the air gap and the growth and development of the nuclei is faster because of the higher diffusion coefficients. Pore sizes are expected to be larger at a higher temperature.

Chung and Kafchinski 1997 [44] discuss that with increasing coagulation bath temperatures, the 6FDA/6FDAM fibres change from having sharp and clear finger-like pores with a tightly packed cross-section structure to a more looser cross-section morphology at room temperature. At higher temperatures, the fibres are fully porous and contain no finger-like pores. The study suggests that the finger-like pores may occur due to unbalanced localized stresses at lower temperatures. At higher temperatures (>20 °C), solubilities and diffusivities increase and thus may cause the spinodal curve to move towards the P-NS axis. Higher coagulation bath temperatures may lead to lower dope solution viscosity, chain rigidity, surface tension and reduction of unbalanced localized stresses that promote instantaneous demixing. The study suggests that at different temperatures, different paths are taken through the ternary phase diagram, which would suggest the differing morphology at different temperatures.

On the other hand, Wang et al. 2002 [41] reports that with decreasing coagulation bath temperatures, the permeability of all gases tested (helium, oxygen, and carbon dioxide) increases, while the selectivity is observed to sink. The study observed that at coagulation bath temperatures of 10-15 °C, the PSf fibres depicted large surface porosities, that could not be repaired with silicone coating. Initial phase separation is the most important process to control outer skin layer formation. With lower coagulation bath temperatures, a decrease in macrovoid formation is also observed. The study suggests that this behaviour is attributed to an increased precipitation rate.

Choi et al. 2010 [27] discovered that smaller surface pores and macrovoids were formed in PVDF membranes at high coagulation bath temperatures. However, Tang et

al. 2021 [48] noted the complete opposite occurrence. Larger surface pores and macrovoids at higher coagulation bath temperatures were observed in PVDF and cellulose acetate membranes.

2.2.5.8 Dope Extrusion Rate (DER)

Similar to how the bore fluid flow rate affects morphology and fibre structure, so does the dope extrusion speed (analogous to the shear rate within the spinneret). Plenty of examination has been made on spinning parameters that occur outside of the spinneret e.g., dope composition, coagulation bath and bore fluid, temperature etc. However, the inner workings and mechanisms of the spinneret are just as important. There are two dominant mechanisms that dictate molecular orientation during membrane formation. The first is the elongational stress due to gravity and spin line stresses. The second is the shear and elongation stress within the spinneret. It is increasingly difficult to decouple the effects of shear, elongation, gravity, and coagulation effects on fibre formation. Several studies have analysed the effect of the dope extrusion rate and its effect on gas permeation rate and selectivity [49]. This aspect of fibre spinning has not been examined as deeply as other aspects of fibre spinning have. Many studies [49], [50] analysing this parameter usually wet spin the fibres, so as to significantly reduce the effects of gravity and elongational stress on the fibres and to freeze the molecular orientation induced by the shear stress into the wet-spun fibres.

To decouple the effects of the inner skin in this study [49], a suitable bore fluid was used to promote delayed demixing. Thus, this type of demixing created an interconnected open-cell structure. The outer skin-layer was dense due to instantaneous demixing, regardless of the magnitude of the dope extrusion rate. The outer skin-layers were seen to be thicker and denser with higher DERs. Higher shear rates resulted in the PES/PVP/NMP hollow fibres with smaller pore sizes and denser skins due to the greater molecular orientation. Such membranes show lower permeability but higher solute rejection. Most crucially, the study found a specific critical DER above which the separation of the spun fibres is not dramatically influenced by the DER. Mechanical stability was seen to also be affected by the DER. The tensile strength at break and Young's modulus of the fibres increases but the elongation at break decreases with higher DERs. This is attributed to the greater molecular orientation and more closely packed molecular chain in the shear direction. Other studies [50]–[52] confirmed these results and came to similar conclusions.

2.2.5.9 Take-up Speed

Another factor that is quite important in the spinning process is the take-up speed. The take-up speed relies heavily on the polymer and the coagulation bath used. The take-up speed itself influences the properties of the freshly spun fibre, by affecting the size of the surface pores of the fibre.

If the take-up speed is slower than the free fall velocity of the fibre, then the possibility of the nascent fibre deforming or clinging to the coagulation bath walls is relatively high. If, on the other hand, the take-up speed is significantly higher than the free fall velocity of the fibre, then the tensile stress in the fibre is almost zero [53]. Starting from this point on, the increase in velocity leads to an increase in the tensile stress in the hollow fibre. This is because the winder drum transfers higher tensile

forces. This causes elongation and constriction of the fibre and a decrease in fibre dimension. Additionally, a high take-up speed leads to a reduction in the residence time of the fibre in the coagulation bath. This leads to changes in the polymer chain orientation and density, which cause reduced permeance [4].

Another effect to consider is that if the take-up speed is too high, then the residence time of the fibre in the coagulation bath is not long enough to fully undergo crystallisation. The tensile forces transferred by the winder drum lead to an increase of tensile strength in the fibre until it reaches a maximum and exceeds the maximum tensile strength of the fibre. At this point, the fibre will break.

Literature [18] has also found contradictory effects of take-up speed on the fibres. Some report that smaller surface pores are observed with higher take-up speeds due to many reasons. Changes in the dope might occur by elongation stress, polymer concentration might increase as solvent is diffused outward, or spinodal decomposition occurs as the elongation stress provokes thermodynamic instability of the dope solution. Other literature [54] reports a higher surface pore size with higher take-up speeds as it is assumed that merging of pores or defects expansion may occur.

3 Materials and Methodology

The purpose of this thesis is to document the process of producing and testing lab-scale hollow fibre membranes with the newly built in-house modular NIPS process plant. As the in-house modular NIPS plant had just been built ready for operation, it was necessary to test the fibres for their morphology and pore structure first, before testing the ultrafiltration or gas separation properties. However, as the spinning plant was utilized more and more, fibres were spun that illustrated favourable permeance and selectivity properties.

To answer the main research question of this thesis and to produce lab-scale hollow fibre membranes, the methodology outlined in the next unit was utilised. Such methodology, design and approach were inspired by various literature papers and research articles that have developed their laboratory-scale productions of hollow fibre membranes.

3.1 Dope Solution

3.1.1 Dope Solution Materials

Polyethersulfone (PES; mixed molecular weight) was purchased in pellet form and synthetic grade solvent 1-methyl-2-pyrrolidone (99,8% NMP; molecular weight 99,13 g/mol) were purchased from VWR and used without any further processing. PES and NMP are the two key components in the dope solution to produce hollow fibre membranes in this process. Polyethylene glycol (molecular weight 10 000 g/mol) was acquired from the university chemical database in powder form. Deionised water (Arium water purification system, Sartorius AG, Goettingen, Germany) was utilised in the dope solution.

3.1.2 Dope Solution Production Plant

Since it was of the utmost importance to create a starting dope mixture with the complete absence of any water or humidity, the PES pellets were dried at about 150 °C in a heating oven for 24 hours. They were then placed in an airtight container for further use.

After drying the PES pellets, they were used to create the dope solution. Figure 28 shows the setup of this process and the finished homogenous PES/NMP dope solution. 1-methyl-2-pyrrolidone (NMP) solvent was added into a triple-necked round-bottom flask and was slowly heated to a maximum of 70 °C, using a heating mantle and under constant stirring with a blade stirrer. To avoid any solvent loss through evaporation, a Dimroth condenser was used on one of the necks of the round-bottom flask. A thermoelement is attached to the far-right neck of the flask to measure and keep track of the temperature reliably. As the solution mustn't exceed 80 °C, a way to track temperature here is necessary. This is partially due to safety reasons, as the flash point of NMP is at 91 °C and partially due to the fact that the solution is prepared faster at higher temperatures.

PES pellets were then slowly added into the hot NMP. PES pellets are prone to agglomerate and create large agglomerates in the NMP; they must be added slowly and in batches instead of all at once. This dope solution was then left to dissolve for around 48 hours under constant stirring at 70 °C. For the production of around 500 mL

of dope solution consisting of 31 wt% of PES, 200 g of PES and 447 g of NMP are mixed together.

After the solution was completely homogenous, the dope solution was filled into an airtight glass bottle for further experimentation.



Figure 28: (a) Dope solution production process: heating mantle (1), triple-necked round-bottom flask (2), Dimroth condenser (3), Stirring motor (4), Thermolement (5) (left); (b) Polyethersulfone/1-methyl-2-pyrrolidone dope solution (top right); (c) Polyethersulfone pellets (bottom right)

3.1.3 Density of Dope Solution

A small portion of the dope solution (20 mL) was taken out to measure the density of the solution. The density was calculated by weighing the dope solution in a measuring cylinder and using the following equation:

$$\text{Density } \rho = \frac{\text{Mass}}{\text{Volume}}$$

Equation 45: Density of a liquid

After the density was calculated, the viscosity of the dope solution could be measured.

3.1.4 Viscosity of Dope Solution

The viscosity was measured by the rheometer (RM180, Kassecker Engineering, Riemerling, Germany) for different temperatures with constant shear rates and vice versa.

3.2 NIPS-Process

3.2.1 NIPS-Process Materials

3.2.1.1 Dope Solutions

The majority of the experiments were performed with a PES/NMP dope. Certain experiments utilised dope solutions with additives such as PEG and water. The dope solutions utilised are outlined in Table 7.

Table 7: Overview of dope solutions used; *data linearly extrapolated

Dope	Dope Composition	PES [wt%]	NMP [wt%]	PEG 10000 [wt%]	H ₂ O [wt%]	Density [g/cm ³]	Viscosity [Pa*s] at 65 °C
A	PES/NMP	20	80	-	-	1,099	0,952
B	PES/NMP	25	75	-	-	1,100	1,170
C	PES/NMP	27	73	-	-	1,109*	1,4*
D	PES/NMP	31	69	-	-	1,128	1,870
E	PES/PEG/NMP	19,7	68,4	12	-	-	-
F	PES/PEG/NMP/ Water	20	70	5	5	1,024	0,339
G	PES/NMP/Water	31	64,4	-	4,6	1,210	1,770
H	PES/NMP/Water	31	61,9	-	7,1	1,040	1,900

3.2.1.2 Bore Fluids

Deionised water was obtained from the laboratory (Arium water purification system, Sartorius AG, Goettingen, Germany) and used as the bore fluid in the production process. A mixture of NMP and water was also used for certain experiments (Table 8).

3.2.2 NIPS-Process Plant

The rest of the dope solution is finally used for this thesis's primary purpose- to create hollow fibre membranes using the non-solvent induced phase separation (NIPS) method. Figure 29 shows the set-up of the equipment used.

The heating, coagulation and wash baths are all filled with distilled water. The pumps are filled with the dope solution and the bore fluid. Pump 1 (on the left side) is the dope pump, and Pump 2 is filled with deionised water and acts as the pump for the bore fluid. Both pumps are designed for a continuous and steady temperature control, chemical resistance, and a maximum operating pressure of 100 bar. Due to the build of the pump station, an operation with a wide range of polymers, pressures and dope viscosities is ensured.

These injection pumps are attached to the spinneret through insulated pipes (insulated with polyurethane foam) and lead to the spinneret, through which the hollow fibres are extruded. The flow rate at which the dope and the bore fluid flow can be controlled by pump regulation system. The pump regulation displays the amount of

dope and bore fluid in the pumps and the set flow rates. The flow rates can be changed by dialing the knobs on the pump regulation system.

The fibres that are extruded from the annular shaped spinneret pass through either an airgap or immediately in the coagulation bath. Regardless, this is where the diffusion process of the solvent and the nonsolvent takes place and phase separation begins. The spinneret can have different dimensions, depending on the specifications and the dimensions of the resulting hollow fibre membrane. Two different spinnerets were utilised in this paper- one spinneret (S1) with an outer diameter of 600 μm and an inner diameter of 400 μm and a second spinneret (S2) with an outer diameter of 800 μm and an inner diameter of 500 μm .

The fibres are then guided through the coagulation bath and taken up by the winder drum, which is programmed to achieve different take-up speeds. This bath (separated by a glass wall from the coagulation bath) also serves as a wash and rinse bath for the fibres. This is the part of the process where solvent exchange continues to take place, even after the spinning process. Thus, by changing the composition, flow rates, and temperature of the dope solution, the bore fluid, the spinneret, the coagulation bath, the wash bath, the take-up speed, the distance of the spinneret from the coagulation water (airgap), drastically different hollow fibres can be produced with other performances and applications.

The parameters that were studied in this thesis and the spinning experiments performed are outlined in Table 8. The coagulation bath consisted of distilled water and apart from the one experiment where the effect of bore fluid composition was observed (Identifiers B_0NMP and B_50NMP), the bore fluid utilised was deionized water. Coagulation bath temperature was kept at 22 °C, except for the experiment where the effect of the coagulation bath temperature was studied (Identifiers DCT_25_1, DCT_25_2, DCT_45_1 and DCT_45_2). Bore fluid temperature was kept constant at 50 °C for all experiments. The spinneret and dope temperatures were always set to identical values. Airgap was kept constant at 260 mm, unless stated explicitly otherwise. The same spinneret was used across every identifier in each experiment, e.g., S2 was used for all three identifiers in the airgap variation experiment and both identifiers in the bore fluid composition variation. S1 was utilised for all other experiments.

3.2.1 Post Treatment of Fibres

Fibres spun were always treated by keeping them in water for at least 24 hrs. Depending on the experiment, different post-treatments were performed, where the fibres spent a few hours in a nonsolvent/solvent to improve the characteristics of the spun fibres. Certain fibres (Identifier C_PDMS40) were also coated using a solution of 3 wt% of polydimethylsiloxane (PDMS) in pentane, followed by a subsequent drying step.

Table 8: Spinning parameters with different spinning dopes for different experiments performed; Key: Spinning Dope_Unique ParameterToBeTested, e.g., B_ST30 = dope B spun at spinneret temperature 30 °C; BFF: bore fluid flowrate; AG: airgap; CT: coagulation bath temperature

Spinneret Temperature Variation						
Identifier	Spinneret Temperature [°C]	Dope Flow Rate [µl/min]	Bore Fluid Flow Rate [µl/min]	Flow	Take-Up Speed [mm/s]	
A_40	40	59	59		73	
B_ST30	30	59	59		56	
B_ST40	40	59	59		58	
B_ST50	50	59	59		63	
B_ST65	65	59	59		75	
C_40	40	59	59		66	
C_PDMS40	40	59	59		66	
C_65	65	59	59		73	
E_40	40	59	59		169	
F_40	40	59	59		186	
D_BFF0,12	50	59	120		172	
D_BFF0,24	50	120	240		317	
D_BFF0,36	50	120	360		344	
D_40	40	59	59		105	

Airgap Variation				
Identifier	Air Gap [mm]	Dope Flow Rate [µl/min]	Bore Fluid Flow Rate [µl/min]	Take-Up Speed [mm/s]
B_AG65	65	115,1	92,7	73
B_AG130	130	115,1	92,7	73
B_AG260	260	115,1	92,7	73

Bore Fluid Composition Variation					
Identifier	Air Gap [mm]	Bore Fluid	Dope Flow Rate [µl/min]	Bore Fluid Flow Rate [µl/min]	Take-Up Speed [mm/s]
B_ONMP	65	deionised H ₂ O	115,1	92,7	73
B_50NMP	65	deionised H ₂ O/NMP 50/50 wt%	115,1	92,7	70

Coagulation Bath Temperature Variation						
Identifier	Coagulation Bath Temperature [°C]	Dope Flow Rate [µl/min]	Flow	Bore Fluid Flow Rate [µl/min]	Take-Up Speed [mm/s]	
DCT_25_1	25	120		240	317	
DCT_25_2	25	59		59	60	
DCT_45_1	45	120		240	306	
DCT_45_2	45	59		59	60	

3.3 Membrane Characterization

3.3.1 SEM Analysis

The spun hollow fibres were first broken with liquid nitrogen to provide for a clean cross section, with most of the pore structure intact. The fibres are then prepared

onto a sample holder and sputtered with the ion coater (Coxem SPT-20, Yuseong-gu, Korea) followed by being looked at under a scanning electron microscope (Coxem E-30Plus, Yuseong-gu, Korea and FEI Quanta250 FEG, Thermo Fischer, Waltham, USA) so that the porous structure, the lumen, and the walls can be accurately seen and measured.

3.3.2 Porosity

The first method utilized measures the geometric porosity (porosity based on the geometric structure and diameters) of a fibre. A small piece of fibre is weighed using an analytical weighing scale (Kern, Germany). This weight, in addition to the SEM images, is utilized to calculate the geometric porosity. Firstly, the mass of a nonporous cylinder of the same dimensions as the spun fibre is calculated using the polymer density. The porosity can be calculated through the ratio of the difference in weight of the fibre and the nonporous cylinder and the cylinder weight.

The second method is widely outlined in literature [29], [45], [55]. Small lengths of fibre are cut, and the length of each segment is measured. Each fibre segment is then weighed on an analytical weighing scale and immersed in isopropanol for an extended period (24 h to 144 h). The fibre segments are then taken out of the isopropanol and quickly weighed again. This difference in weight (and the consideration of some isopropanol in the lumen) can be used to calculate the volumetric porosity. Further discussion about the two methods will be carried out in a later unit.



Figure 29: The spinning equipment for the production of hollow fibre membranes: convective thermostats for the dope solution (1), for the bore fluid (2) and the spinneret (3), motors and gearbox for the pumps (4), dope solution pump (5), bore fluid pump (6), pump regulation (7), bore fluid supply pipe (8), polymer supply pipe (9), spinneret (10), spinneret heating pipes (11), coagulation bath (12), fibre with a deflection roller (13), take-up conduction (14), take-up winder drum (15), take-up regulation (16), wash bath (17), convection thermostat for the baths (18), emergency switch (19), safety and electrical box of the equipment (20).

3.3.3 Membrane Module Production

To test the performance of the hollow fibre membranes spun on to the drum are then checked for any surface imperfections (obvious kinks, sharp bends, anything that prevents the unhindered flow of fluid through the membranes) and then assembled in a module, as shown in Figure 30.

The module building process started with spinning fibres onto the winder drum. After a suitable post-treatment, the fibres are then collected, checked for surface imperfections, and then placed one by one on a black PTFE glass fabric mat. The fibres were rolled into a cylindrical shape and placed into the module housing. Having sufficiently stretched and adjusted them in the center of the housing, the fibres were potted on both sides with Araldite 2028-1 (polyurethane two-phase epoxy resin glue, Huntsman International LLC, Utah, USA).

Modules of differing lengths were used, determined by the availability of the parts, ranging from 13,5 cm to 15 cm. This length refers to the effective length of the module- from the edge of one shell opening to the other. This length was taken for all calculations as the fibres before the shell openings are encased in the epoxy resin and thus are not considered to be the effective in the ultrafiltration and gas separation tests. Depending on the spinning process, the number of fibres potted in a module differ as well, ranging from 15 to 20 fibres.



Figure 30: Module of 25 hollow fibres; complete module (far left), view from the lumen (centre) and view from the shell side (far right)

The module building process was optimised when one of the same plastic black mats were taped to the winder drum. The fibres were spun with a specific distance to each other. This facilitated the building process as it was no longer necessary to place fibres one by one on the black mat. After the fibres were transferred from the black mat, the rest of the process was carried out analogously to the previous process. The modules were tested with the ultrafiltration or gas separation units.

It is crucial that the modules built are tight, and that the fibres are stretched before they are potted. This is to avoid collapsing of the fibres onto one another at high pressures, as this can affect the measured permeance of the fibres. However, this also presents a problem- fibres stretched too tight can lead to earlier and easier rupture of fibres, as well as damage to the pore structure. Thus, again a compromise needs to be met.

3.3.4 Ultrafiltration Tests

3.3.4.1 Test Set-Up

These modules are then fitted with 6 mm fittings on all four sides so that they can be tested. Figure 31 displays the ultrafiltration unit that was built in-house (E166-02-2).

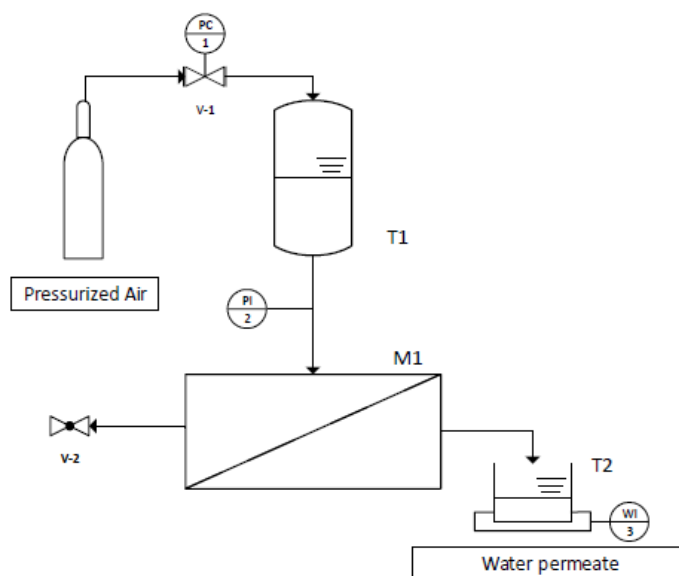


Figure 31: The ultrafiltration unit (left) pressurized air connection (1), pressure indicator (2), feed tank (3), flow indicators (4), needle valves (5), membrane module (6), permeate tank (7), extra tank for a feed (for dead-end configuration)/retentate tank (8), weighing scale (9); flow chart of the ultrafiltration unit built to determine pure water permeance (right)

A membrane module is connected to a reservoir tank through the feed side, where the hydrostatic pressure is controlled by applying pressurized air to the tank. The resulting pressure difference leads to the water from the shell side permeating through the membrane and is released through the lumen side into the beaker on top of the weighing scale. The permeate can be thus, measured either by its volume or its weight.

The tank can be filled with a solution of bovine serum albumin (MW = 66 000 g/mol; purchased from Carl Roth) and water, which is used to test the solute rejection rate for the membranes. The amount of BSA in the permeate is the deciding factor for the membranes' performance. The lower the concentration of the BSA in the permeate, the higher the solute rejection rate is, which is what is desired of the membranes. The permeate is then collected into small samples and examined using a UV/VIS spectrometer to determine the BSA concentration in the permeate.

3.3.4.2 UV/VIS Spectroscopy

Samples are taken of the fluid from the feed and permeate sides and the BSA concentrations are determined using a UV/VIS spectrometer (UV-1800, Shimadzu, Kyoto, Japan). To be able to calculate the concentration from the signal of the spectrometer, a calibration using a set concentration is necessary.

In two glass sample containers, deionized water is added to create a baseline. Using a sample from the feed BSA solution, the UV/VIS machine is calibrated. One sample from the feed and multiple samples from the permeate are collected and their UV absorption spectrum is recorded, as shown in Figure 36.

3.3.5 Gas Separation Tests

The build module was also tested with the in-house (E-166-02-2) gas separation unit. The module is attached at the feed, retentate and permeate sides. The gas separation is performed with pure gases and in a dead-end operation. Pure gas (nitrogen, carbon dioxide or oxygen) under a certain pressure flows through the mass flow counter (MFC). The mass flow of the gas can be controlled by the MFC. The gas is then led through the feed into the module through the shell side. The retentate side valves are closed. Thus, the gas makes its way by diffusing into the lumen. It is collected from the permeate side and led through a definer, that measures the flow rate of the permeate. The pressure sensors at each feed, retentate and permeate side display the pressure, which can be adjusted by adjusting the MFC value. The gas separation unit is shown in Figure 32.

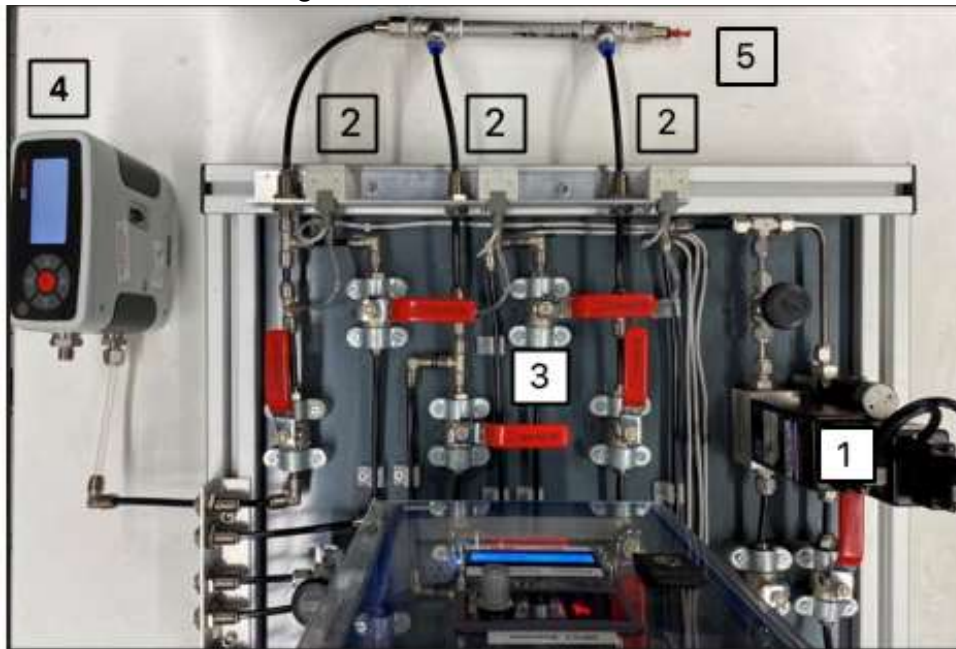


Figure 32: Gas separation unit with MFC (1), pressure sensors (2), steel valves (3), definer (4) and the membrane module (5)

3.3.6 Stress and Tensile Tests

The mechanical stability is an important characteristic of a hollow fibre. Fibres experience pressures of up to 3-5 bar in ultrafiltration and gas separation tests without any mechanical failure.

Fibre segments were taken and placed in a stress strain test equipment and tensile tests were performed, until the segment underwent breakage. The elongation of the fibres and the applied force were recorded. Using this information and the cross-sectional area of the fibre segment, the stress could be calculated.

4 Results

4.1 Viscosity of The Dope Solution

The viscosity of the dope solution has an influential role in the spinning process, morphology, and pore structure of hollow fibres. Thus, it was deemed of importance to measure the viscosity of the spinning dopes utilized for spinning. It was also deemed of value to observe the trend of PES concentration on the dope viscosity. Dope viscosity plays an important role in the fibre morphology and the type of demixing and precipitation that leads to the end result.

It can be established from Figure 33, that with increasing temperatures, the dope viscosity decreases. An increase in PES concentration leads to the opposite effect. Dope viscosity is observed to increase as the concentration of PES in the dope solution is increased (Figure 34). This, as literature suggests [1], [3], [56], is due to the higher number of PES macromolecules in the dope solution, thus increasing the dope viscosity. Figure 33 shows an interesting trend in viscosity with temperature for spinning dope B. This is most probably a typing/noting down error, which is explained later in 5.1.

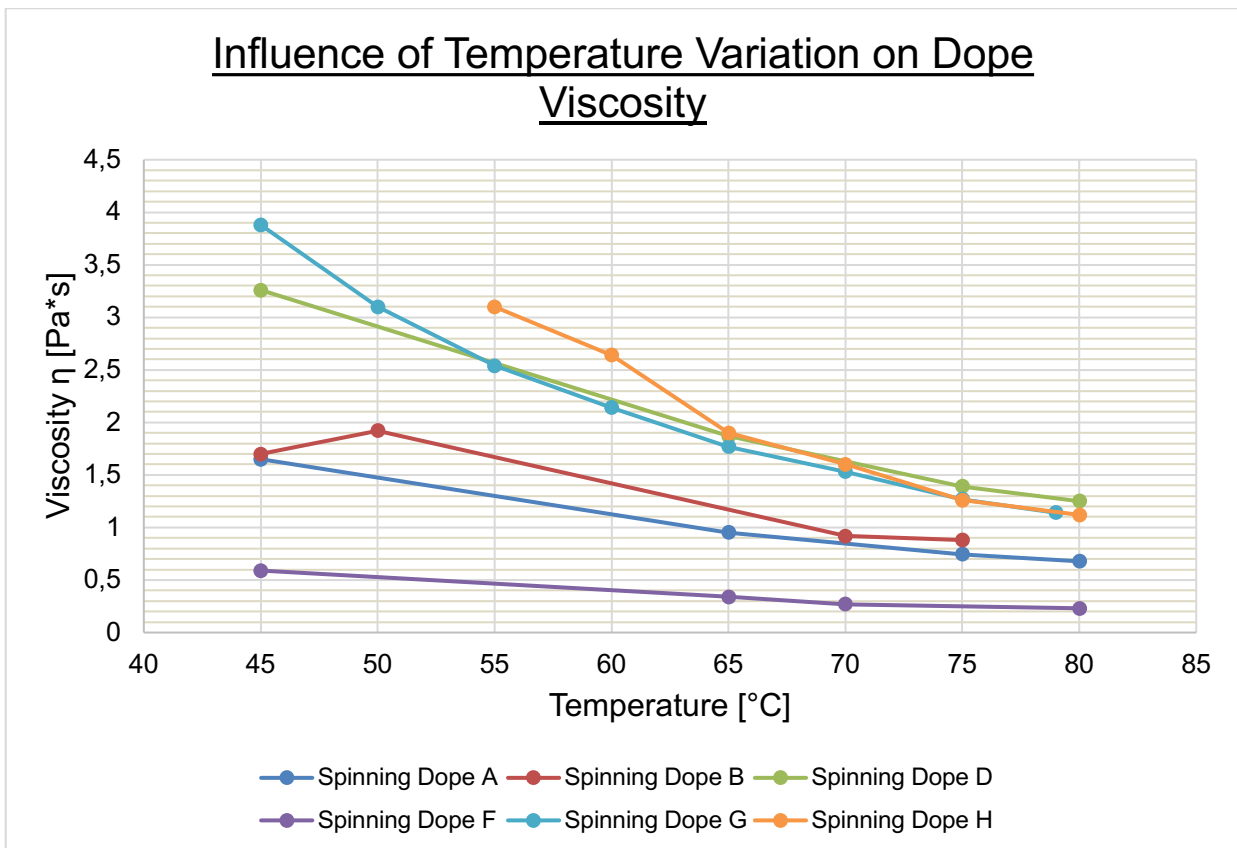


Figure 33: Influence of temperature variation on the dope viscosities for multiple spinning dopes used in this thesis

Influence of PES Concentration on Dope Viscosity

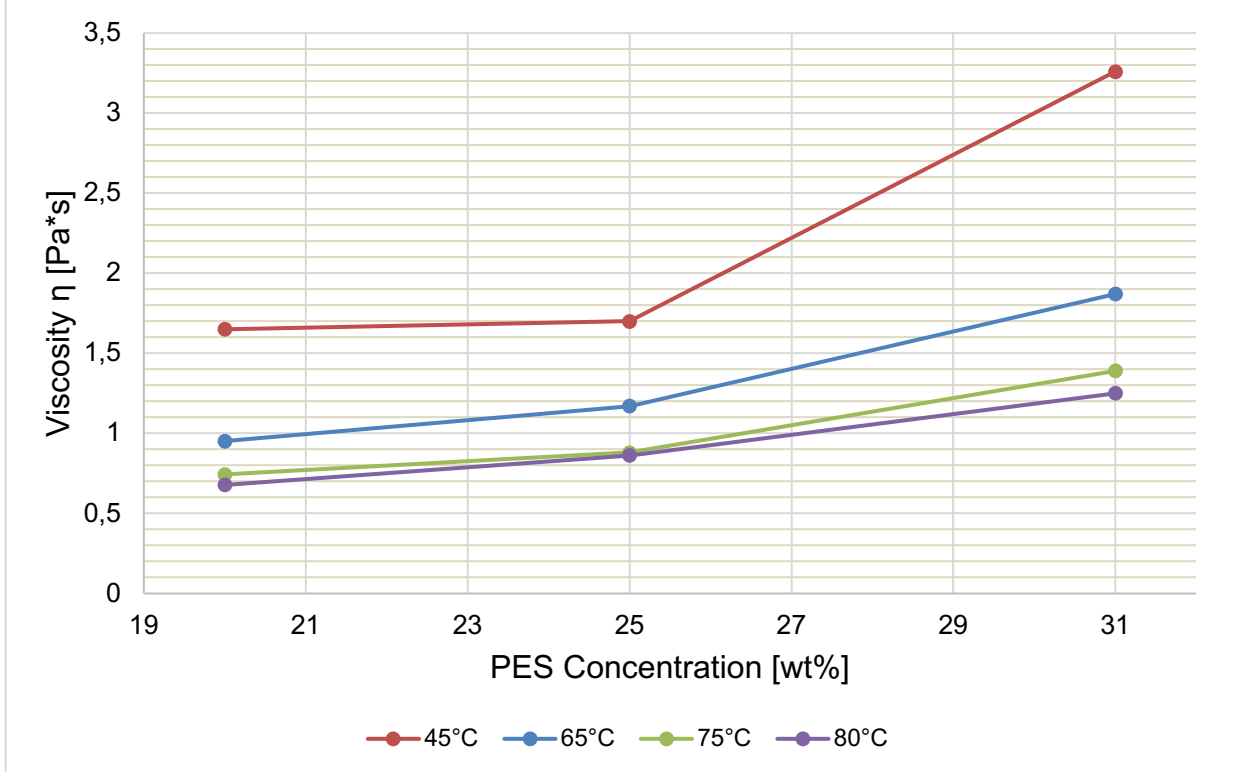


Figure 34: Influence of PES concentration on dope viscosity for spinning dopes A, B and D

4.2 SEM Analysis

It is possible to see very clearly that fibres with vastly different morphology and fibre structure are spun due to their differing spinning parameters, as evident in Figure 35. The four SEM pictures are only pictured here as an example. All SEM pictures can be found labelled in the Appendix section. Interpretation of the results, fibre dimensions and SEM pictures are detailed in the next chapter.

A comprehensive outlook is given on the influence of PES concentration, spinning temperature (temperature of the spinneret), air gap length, bore fluid composition on fibre morphology and fibre dimensions is discussed in the next chapter.

Table 9-Table 15 provides an overview of the fibre dimensions and porosity of the fibres spun in different experiments. This is merely a summary of the observed effects the examined parameter had on the dimensions and the porosity of the fibre in question. A detailed discussion and interpretation follow in the next chapter.

With increasing concentrations of PES in the dope solution, a general trend can be seen of increasing fibre dimensions, but a downward trend in porosity. This is in keeping with the observed phenomena described in literature [3], [18].

Table 9: Fibre dimensions and porosities of four identifiers at spinneret temperature 40 °C

	Identifier			
	A_40	B_ST40	C_40	D_40
Outer Diameter [µm]	395,1	492,8	449,0	574,8
Inner Diameter [µm]	286,5	376,4	333,1	407,4
Geometric Porosity [%]	71,6	67,3	62,1	59,7

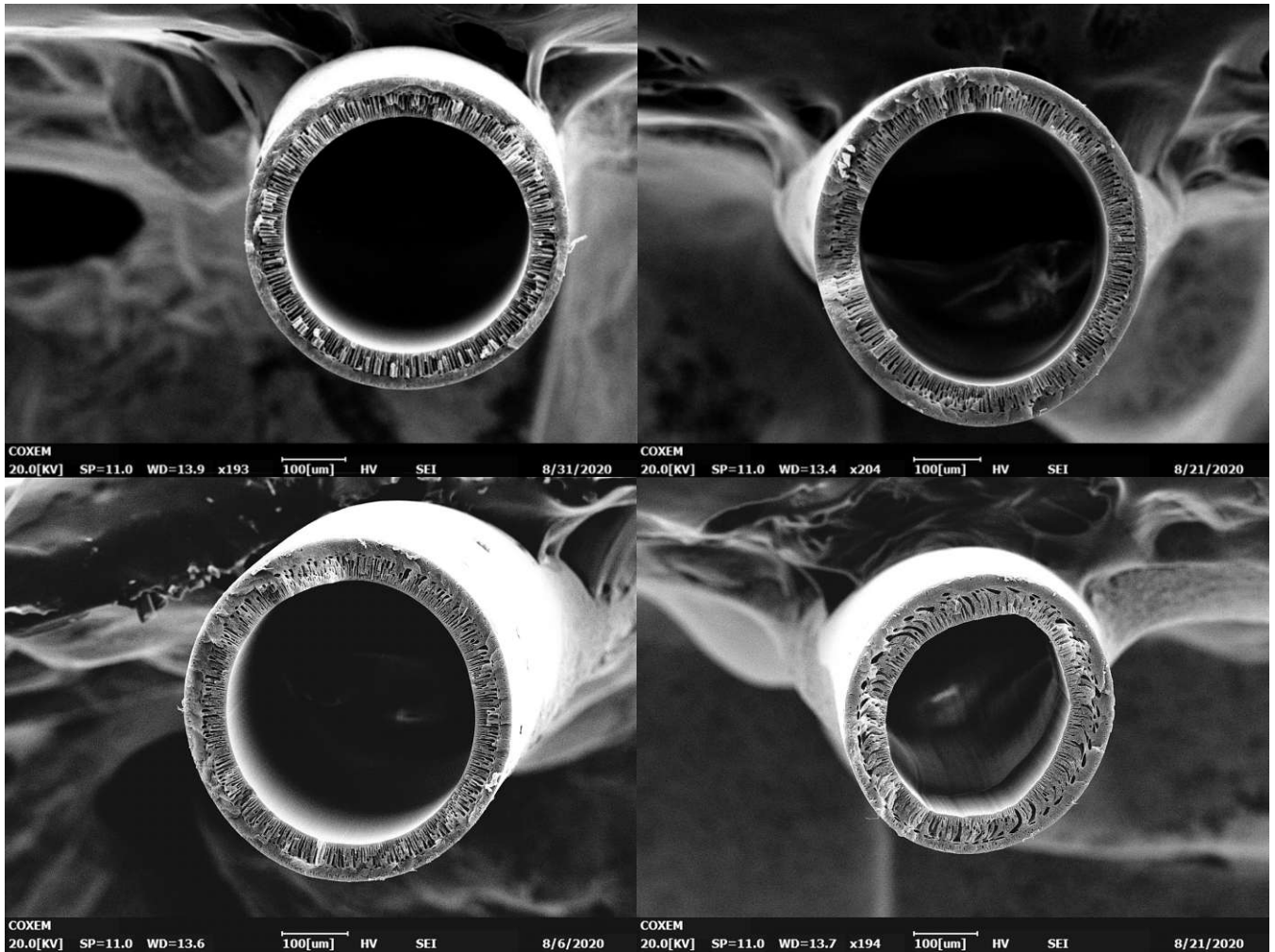


Figure 35: SEM photographs of hollow fibres spun with increasing spinneret temperature : from the top left: B_ST30, B_ST40, and from bottom left: B_ST50 and B_ST65

Based on the results obtained, the spinneret temperature leads to an initial increase followed by a decrease in fibre dimensions and a simultaneous increase in porosity (see Table 10). This may be due to increased diffusion rates of solvent exchange and phase separation.

Table 10: Fibre dimensions and porosities of hollow fibres spun from spinning dope B at four different spinneret temperatures

	Identifier			
	B_ST30	B_ST40	B_ST50	B_ST65
Outer Diameter [µm]	460,7	503,6	492,8	426,8
Inner Diameter [µm]	341,1	381,3	376,4	290,9
Geometric Porosity [%]	57,8	58,9	67,3	72,4

It was observed that while there was an insignificant change in the fibre diameters, the air gap length had a significant impact on the observed porosity of the spun fibres, as the porosity seemed to decrease with increasing air gap length. This can be explained by the increased time the fibre spends in the air with a certain amount

of humidity, resulting in slower demixing. Once the fibre meets the coagulation bath, the fibre is quickly precipitated (Table 11).

Table 11: Fibre dimensions and porosities of hollow fibres spun from spinning dope B at three different air gaps

	Identifier		
	B_AG65	B_AG130	B_AG260
Outer Diameter [μm]	602,7	606,0	568,1
Inner Diameter [μm]	418,1	450,4	417,5
Geometric Porosity [%]	71,2	67,1	64,6

Table 12: Fibre dimensions and porosities of hollow fibres spun from spinning dope B spun with two different bore fluid compositions

	Identifier	
	B_ONMP	B_50NMP
Outer Diameter [μm]	602,7	574,3
Inner Diameter [μm]	418,1	407,6
Geometric Porosity [%]	71,2	67,2

From Table 12 the amount of NMP in the bore fluid decreased fibre dimensions and the porosities of the spun fibres. From the SEM pictures, it is evident that the NMP changed the inner morphology of the fibres. Adding solvent into the bore fluid delays demixing and slows down the rate of demixing, which might be the reason for the decrease in porosity.

Table 13: Fibre dimensions and porosities of hollow fibres spun from spinning dopes A, E and F with different additives

	Identifier		
	A_40	E_40	F_40
Outer Diameter [μm]	420,8	478,7	522,8
Inner Diameter [μm]	319,0	298,1	369,1
Geometric Porosity [%]	81,6	64,4	69,2

The effect of additives added to the dope solution was also examined. From Table 13, it is evident that the fibre dimensions increase significantly from A_40 (no additive) to F_40 (PEG and water as additives). It is surprising to note that the addition of PEG reduces porosity, when PEG is a commonly known pore-forming additive. The addition of both PEG and water (F_40) however depicts higher porosity than E_40, which may be attributed to instantaneous L-L demixing and formation of many macrovoids.

Table 14: Fibre dimensions and porosities of hollow fibres spun from spinning dope D at different bore fluid flowrates

	Identifier		
	D_BFF0,12	D_BFF0,24	D_BFF0,36
Outer Diameter [μm]	664,4	669,0	650,5
Inner Diameter [μm]	566,4	579,8	593,1
Geometric Porosity [%]	68,6	57,1	45,8

The effect of the ratio of the flow rates of dope and bore fluid on fibre dimensions and morphology was also examined (Table 14). Increasing diameters and decreasing porosities are observed with increasing flow rates. This could be due to the increasing take-up speeds necessary to keep the fibre at a suitable elongation and to keep up with the increasing flow rates.

Table 15: Fibre dimensions of hollow fibres spun from spinning dope D at different coagulation bath temperatures

	Identifier	
	DCT_25_2	DCT_45_2
Outer Diameter [μm]	446,4	482,1
Inner Diameter [μm]	292,9	296,4

Coagulation bath temperature and its effect on fibres was also examined (Table 15). There is a slight increase of the fibre dimension to be seen. Porosity tests were unfortunately not conducted. Despite of the somewhat conflicting results of this experiment with the theory of phase separation, this experiment still serves as a validation that fibres can be effectively spun with varying coagulation bath temperatures with the newly built modular NIPS plant.

4.3 Ultrafiltration Tests

The purpose of this thesis is to explore the operation of the modular NIPS process plant. Due to the new operation of the newly built plant, it was imperative to be able to spin fibres that were hollow, circular in shape and display an optimum pore structure. Thus, a large part of this thesis and its focus deals with SEM pictures and porosity testing, rather than the UF and permselectivity performance. However, the operation of the modular NIPS process plant proved to be successful enough to spin fibres that showed favourable UF properties. It is imperative that high-performance membranes need to have a good rejection rate as well as an optimum permeance.

UF tests were done for fibres spun with different flow rates, as shown in Table 16. D_BFF0,12 and D_BFF0,24 have the same dope to bore fluid flow rate ratio. The increased rejection rates suggest that the pore sizes decrease as extrusion rates increase due to stretching of the fibre.

Table 16: Permeance and solute rejection rate for spinning dope D at two different flow rates

	Identifier	
	D_BFF0,12	D_BFF0,24
Permeance [L/h/bar/m^2]	20,7	286,1
Solute Rejection Rate [%]	78,1	89,0

An absorption spectrum can be graphed from the data recorded from the UV/VIS machine. Multiple samples are taken and thus an average taken. The BSA rejection rate can be determined using the peaks depicted from the UV/VIS graph (Figure 36).

Absorption Spectrum for BSA Rejection

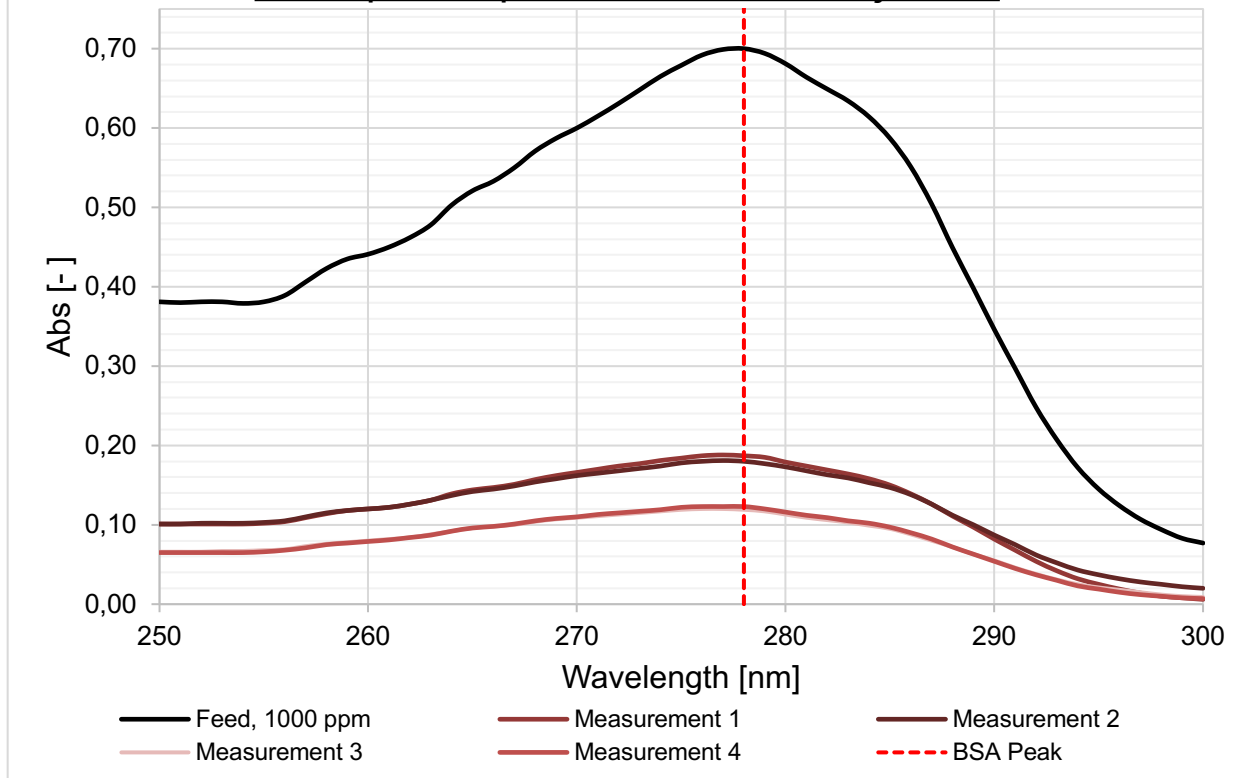


Figure 36: BSA absorption spectrum for spinning dope D_BFF0,12

Another UF experiment was carried out for fibres spun with two different coagulation bath temperatures (Table 17). Solute rejection rate increases as the coagulation bath temperature increases. This is probably credited to an increase in not only the faster diffusion and demixing rate but also due to a higher humidity in the air gap.

Table 17: Permeance and solute rejection rate of hollow fibres spun for spinning dope D at two different coagulation baths

	Identifier	
	DCT_25_1	DCT_45_1
Permeance [L/h/bar/m²]	286,1	2,8
Solute Rejection [%]	89,0	95,7

4.4 Gas Separation Tests

Modules were tested with the in-house (E166-02-2) gas separation unit. While the permeances measured were higher than the values that literature reports, it is important to note that the modular NIPS process plant had just been under operation and thus it is to expect that further optimization, experience in operating the unit is necessary.

As can be seen from Table 18, there is a decidedly large decrease of permeance for both nitrogen and carbon dioxide at 40 and 65 °C, despite of the fact that with increasing spinning temperature, the porosity increases. The selectivity also

decreases with temperature, although not very significantly. This could be due to the difference in pore structure and the reduction in the inner and outer diameters with the increase in temperature.

Table 18: Permeance and selectivity for fibres spun with spinning dope C at spinneret temperatures 40 and 65 °C

Gas Permeation Performance						
delta P [bar]	C_40			C_65		
	N ₂ [GPU]	CO ₂ [GPU]	CO ₂ /N ₂	N ₂ [GPU]	CO ₂ [GPU]	CO ₂ /N ₂
0,6	657,8	666,0	1,01	3284,7	2863,6	0,87
0,9	1390,1	1313,0	0,94	2615,7	2182,8	0,83
1,3	151,1	146,9	0,97	2307,7	1934,6	0,84

Table 19 shows no real difference between the permeances of nitrogen and carbon dioxide and the selectivities for fibres A_40 and B_40. The spike measured at 3 bars for nitrogen with B_40 is most likely a result of an imperfect part of the fibre rupturing. It is also evident that in this case the permeance increases tendentially as the pressure difference is increased. This is, however, not always the case (Table 18). This behaviour is most likely due to the way the fibres were prepared during the module building process. Additionally, carbon dioxide gas was tested before nitrogen gas, which also explains the increase in permeance for nitrogen. This was performed before it was known that carbon dioxide affects the fibre morphology, changing the permeance of gases tested after carbon dioxide, as reported in literature [57].

Table 19: Permeance and selectivity for fibres spun with spinning dopes A and B at spinneret temperature 40 °C

Gas Permeation Performance						
delta P [bar]	A_40			B_40		
	N ₂ [GPU]	CO ₂ [GPU]	CO ₂ /N ₂	N ₂ [GPU]	CO ₂ [GPU]	CO ₂ /N ₂
1,1	151,1	146,9	0,97	152,5	138,5	0,91
2,0	153,8	151,4	0,98	177,8	150,8	0,85
3,0	157,1	156,2	0,99	515,8	175,7	0,84

The PDMS coating clearly influenced the permeance and the selectivity of the fibres. The PDMS coating decreased the permeances and selectivities of both gases. As most literature describes, a 'healing' step is usually necessary with PES fibres, as it is relatively hard to spin without imperfections and pinholes. The membrane skin layer is covered with a PDMS layer which prevents any fluid to escape through holes/imperfections. The PDMS coating also acts as a selective layer for carbon dioxide.

Table 20: Influence of coating on the permselectivity performance; fibres spun with spinning dope C_40

Gas Permeation Performance							
C_40				C_PDMS40			
delta P [bar]	N ₂ [GPU]	CO ₂ [GPU]	CO ₂ /N ₂	delta P [bar]	N ₂ [GPU]	CO ₂ [GPU]	CO ₂ /N ₂
0,64	658,0	666,0	1,01	0,76	299,8	445,0	1,48
0,77	945,0	1095,8	1,16	0,83	364,0	1097,0	3,01
0,88	1390,0	1313,0	0,94	1,04	776,2	1569,7	2,02

4.5 Mechanical Stability

Based on the results (Figure 37), it was observed that the fibres can undergo more stress and are able to elongate much further before breaking with higher PES concentrations. This is assumed to be due to the increased number of macromolecules within the dope solution and the lower porosity with increased PES concentrations.

The increase in PES concentration leads to fibres with significantly lower porosities, which in turn lead to fibres that show a higher elongation at break and that can withstand higher stresses. This is due to the decreased pore density as the PES concentration rises.

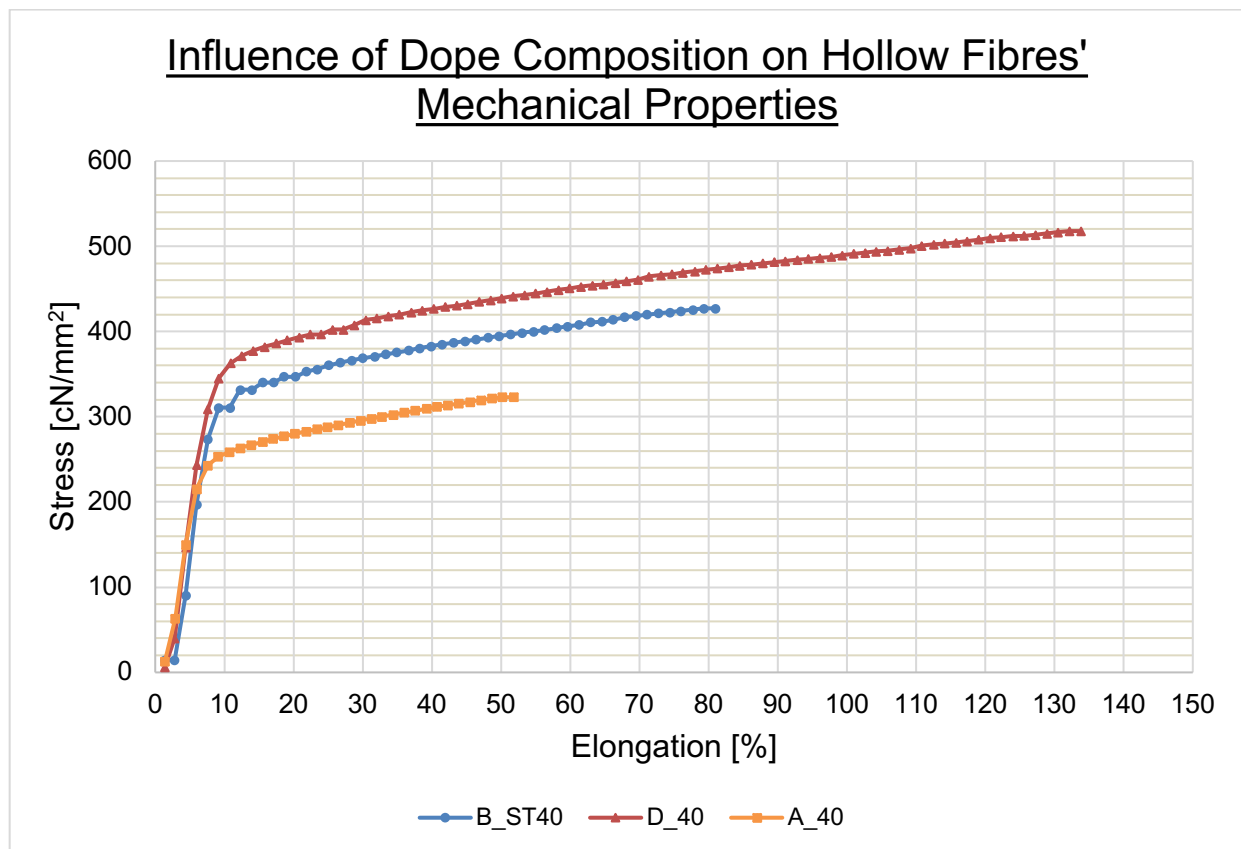


Figure 37: Influence of PES concentration on the stress strain test of spun hollow fibres from three different spinning dopes

5 Discussion and Interpretation

5.1 Viscosity of Dope Solution

As found in literature [3], [18], [25], the viscosity of the dope solution directly influences the porous structure within the fibres, as it leads to a much more pronounced portion of macropores. Viscosity is also related to the PES concentration in the dope solution and the temperature of the solution. Thus, it is imperative to measure and establish the exact connection between the three.

It is an established fact that the viscosity of any liquid decreases with temperature. This is because as the temperature increases, the macromolecules gain kinetic energy and become more mobile. This in turn leads to the reduction of the attractive binding energy between the molecules and a reduction in viscosity [58]. This is exactly the trend that can be seen in Figure 33, as for all spinning dopes, an increase in temperature results to a decrease in dope viscosity. Dope B's viscosity shows an unexpected trend from 45 to 50 °C, and this is most likely due to a type/written error while noting down the viscosity.

The more interesting effect on the dope viscosity is the PES concentration in the dope solution. In Figure 34, it is evident again that dope viscosity decreases with temperature. It is also evident that the viscosity for spinning dopes A, B and D increases with increasing PES concentration (at the same temperature). This is a confirmation of what is reported in literature [3], [18], [25]. With increasing PES concentration and a larger number of PES macromolecules, a higher chain entanglement is expected. This has a multitude of consequences on fibre morphology, porosity, and pore structure, which is further examined in later units.

5.2 SEM Analysis

In this thesis, PES concentration in the dope solution, spinneret and dope temperature, solvent in bore fluid, additives and flow rates of dope and bore fluid and the airgap at which the fibres are spun all depict fibres with varying morphologies, dimensions, and porous structures. Each parameter influences the fibre dimensions, morphology, and pore structure differently. As seen in many literature papers and reports, it is not always easy to separate the effects of one parameter from another.

SEM characterization is a widely utilized method for characterizing fibres as this is one of the simpler ways to examine pore structure, surface porosity and fibre dimensions accurately. In this thesis, the SEM characterization plays a large role in analyzing the spun fibres, as that is the first characterization method used. Additionally, the SEM characterization proved initially to be the guiding method in the decision of which parameters to change, experiments to perform and fibres to spin.

Hollow fibres are asymmetric membranes and have been thoroughly discussed in previous chapters. All SEM pictures display the characteristic outer/inner skin layer supported by a spongy interconnected pore structure. Almost all fibres (regardless of the parameters they were spun with) display finger-like pores growing from either the outer, inner or both surfaces. Macrovoids, as reported from literature, are a sign of instantaneous L-L demixing and of a nonsolvent-solvent system that show high affinity to each other. Additionally, a dense outer skin layer is also another sign for the same

phenomenon. Thus, it can be assumed that the dope composition for all dopes were close enough to the metastable/unstable state in the ternary phase diagram that little nonsolvent was needed to precipitate.

One limitation that must be discussed is that the SEM utilised in this thesis did not have a high enough resolution capable of magnifying to the lumen and shell surfaces. SEM pictures of certain experiments (air gap variation and the NMP concentration in the bore fluid) were examined under a SEM with a much higher resolution and magnification (FEI Quanta250 FEG, Thermo Fischer, Waltham, USA). Thus, examining the lumen and shell surfaces was possible. Since the majority of the SEM pictures taken do not illustrate surface porosity and the lumen and shell surfaces, no assumptions and statements can be made about these characteristics.

Secondly, the cross-section of the fibre is utilised to calculate the fibre dimensions, porosity, gas permeance and PWP. It is assumed that the fibre consists of the same pore structure, density, and distribution over its entire length. In addition, it is also assumed that the fibre has the same dimensions over its effective length. This can be misleading, as there might be imperfections, holes, spots of incomplete/improper phase inversion, damage, collapsing and other undesirable and inevitable consequences over the fibres' lengths. Such imperfections are not considered in this thesis, as this would make a qualitative and quantitative evaluation of the fibres almost impossible.

5.2.1 Influence of Airgap on Fibres' Morphology

Air gap length is a crucial parameter to the morphology and dimensions of hollow fibres. Figure 39 shows the influence of the air gap length on the spun fibres. While the outer and inner diameters of the spun fibres show a small decrease, the porosity is profoundly affected by the increase in air gap length. The fibre dimensions are seen to slightly decrease as the airgap increases. The fibre experiences higher elongational stresses as the airgap increases. The PES aggregates rearrange themselves into a state of higher stability, leading to a decrease in pore size and a more uniform distribution of pores on the membrane surface on the bore fluid side, as can be seen in Figure 38.

From the SEM pictures (Table 29) taken, all fibres from all different air gaps show finger-like macrovoids forming from both inner and outer surfaces. Additionally, many of the pores display a closed-off pore structure. The characteristic spongy structure can be observed from fibres spun with all three different airgap lengths. The more peculiar phenomenon is the large macrovoids that appear to be distorted towards the middle of the cross-section. This can be probably attributed to the higher flow rates that were set for this experiment. The dope flow rate 115,1 $\mu\text{l}/\text{min}$ and bore fluid flow rate 92,7 $\mu\text{l}/\text{min}$ were higher than the usual flow rates (59/59 $\mu\text{l}/\text{min}$). Due to the larger amount and higher speeds of dope and bore fluid flowing through the spinneret, the diffusion and nucleation process taking place in the coagulation bath are distorted.

Additionally, the take-up speed also plays a role in the formation of dimensions and pore structure, as this affects the shear stress and tensile force that the fibre experiences during phase separation. While it has been assumed that the phase separation that occurs in most of the experiments was to some extent instantaneous demixing, the fibre does not fully precipitate during the time the fibre first coagulates

and reaches the take-up winder drum. Therefore, it can be safely assumed that this distortion can affect the pore structure.

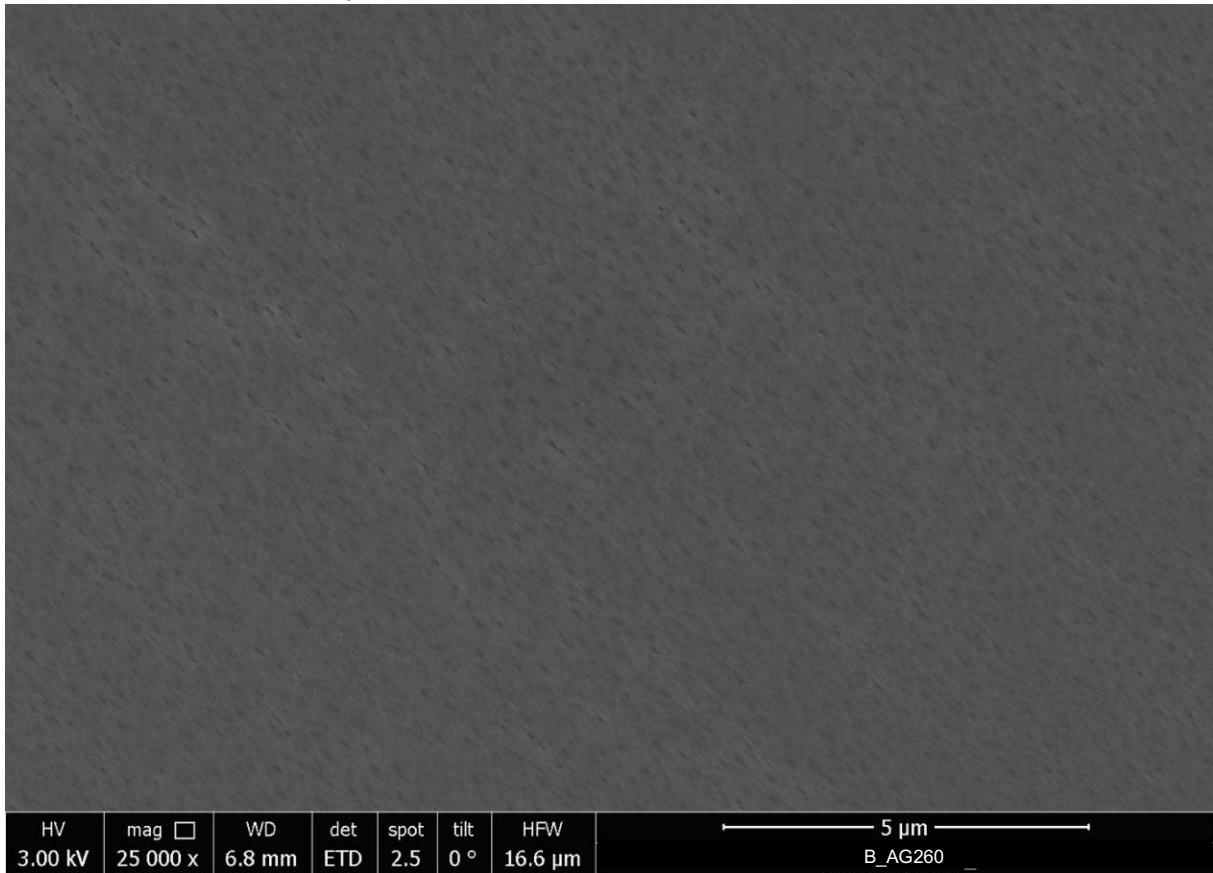


Figure 38: Lumen surface of B_AG260 fibres; sample prepared by cutting the hollow fibre in half and placing the fibre flat on to the sample holder to be able to observe the inner surface

In the fibres spun at 65 mm, a faint separation in the cross section is evident in the middle of the cross-section (Table 29). This is also attributed to the demixing process. There is a higher density of finger-like pores from the inner surface as compared to from the outer surface. This is due to the instantaneous precipitation and nucleation that starts as soon as the dope comes into contact with the bore fluid outside of the spinneret. The fibre spends time in the airgap before the fibre is submerged in the coagulation bath. During this time, nucleation of the polymer-rich phase is occurring as the NMP, and water diffuse from the inside of the fibre. A skin is formed, which slows down and ultimately prevents solvent exchange and traps the solvent and nonsolvent within the pore structure, leading to more macropores interspersed with a spongy texture towards the inner surface.

Influence of Air Gap *B_AG65, B_AG130 and B_AG260*

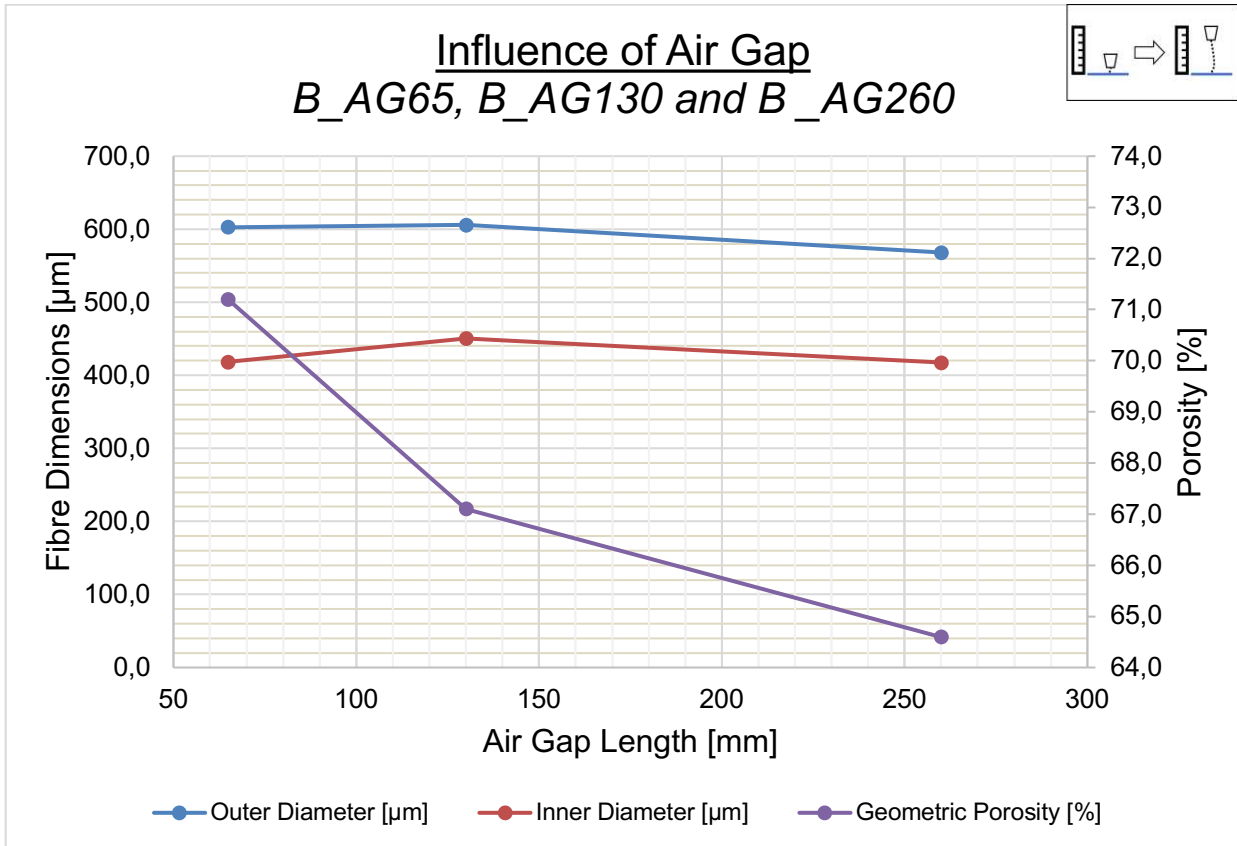


Figure 39: Influence of air gap length on fibre dimensions and porosity for hollow fibres spun from spinning dope B; three different air gap lengths set: 65, 130 and 260 mm

Finally, the fibre is submerged in the coagulation bath and another phase separation front is to be found on the outer surface. Another reason for the lower density of macropores on the outer part of the cross-section is that the pores that did start to form in the air gap (due to humidity) were pulled together due to the shear rate and the gravitational force the fibres experience as they travel through the air gap. The moment the fibres reach the water in the coagulation bath, the structure is somewhat frozen. Solvent exchange continues to take place, however, at a reduced pace as the growth of the skin and nucleation occur.

The effect of the air gap on porosity is an interesting trend as well. Porosity decreases as the air gap length increases. This effect is observed in literature with conflicting conclusions [29], [35], [38], [42]. In this thesis, it was observed that the air gap tended to stretch the fibres leading to the pores to collapse together. The fibres experience more gravitational pull as the air gap length increases, leading to lower porosity. This result is in tune with literature [38], where a higher air gap leads to smaller pore sizes due to tighter molecular packing.

5.2.2 Influence of Polymer Concentration in Dope Solution on Fibres' Morphology

PES concentration affects the kinetics of membrane formation and solvent exchange, thus greatly influencing the fibre morphology and porosity. Thicker skins and fibre dimensions are the result of higher PES concentrations due to the significant delay in the coagulation of the inner structure. The binodal curve shifts towards the P-S axis in the ternary phase diagram, thus affecting phase inversion thermodynamics.

Any phenomenon that affects the kinetics and thermodynamics of the phase inversion process, ultimately affects fibre morphology, dimensions, and porosity. This is exactly the observation that was witnessed in this experiment.

PES concentration and its effect on the dope viscosity has already been examined. Dope viscosity, PES concentration and fibre porosity are undeniably interconnected, with each parameter affecting the other. Thus, dope viscosity must be considered when discussing the effects of PES concentration on fibre dimensions, morphology and fibre porosity.

Figure 41 shows a general increasing trend of fibre dimensions (with a dip in fibre dimensions at 27 wt% PES) and a decreasing trend in porosity with increasing PES concentrations. With higher concentrations of PES, it would seem that fewer macrovoids and a lower porosity are exhibited by the fibres. With increasing concentrations, the fibres spun are larger but show a slight decrease with fibres spun from dope C.

However, there are additional, and arguably more significant effects that need to be accounted for; namely the take-up speed (elongational stresses caused due to the speed at which the fibre is winded) and the die swell phenomenon. One effect is the tension the fibre experiences when it is being taken up by the winder drum. While it would have been ideal to keep the take-up speeds constant, this was tricky to hold constant. During the experiments, it was always attempted to set the take-up speed so that the fibre is under an appropriate amount of elongational stress visually. The take-up speed should correspond with the free fall velocity at which the fibre emerges from the spinneret and due to the varying viscosities of the dope solutions, this velocity also varied. A balance had to be struck between the mechanical stability of the fibre and the elongational stress the still precipitating fibre could withstand. Thus, this led to varying take-up speeds (Table 8).

Even though the take-up speeds are not very different from each other- A_40 being taken up at 73 mm/s, B_ST40 at 58 mm/s, C_40 at 66 mm/s and D_40 at 105 mm/s- this difference in the amount of elongational stress plays a large role in the thickness of the fibre. This effect would describe the sudden decrease in the fibre dimension for identifier C_40. B_ST40 was taken up at a lower speed as compared to A_40 and C_40 and thus is thicker than either identifier. The increase in fibre dimensions to D_40, however, cannot be explained with this phenomenon, since D_40 was taken up at a much faster speed than the other identifiers but is thicker than the rest. Since the dope extrusion rate (DER, and hence the dope extrusion velocity) was kept constant over all four identifiers (59 μ l/min), each identifier experienced a different stretch ratio [59]. This parameter can be defined as the ratio between the take-up speed and the dope extrusion velocity, as shown in Equation 46:

$$\text{Stretch Ratio} = \frac{\text{Take - up Speed}}{\text{Dope Extrusion Velocity}}$$

Equation 46: Definition of the stretch ratio

Table 21 depicts the relationship between the take-up speed and the DERs of all four identifiers in detail. The stretch ratio varying from around 9 to nearly 17 shows clearly the fact that the take-up speed was a prominent factor in the fibre thickness. The ID/OD ratios of all four hollow fibres were higher than the spinneret ID/OD ratio,

leading to the conclusion that the fibres shrunk and have smaller cross-sections than the spinneret cross-section. However, it is expected that the rather high stretch ratios in this work would lead to fibres of even lower thickness. This unforeseen phenomenon, however, can be attributed to the die swell effect.

Table 21: Physical dimensions of the resulting hollow fibres; concentration variation

	A_40	B_ST40	C_40	D_40
Stretch Ratio [-]	11,6	9,2	10,5	16,7
ID/OD [-]	0,73	0,76	0,74	0,71
Take-up Speed [mm/s]	73	58	66	105
DER [$\mu\text{l}/\text{min}$]			59	
Dope Extrusion Velocity [mm/s]			6,3	
Spinneret Ratio (ID/OD) [-]			0,67	

Die swell is an aspect that is common to extrusion of viscoelastic polymers/polymer mixtures. When an extrudate is forced through an orifice into the air, the extrudate is compressed as it enters the die. As it leaves the die, the extrudate partially swells back to the previous cross-sectional area and volume, as is shown in Figure 40. The previous shape in the larger cross section is a part of the extrudate's 'fading memory', which it tries to return to after leaving the orifice. Die swell is an effect that is dependent on the material, extrusion conditions and the temperature [60]–[62]. As stated above, it is evident that the fibres spun are thicker than expected and this can be attributed to the die swell effect. As the PES concentration in the dope solution increases, the viscosity rises and thus the die swell effect is expected to have a greater impact on the fibre. It has been mentioned in literature [59], [61] that winding a fibre onto a spool reduces the die swell and this exact occurrence was observed in this work as well.

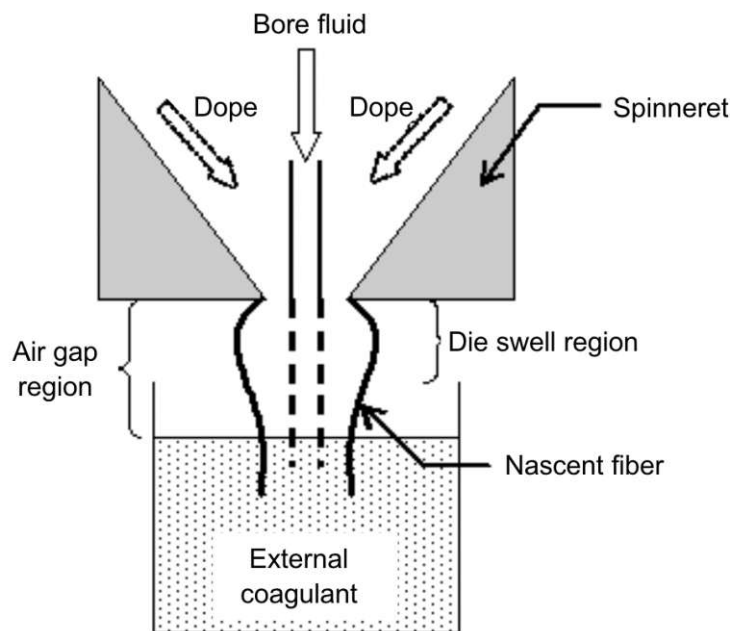


Figure 40: Die swell illustration in hollow fibre formation [59]

Additionally, the fibre length between the time that they are extruded and get taken onto the first spool (bottom white spool in Figure 29) experience elongational

stress due to gravity as well and this counteracts the die swell effect as well. However, literature [59], [61] states that this effect is close to negligible and almost eliminated once the fibre is taken up on to the winder drum. Thus, the effects of the take-up speed and die swell make comparison of each fibre from each dope concentration difficult.

From Table 27, it is evident that all fibres show long finger-like pores spreading from the inner surface. However, the length and density of these fibres decrease with increasing PES concentration. The ratio of the finger-like pores length to the wall thickness seems to also decrease, as the fibre becomes larger as well. The number of finger-like pores from the outer surface becomes larger with increasing PES concentration. The same distortion with the pores in the mid-region of the cross-section is seen for fibres spun with dope A and B. This can be attributed to the lower viscosity of dopes A and B in comparison to dope D. The decrease in finger-like pores and creation of spongy structures with higher concentrations is an observation also recorded in literature.

Higher viscosities and higher PES concentrations mean that a higher concentration of macromolecules is present in the dope solution. This means that less nonsolvent is necessary to induce phase inversion. A greater chain entanglement and molecular packing was observed with higher PES concentrations, therefore leading to fibres with lower porosity. Additionally, the Flory-Huggins model also proves that a higher macromolecular concentration leads to lower free volume and less intrinsic porosity.

The increase in fibre dimensions is also due in part to a greater stability of the fibre at higher PES concentrations. It was comparatively easier to spin and handle fibres with higher PES concentrations, as this phenomenon leads to fibres that are mechanically stable.

The viscosity plays a large role in the solvent-nonsolvent exchange. With a higher number of PES molecules, viscosity increases, and phase inversion leads to skin formation at a much faster rate. This leads to the solvent and nonsolvent trapped within the inner structure of the fibre and a reduced solvent-nonsolvent exchange, leading to the decrease in the length and density of the finger-like pores and a spongier structure due to delayed demixing. Viscosity also influences the influence of gravity within the airgap. This is because the stronger internal friction between the randomly coiled molecules may be able to outweigh the gravitational forces, preventing further elongation. This leads to a lower porosity with higher PES concentrations.

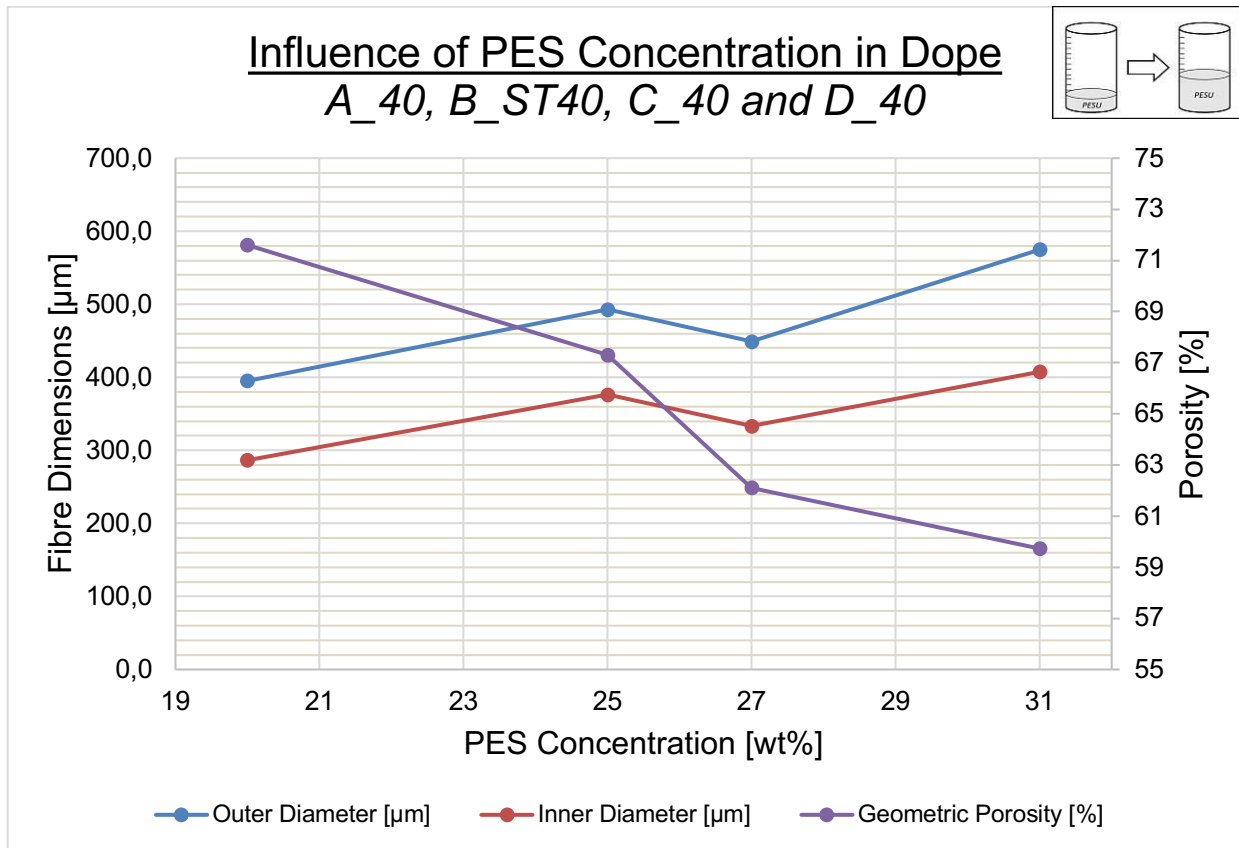


Figure 41: Influence of the PES concentration in the dope solution on fibre dimensions and porosity

The viscosity of the dope solution also probably played a hand in the spongier structure seen on the outer region of the cross-section as well. Due to the higher concentration of PES in the dope solution and at the interface, the outer skin layer was created faster due to the humidity in the air gap. This led to the reduction of the solvent exchange of NMP and the steam in the air gap, thus leading to delayed demixing and a spongier pore structure. As the fibre then was submerged into the coagulation bath, the pore structure was arrested, and the nucleation and formation of the smaller finger-like pores was to be noticed.

5.2.3 Influence of Temperature of Dope Solution on Fibres' Morphology

The effect of the temperature of the dope solution and spinneret was also examined. The spinneret temperature is a deciding factor in the spinning of the fibres. It is also the last region where temperature control of the NIPS process is possible. Thus, in these experiments the dope temperature was identical to the spinneret temperature. The bore fluid temperature was kept at a constant 50 °C for all experiments. A constant temperature of 50 °C was held at the pump reservoir and the bore fluid was heated further in the spinneret.

It is evident that an increase in the temperature reduces the viscosity of the dope solution and thus leads to thinner fibres with higher porosities, when the temperature is increased (Figure 42). Thinner fibres were also a result of elongational and gravitational stresses as a result of take-up speeds. Similar concepts as described in 5.2.2 apply here as well. The rise in temperature leads to increased rate of diffusion and solvent exchange. This speeds the process of demixing, leading to greater macropore formation. Table 28 shows the trend of fibre morphology, pore structure

and macrovoid formation with increasing temperature. At 65 °C, the same distortion of the pores in the mid-region of the cross-section can be observed. This affect is probably due to the lower viscosity and thus the greater elongational stress experienced by the fibre as it is spun. A large density of finger-like pores growing from the inner region of the cross-section can be found in all fibres at all temperatures. From the SEM pictures, it is evident that fibres spun at 65 °C with dope B do not exhibit a desired shape and morphology, despite illustrating higher porosities. The lumen surface is also not perfectly round, as the fibres go from exhibiting perfectly circular lumens to a lumen with jagged edges.

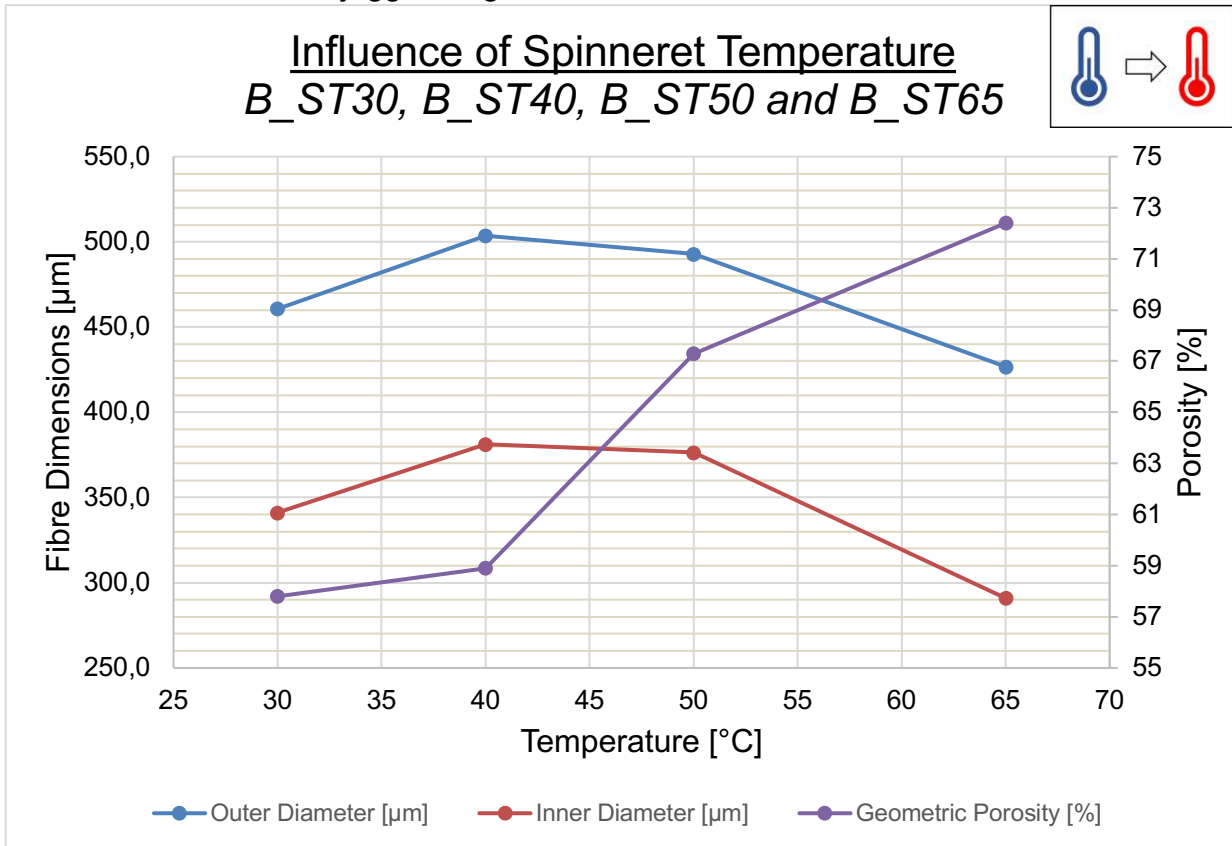


Figure 42: Influence of the spinneret temperature on fibre dimensions and porosity

The outer region of the cross-section also exhibits a spongier texture at higher temperatures. While this is in contradiction with what was described in 5.2.2, it is also important to note that at a higher temperature the dope solution is less viscous and experiences more elongational and gravitational forces, thus resulting in some of the pores collapsing into each other. This elongational force that the fibre experiences is also responsible in reducing the fibre dimensions with higher temperatures.

The effects of the take-up speed and die swell must be acknowledged in this experiment as well. Table 22 illustrates the effects of the take-up speed and die swell on the fibre dimensions. B_ST30, B_ST40 and B_ST50 all have similar take-up speeds, ID/OD ratios and stretch ratios, while B_ST65 being significantly different from the other three identifiers. B_ST65 was the only hollow fibre where the ID/OD ratio was almost equal to the spinneret ID/OD ratio, suggesting that at 65 °C, the opposing effects of the take-up speed and the die swell were in equilibrium, leading to fibre dimensions very similar to the spinneret dimensions. Literature [60] states that the die swell effect reduces with increasing temperature with a fixed flow rate, an observation

to which this thesis is in line with. Similarities between the ID/OD ratio and the spinneret ID/OD ratio can also be explained by the higher take-up speed B_ST65 was collected with in comparison to the other three hollow fibres.

Table 22: Physical dimensions of the resulting hollow fibres; spinneret temperature variation

	B_ST30	B_ST40	B_ST50	B_ST65
Stretch Ratio [-]	8,9	9,2	10	11,9
ID/OD [-]	0,74	0,76	0,76	0,68
Take-up Speed [mm/s]	56	58	63	75
DER [$\mu\text{l}/\text{min}$]			59	
Dope Extrusion Velocity [mm/s]			6,3	
Spinneret Ratio (ID/OD) [-]			0,67	

5.2.4 Influence of Solvent in Bore Fluid on Fibres' Morphology

The bore fluid composition plays a large role in the determination of the morphology and pore structure of the inner surface. As the bore fluid is mainly responsible for the phase inversion in the lumen, this is the highlight of this experiment. It is hard to compare and see a trend when only two different points are taken and measured. However, the trend shown in Figure 44 has also been recorded in literature. Thus, this aspect is also worth discussing in this thesis.

Table 30 displays the SEM pictures of the fibres spun in this experiment. Both SEM pictures do not show an ideal geometry. It is probable that the cut of the fibre taken for B_ONMP was not ideal, or that the choice of the fibre was unlucky, as an imperfect portion of the fibre length was chosen inadvertently. However, fibres spun from B_50NMP show a circular geometry for the outer diameter, but a wavy inner form. This suggests that the cut taken from this fibre was not the problem, and that this peculiar wavy inner form is due to the bore fluid composition. It has been recorded in literature [45] that the presence of a solvent (NMP in this case) reduces the demixing rate and slows down the phase inversion, resulting in this wavy inner form. Other quick experiments that were carried out with some concentration of NMP in the bore fluid led to the same conclusion.

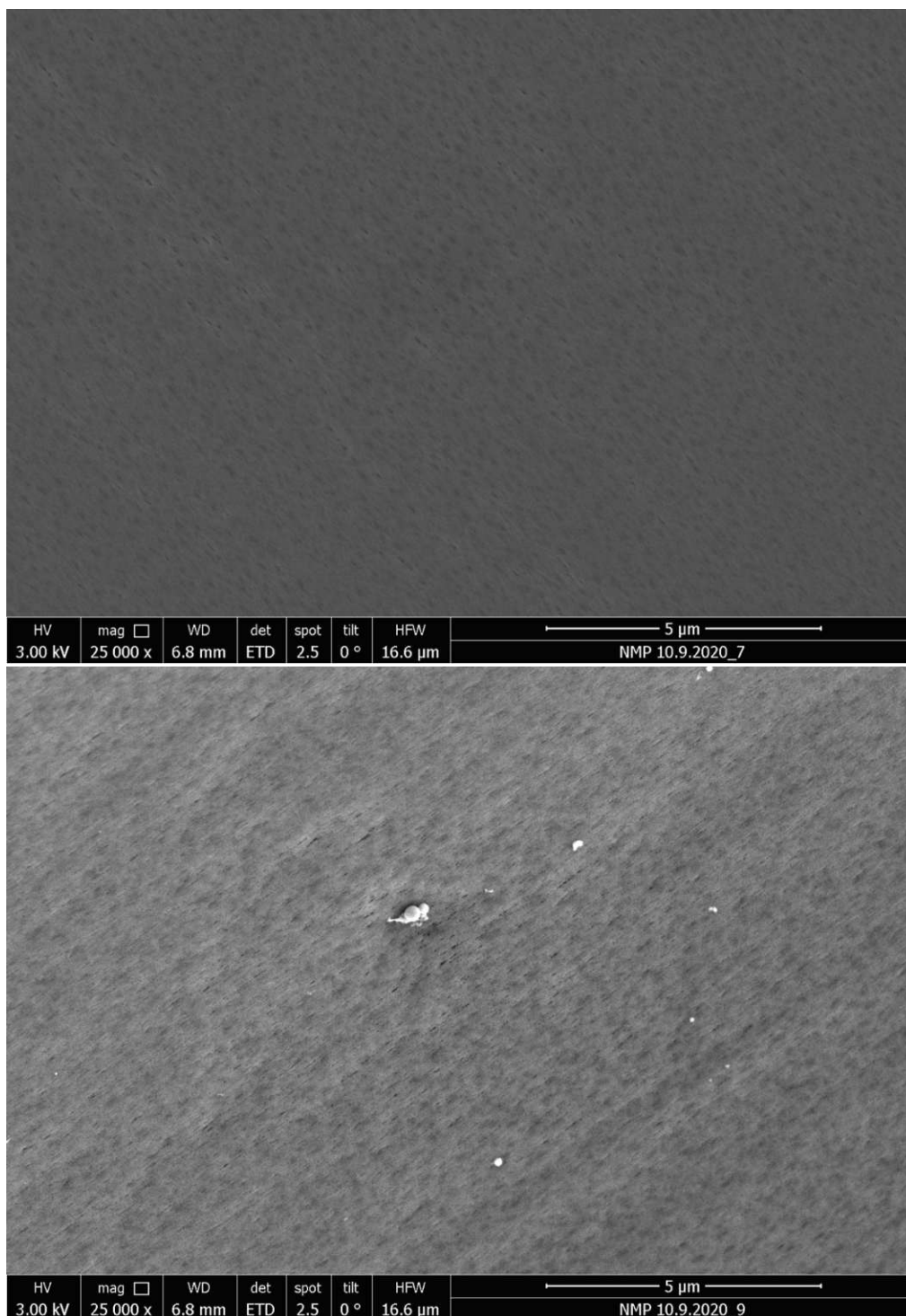


Figure 43: Lumen surfaces of B_0NMP (top) and B_50NMP (bottom)

Qualitatively speaking (Figure 43), there is an increase in the pore density of the fibres spun from B_0NMP and B_50NMP. However, the phenomenon of a dense inner layer with few pores was not observed here with B_0NMP, as is typically the case when using a strong nonsolvent as the bore fluid.

A general increase of solvent concentration has been observed to lead to increasing pore sizes and porosities due to the delayed L-L demixing as the effectiveness of the NMP/water mixture as a nonsolvent was decreased. Increasing NMP concentrations in the bore fluid moves the binodal further and further away from the P-S axis, resulting lower precipitation rates and delayed demixing. However, this

trend was not observed in this thesis. An increase of NMP concentration in the bore fluid from 0 to 50 wt% led to a slight decrease in porosity. In multiple studies, finger-like macrovoids were seen to be somewhat suppressed as the solvent concentrations in the bore fluid increased. However, there was no clear difference between the density and number of finger-like pores in B_0NMP and B_50NMP. Fibre dimensions change is almost negligible between the two fibres as well.

From the results, this aspect of the thesis needs to be further experimented, examined, and developed. It is entirely possible that there is a turning point between 0 and 50 wt% NMP, that was not measured here. Additionally, it is possible that after a certain threshold of NMP concentration in the bore fluid that the demixing process is drastically affected and leads to unfavourable and somewhat unrealistic results, as what has probably occurred in this case.

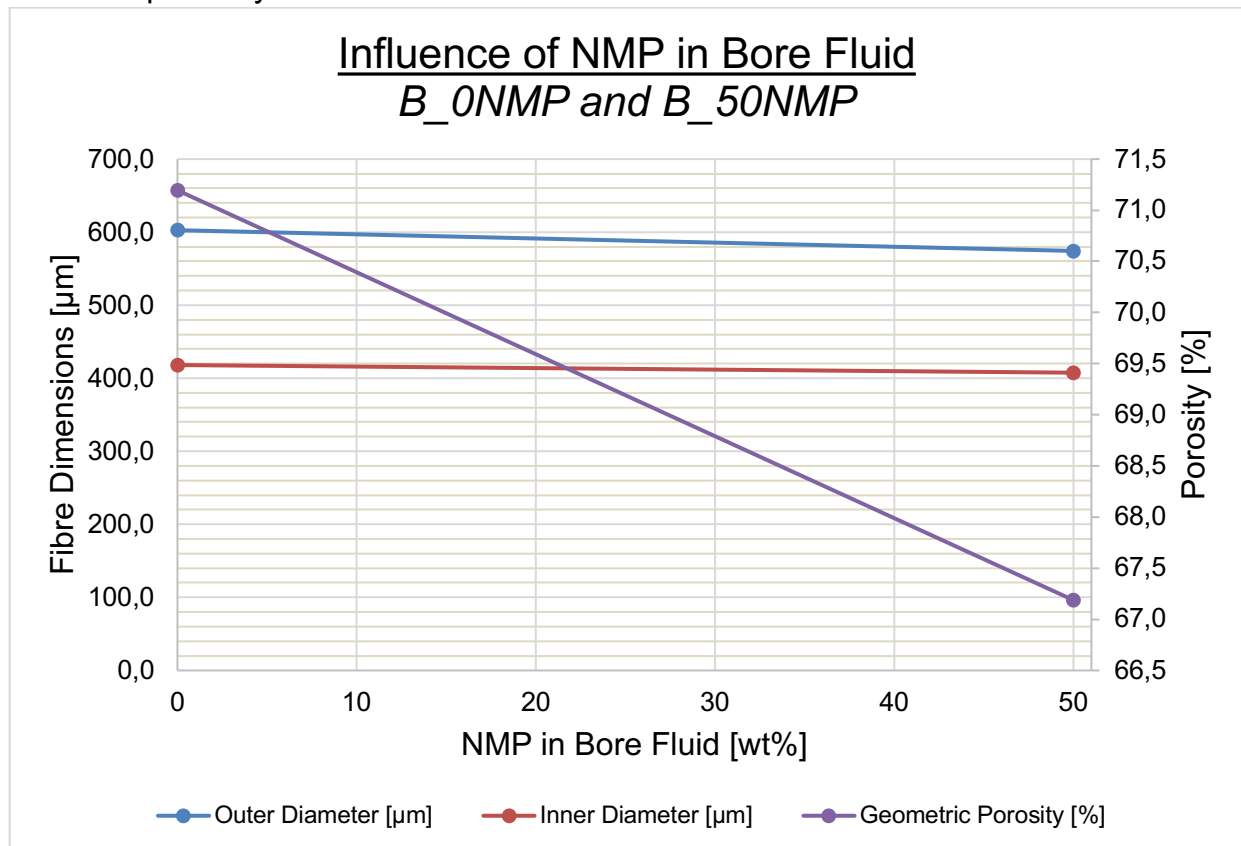


Figure 44: Influence of the amount of NMP in the bore fluid on fibre dimensions and porosity

5.2.5 Influence of Additives on Fibres' Morphology

A small experiment was also performed with different additives: PEG (dope E) and PEG and water (dope F). Three dopes have been chosen with the same PES concentration (20 wt%). PEG is a pore-forming additive that changes the kinetics and thermodynamics of membrane formation. Additives like PEG are retained within the fibre structure and thus alters the hydrophilicity/hydrophobicity behaviour of the membrane. Typically, additives like PEG can induce thermodynamic instability and promote instantaneous demixing, resulting in high fibre porosity.

With all additives, a cross-section complete with finger-like macrovoids was observed (Table 34). Fibres A_40 show smaller finger-like macrovoids as compared to fibres spun with dopes E and F. This can be attributed to the pore-forming additives of

PEG. The viscosity of dope F is also lower than A, therefore macrovoid formation is promoted. This phenomenon is unsurprising to observe.

Figure 45 and Figure 46 show that the addition of PEG and PEG/water increases outer diameters of the fibres. The fibres increase in fibre dimension as well. This is due to the increased concentration of macromolecules in the dope solution. This would also suggest that the dope solutions E and F are more viscous than A. Unfortunately, the viscosity of dope E could not be measured, and the viscosity of dope F seems to contradict the behaviour observed by fibres spun from dope F.

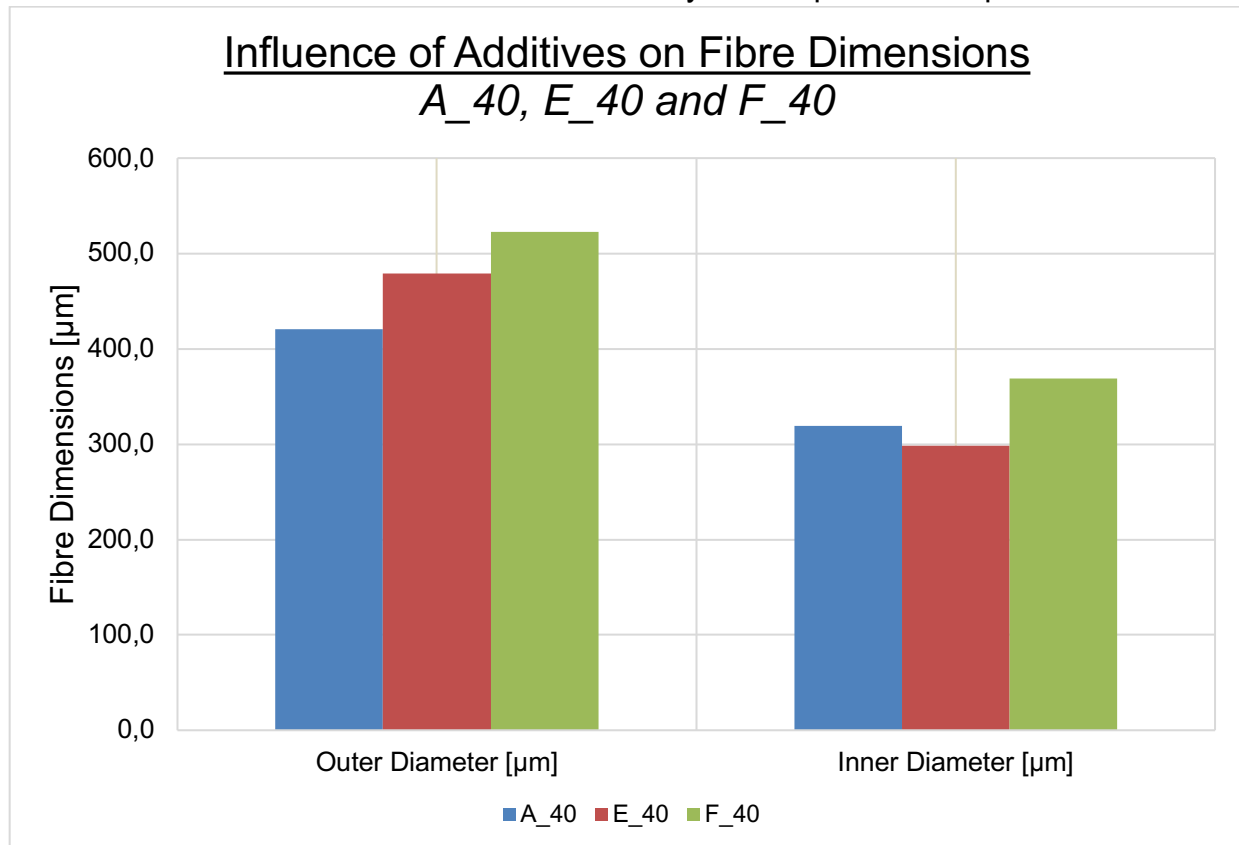


Figure 45: Influence of different additives on fibre dimensions

However, the porosity of the fibres correlates with the thickness and the behaviour exhibited by fibres with higher polymer concentration. Fibres spun from dope E exhibit a lower porosity as compared to fibres A_40. However, PEG is a pore-forming additive and its alterations on the demixing process leads to high fibre porosity. This was not the result that was observed. This phenomenon can be attributed to the assumptions taken for porosity experiments. Fibre samples spun from dopes E and F were tested for porosity after a long period of time after spinning. It can be also assumed that the fibres samples from dope E exhibited some imperfections and might have been damaged during the period that they were stored after spinning.

Fibres spun from dope F seem to correspond with the trends observed. Despite of the fact that this dope exhibited a lower viscosity than dope A, the fibres spun from this dope are thicker, as both PEG and water increase dope viscosity. However, the porosity measured is lower than fibres A_40. It is probably that there is a threshold of PEG concentration, above which the dope gets too viscous and the fibres steer away from the desired pore structure and thickness.

Only by visually examining the SEM pictures (Table 34), fibres E_40 and F_40 display larger macrovoids, and a less spongy structure as compared to fibres A_40. However, surface porosity (especially on the outer surface) is very visibly seen to increase with increasing additives (Figure 47). Fibres F_40 show a very porous outer skin-layer, due to the addition of PEG as well as the water in the dope, leading to a much faster binodal demixing. Despite of the increase in viscosity, it can be assumed that the dope is so close to the binodal, that it demixes extremely quickly, leading to a very porous outer layer and large macrovoid formation. Fibres E_40 depict some surface porosity, however not to the same degree as from dope F. This is in keeping with studies that report that the presence of PEG in a PES/NMP system leads to large macrovoids in the cross-section.

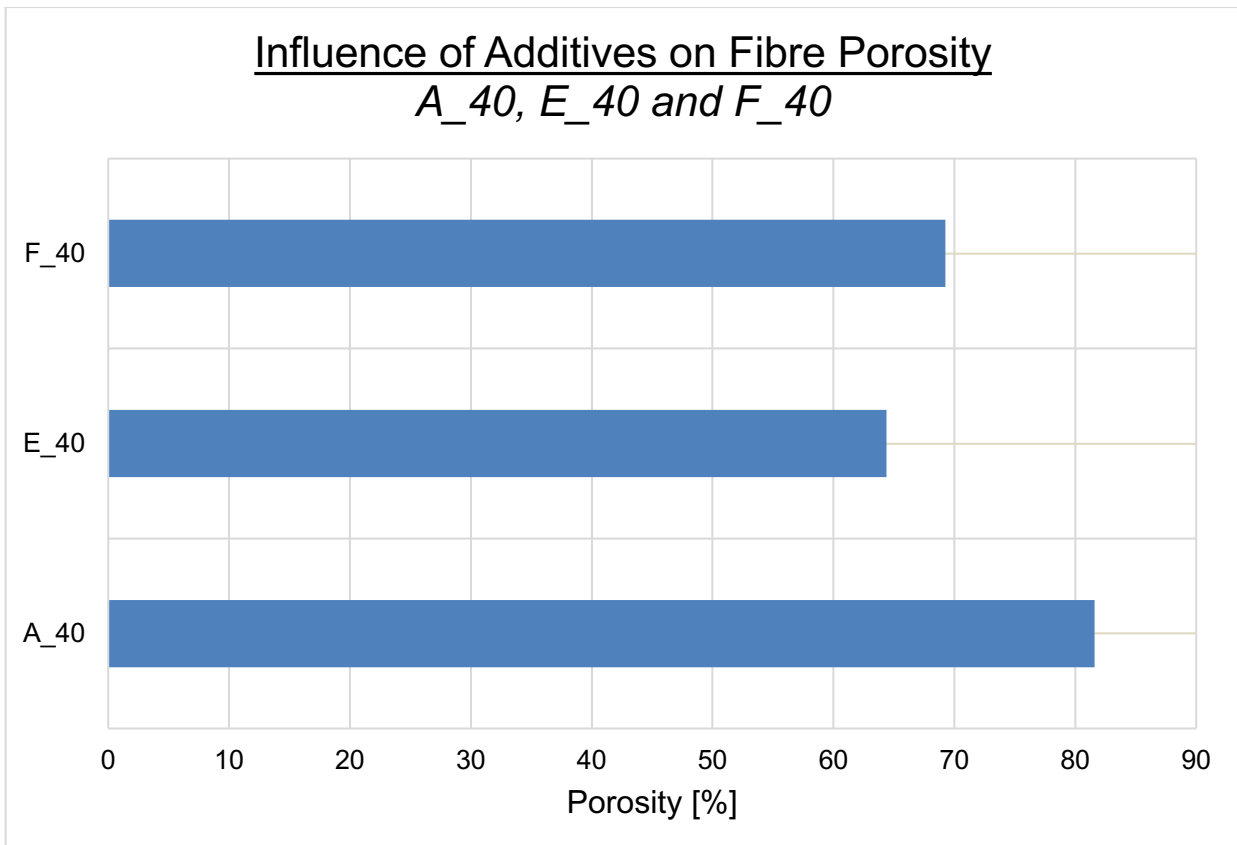


Figure 46: Influence of different additives on fibre porosity

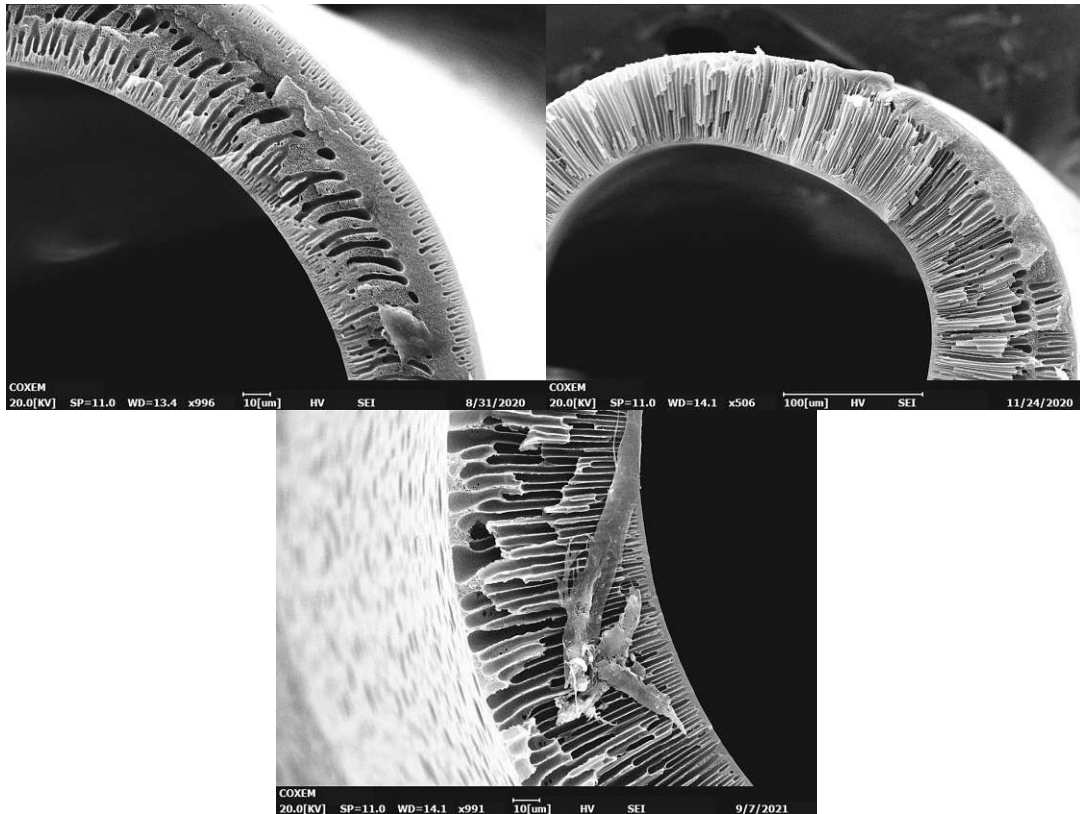


Figure 47: Surface porosity on the shell side; A_40 (left), E_40 (right) and F_40 (bottom)

Conclusively, this aspect of fibre spinning, and dope composition requires further research and development. A multitude of additives exist for different purposes. While certain additives like PI, PEG and PVP have been analysed for their effects on membrane production, more in-depth research is necessary to enable a more quantitative approach.

5.2.6 Influence of Flow Rates on Fibres' Morphology

Fibres were spun from spinning dope D (D_BFF0,12, D_BFF0,24 and D_BFF0,36) to analyse the effect of the dope extrusion rate (DER) and the bore fluid flow rate. Molecular orientation during fibre formation is controlled by elongational stress due to gravity and the shear and elongation stress within the spinneret and thus it was deemed important to evaluate the effect of DER on fibres' morphology and pore structure.

From Table 32 and Figure 48 it is evident that with increasing bore fluid flow rates, the wall thickness becomes thinner. While the outer diameter does not change significantly, the inner diameter becomes larger, thus resulting in fibres with thinner walls. This morphological behaviour is due to the increased speed at which the bore fluid was flown. This same conclusion was met by literature as well.

The SEM pictures show a trend in the pore structure of the fibres with increasing bore fluid flow rates. D_BFF0,12 shows very few macrovoids growing from the outer region of the cross-section, with increasing number of such macrovoids in D_BFF0,24 and moreso in D_BFF0,36. The type of demixing is crucial and the reason for such behaviour. D_BFF0,12 was spun at lower speeds and flow rates and spent a larger period in the air gap. This led to slower demixing and lower precipitation rates with the humidity when the fibres were submerged in the coagulation bath. This led to a

spongier structure with fewer macrovoids on the outer region. As the flow rates were increased, diffusion and precipitation rates were also increased, leading to a more instantaneous demixing and more macrovoids. In all fibres, the macrovoids from the outer region are not very large (in comparison to the macrovoids growing from the inner region). This can be a result of the faster flow rates that prevents the excessive growth of the nucleated polymer-lean phase, as the fibre travels much quicker through the air gap and coagulation bath. The finger-like macrovoids growing from the inner region of the cross-section are virtually the same for all fibres spun in this experiment.

The biggest factor here is again the take-up speed. Even though the phenomena caused by higher flow rates do contribute to the change in fibre dimensions, the take-up speed probably plays the largest role in the size of the fibre. D_BFF0,12 experienced the lowest take-up speed (172 mm/s), D_BFF0,24 with 317 mm/s and D_BFF0,36 the highest take-up speed (344 mm/s). Figure 48 depicts that D_BFF0,36 to have the smallest outer diameter as compared to the other two identifiers, which is line with D_BFF0,36 being taken up with the highest speed. D_BFF0,24 has a larger outer diameter than D_BFF0,12, which is not in line with the take-up speeds. However, this is where the higher flowrates come into play. D_BFF0,24 is extruded at twice the DER and bore fluid flowrates as D_BFF0,12 and this attributes to the increase in fibre size. With increasing DER, more dope is extruded out and thus experiences higher die swell and elongational stresses, leading to another balancing effect between the take-up speed, the die swell effect and the DER and bore fluid flowrate.

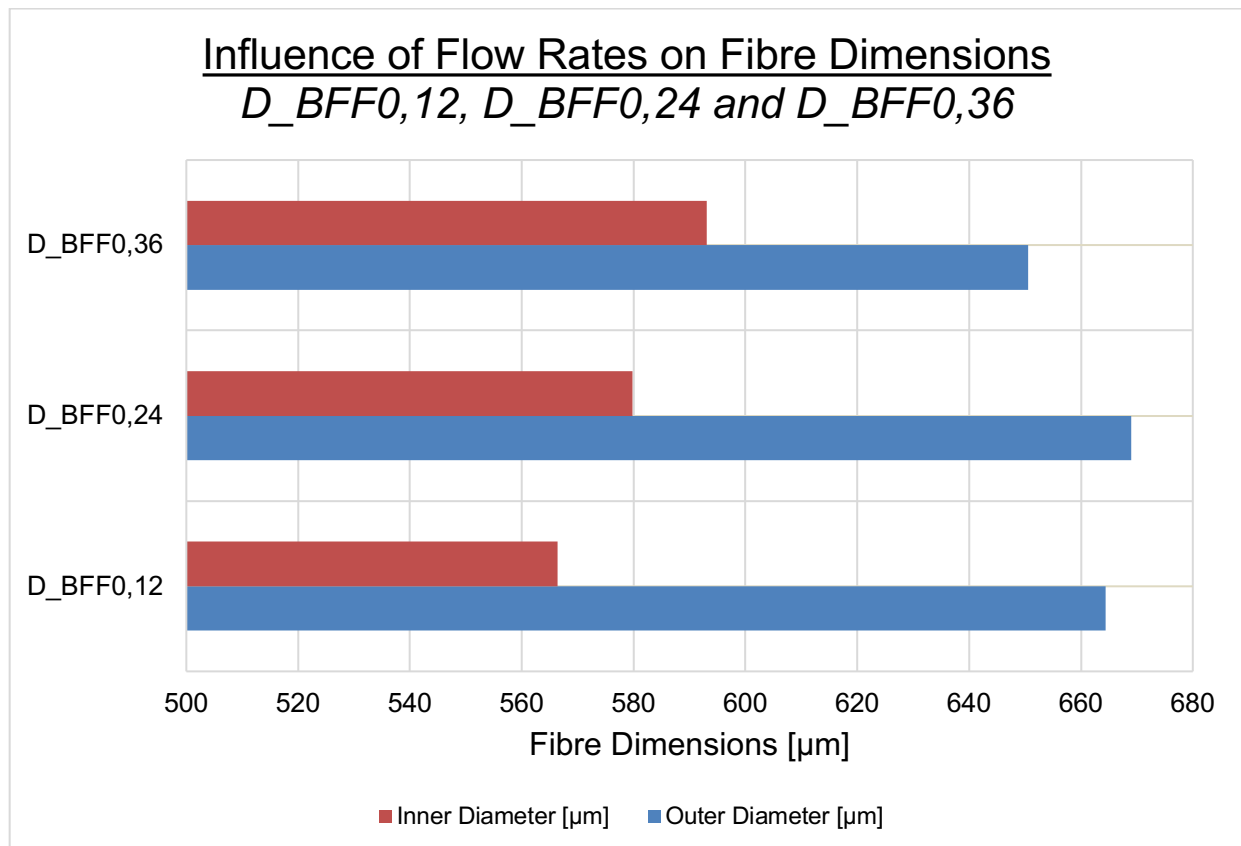


Figure 48: Influence of dope/bore fluid flow rates on fibre dimensions

D_BFF0,12 and D_BFF0,24 fibres were spun with the same dope/bore fluid flow rate ratio and this effect can be prominently observed as well. While the fibre

dimensions do not differ greatly, the porosity shows a significant decrease (Figure 49). With an increase of over 10%, the D_BFF0,24 fibres depicted a more porous membrane. This contradicts literature, where an insignificant effect was observed. It was stated that no difference in porosity was detectable. Pore sizes were observed to decrease due to the slow demixing at the inner surface, whereas pore density was seen to increase. Alas, in this thesis it was observed that porosity decreased, due to the less amount of time available for nucleation and growth of pores. With increasing flow rates, the shear stresses the fibre experiences is also higher. Additionally, take-up speeds must be higher to compensate for the faster flow rates. Thus, the pores are at a higher danger of collapsing and being pulled together therefore, decreasing porosity.

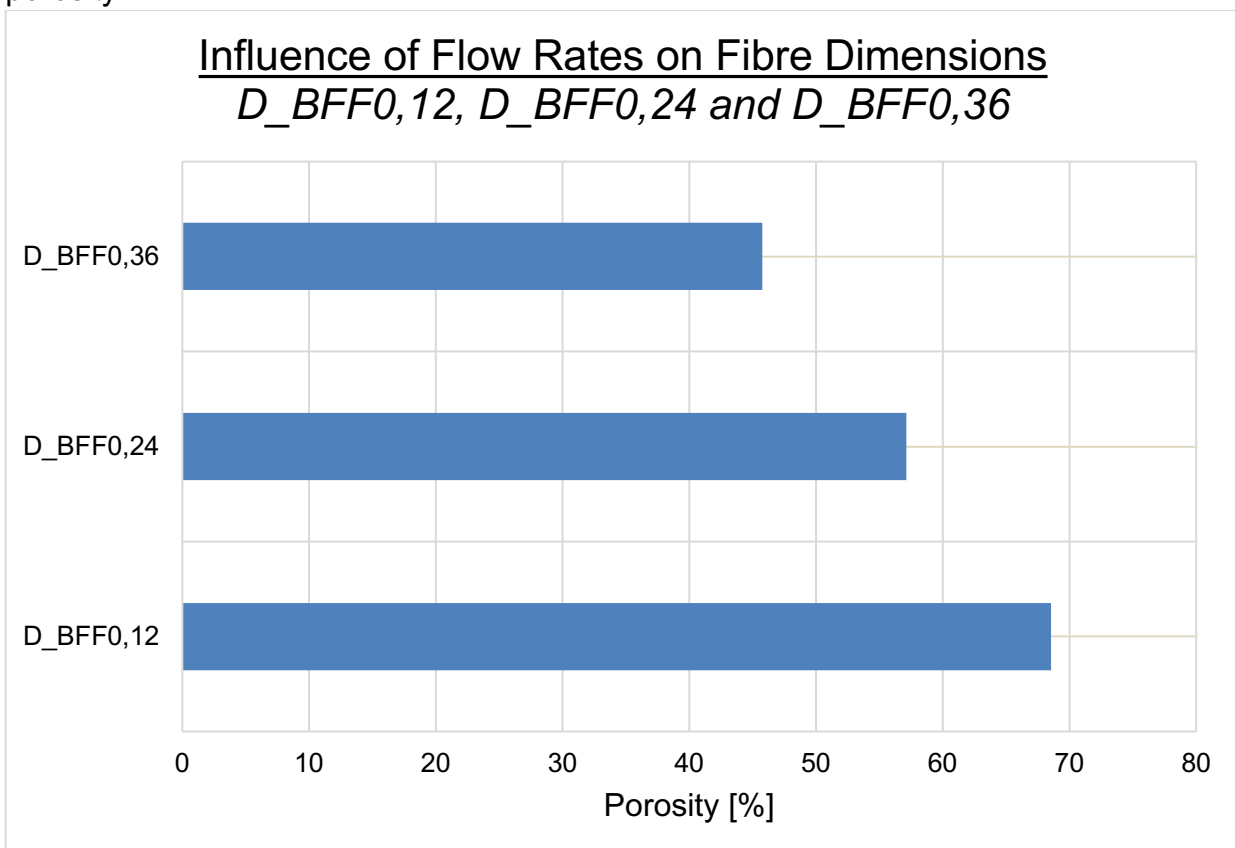


Figure 49: Influence of dope/bore fluid flow rates on fibre porosity

5.3 Ultrafiltration Tests

As mentioned before, the focus and guiding element of this thesis was the SEM characterization of the spun fibres. Fibre characterization using methods like ultrafiltration, gas separation and tensile tests were performed as evidence for the fact that the spun fibres were indeed capable of being utilised in fields and purposes in the biomedical, pharmaceutical, food and other industries, with further optimisation, development, and experience. Thus, it is imperative that further research and experimentation be dedicated to this form of characterisation in the future. Two different UF experiments were performed- coagulation bath temperature variation and flow rate variation.

5.3.1 Influence of Flow Rates on UF Performance

Literature suggests that there is link between the UF performance of spun fibres and the flow rate at which they were spun at. Here two different flow rate settings were examined. The ratio between the dope and bore fluid flow rate was identical, however D_BFF0,12 was spun at lower flow rates than D_BFF0,24. UF tests were conducted in the in-house apparatus. UF was performed on the lumen side and the permeate collected from the shell side. Figure 50 depicts the results of the UF test. With an increase in flow rates, both PWP and solute rejection increases. This is in contradiction with the concept that more permeable fibres typically illustrate comparatively lower solute rejections. It has also been discussed that D_BFF0,24 fibres are thinner and less porous. Therefore, the UF performance is quite interesting.

Studies [49], [50] report that PWP increased and BSA rejection decreased with increasing bore fluid flow rates due to an increase in pore density and a simultaneous decrease in wall thickness. This can partially be observed in this thesis as well. Thinner fibres with lower wall thicknesses were also observed with increase flow rates. However, the porosity of the fibres was seen to decrease instead of the increase that was observed in multiple papers. PWP and BSA rejection both increased in the UF results obtained.

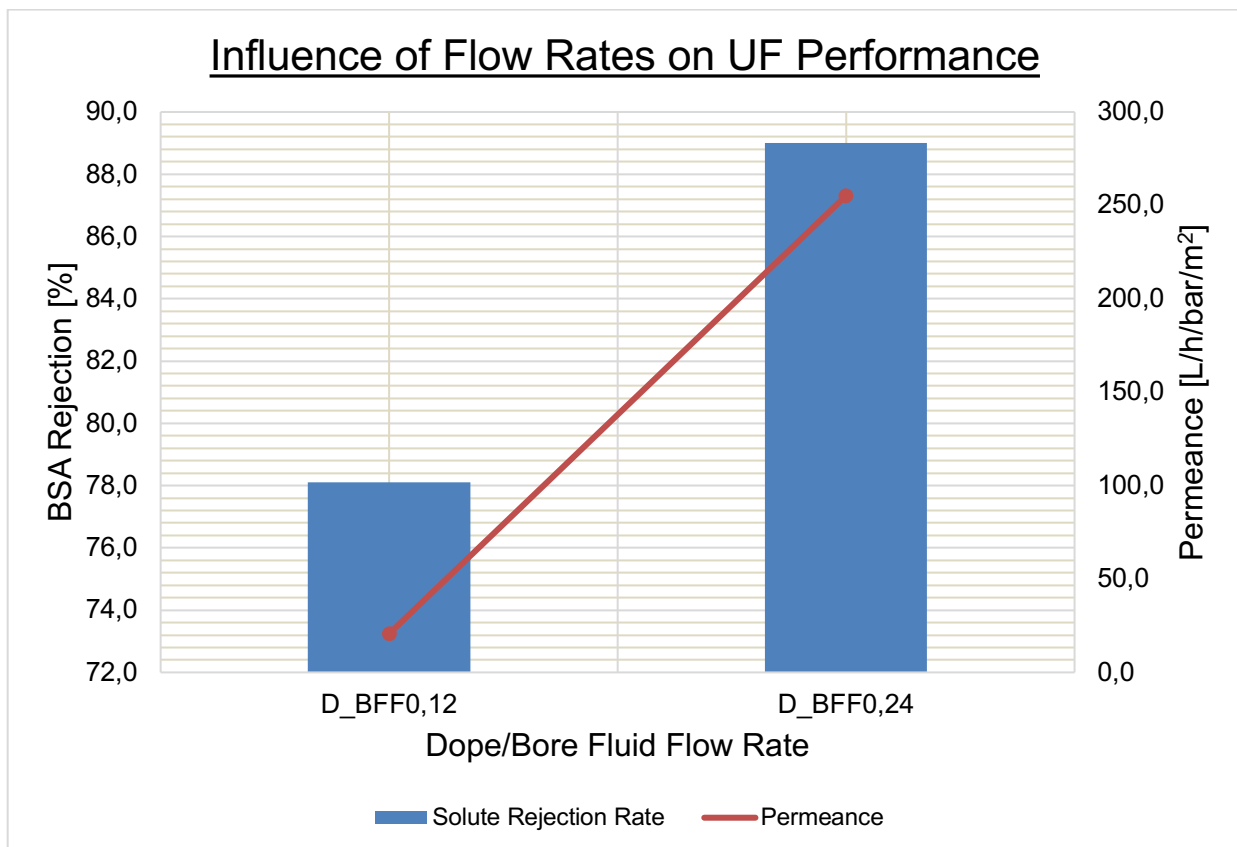


Figure 50: Influence of dope/bore fluid flow rate on UF performance

5.3.2 Influence of Coagulation Bath Temperature on UF Performance and Fibre Morphology

Coagulation bath temperature has a significant effect on fibre morphology and UF performance. While studies done contradict the effect of the coagulation bath, its effect on fibre performance and morphology is inevitable. Higher coagulation bath temperatures lead to higher humidity in the air gap, affecting the interdiffusion between

the solvent and nonsolvent at the fibre walls. In other words, this temperature highly affects the kinetics of fibre formation.

Since varying the coagulation bath temperature in this experiment was lengthy and were only performed in the earlier stages of this work, porosity tests were not conducted. Additionally, the fibre spinning process with the new NIPS plant was in its early stages and thus the focus lied upon achieving a desirable geometry with a finger-like pore structure that is suitable for ultrafiltration purposes. Therefore, this unit will cover both the effects of the coagulation bath temperature on the fibre morphology as well as fibre UF performance.

SEM pictures were taken from DCT_25_2 and DCT_45_2 fibres (Table 31). There is no profound difference in pore structure, macrovoid formation and fibre dimension of the fibres. The baffling phenomenon is the increase in fibre dimension with increasing coagulation bath temperatures. This contradicts the theory behind demixing, and the concepts that were used to describe the observed phenomena in this thesis. Literature reports thinner fibres, greater macrovoid formation and a fundamentally different fibre morphology with higher coagulation bath temperatures. As is usual in this field, studies reported conflicting observations regarding macrovoid formation. However, in this thesis, no correlation was found between coagulation bath temperature and fibre morphology. Yet again, the fibre dimensions are highly dependant on the take-up speed at which the fibres were taken up on the winder drum.

UF experiments were conducted using DCT_25_1 and DCT_45_1 (Figure 51). SEM pictures for DCT_45_1 could not be taken. This makes it considerably harder to compare and contrast fibres' UF performance with fibre morphology in mind. However, the UF performance is somewhat like what is recorded in literature. Solute rejection for BSA is recorded to be over 90% in many studies. Permeances recorded in this thesis have a very large variation and are either too low or too high to be consistent with literature.

Influence of Coagulation Bath Temperature on UF Performance

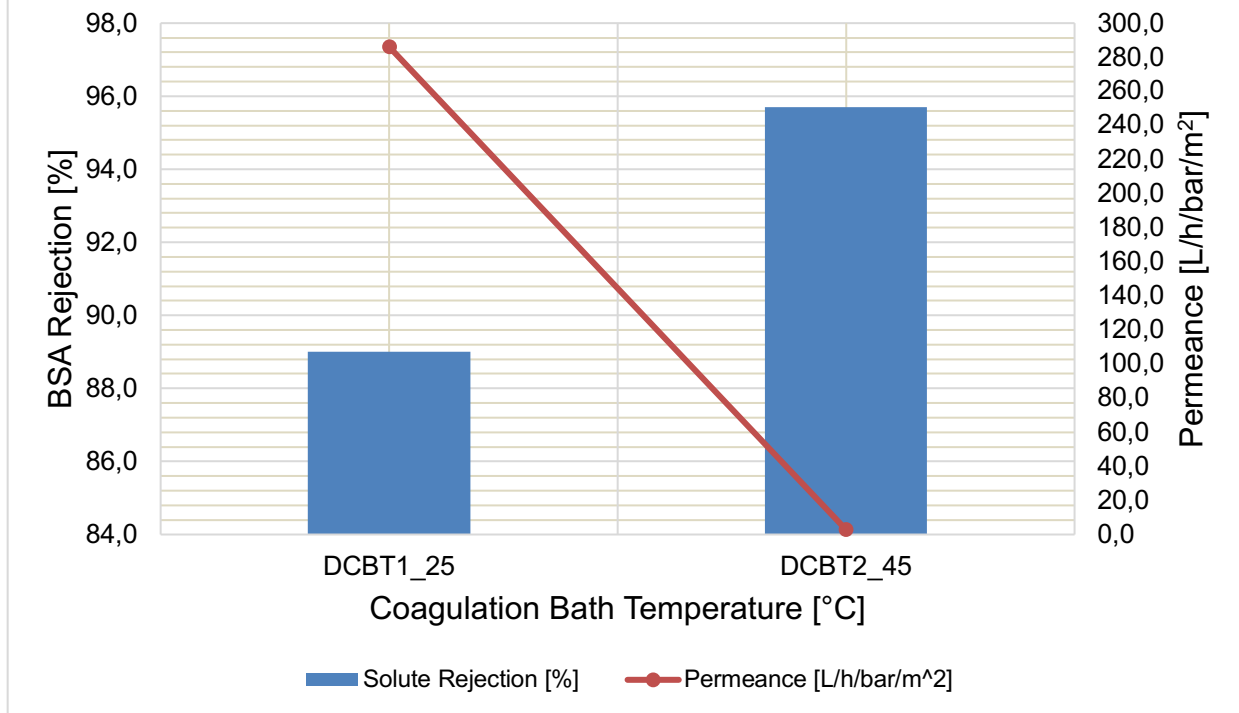


Figure 51: UF performance for different membranes spun at different coagulation bath temperatures

However, deductions can still be concluded from the results obtained. A compromise needs to be struck between highly permeable and highly selective membranes. Based on Figure 51 and the theory explained in previous units, it can be deduced that with rising coagulation bath temperatures, pore sizes become smaller and more closed ended. This leads to a significant decrease in permeance, but an equally significant increase in solute rejection. Such a fibre morphology can be explained through a spongy structure with a dense skin-layer. This phenomenon has been described in literature as well. Due to the increase in humidity in the air gap (due to higher coagulation bath temperatures), a formation of a fibre wall occurs that hinders fast solvent exchange.

5.4 Porosity Tests

The results obtained from the porosity tests and the effects that the examined parameters have on the fibre porosity have already been discussed in the unit before. The aim of this unit is to highlight some of the disparities and the assumptions taken for the two types of porosity experiments. The methods for geometric porosity and the gravimetric isopropanol porosity have already been explained.

Figure 52-Figure 56 are just some of the examples that illustrate the differences between the geometric and gravimetric porosity of the tested fibres. Geometric porosity tests utilise the mass of the dry fibre segment, as well as the information of the fibre dimensions from SEM pictures to calculate fibre porosity. While this test seems to be more accurate than the gravimetric isopropanol experiment, it still has some drawbacks. For one, the fibre dimensions (outer and inner diameters) as well as the

pore structure in the few SEM pictures taken are assumed to be consistent and identical over the entire length of the spun fibre, which might not be the case. It is also assumed that the fibre is completely dried when weighed. However, very small amounts of NMP, water and/or other post-treatment fluid might still be present in the pores, since the drying takes a significant amount of time. It is also assumed that the pores of the dried fibres are intact and in the same condition as when they were freshly spun. There has been discussion in literature over the possible collapse and damage to the pore structure when the fibres are left to dry over a period of a few days.

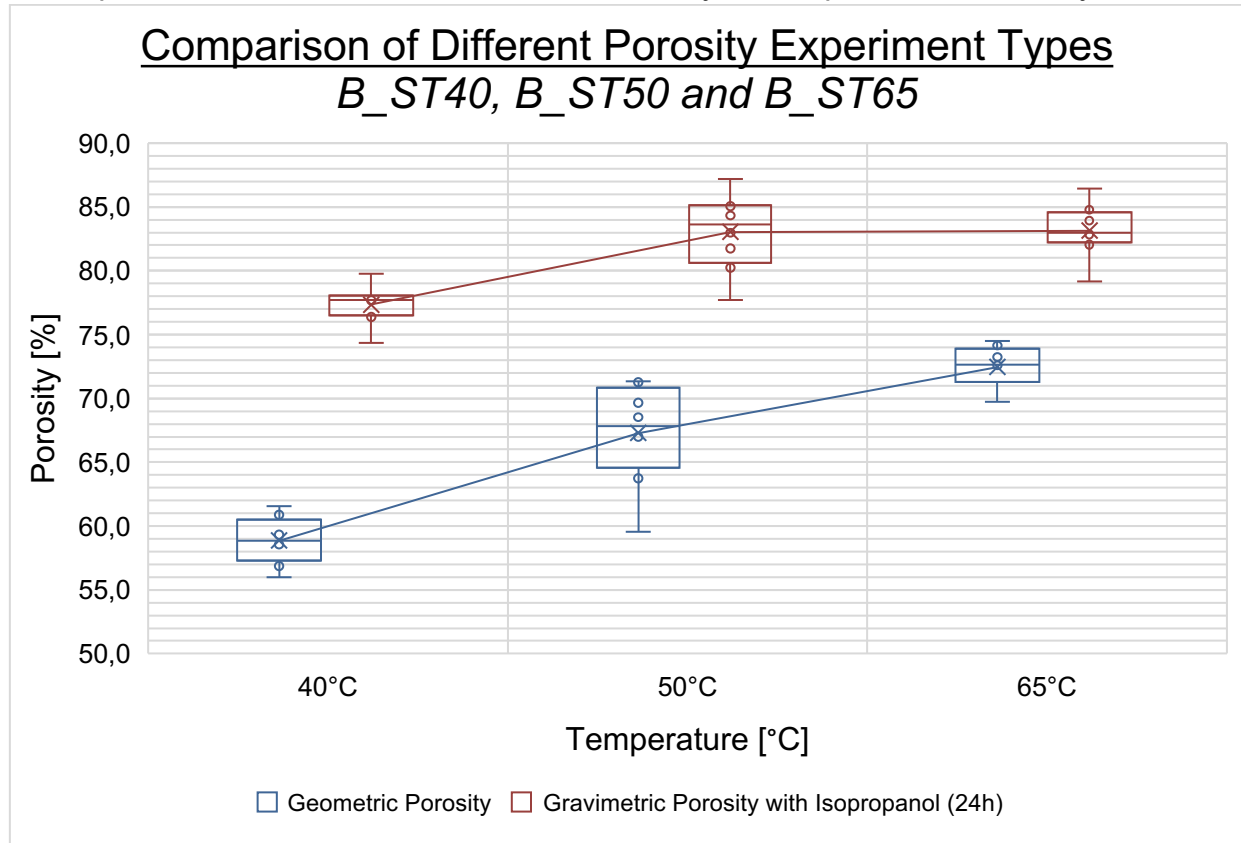


Figure 52: Comparison of geometric and isopropanol porosity experiments; temperature variation

Even more assumptions need to be met when considering the isopropanol porosity experiment. This test requires an additional weighing of the wet fibre segment after a period submerged in isopropanol. Such a weighing (carried out on an analytical scale) requires speed as isopropanol is a volatile compound and quickly evaporates into the atmosphere, thus skewing the weighing to be less than the correct weight. Secondly, when the fibre is taken out of the isopropanol, a certain amount of isopropanol is present on the lumen and fibre walls, skewing the reading to be more than what the correct reading could be. This is due to the surface tension of the isopropanol as the isopropanol cohere with one another on the fibre surfaces. Another reason for higher porosities reported with this method is that a small amount of liquid drips onto the weighing scale underneath the fibre, increasing the weight to be measured. It is almost impossible to separate such effects from this process, as it is hard to gauge just how much isopropanol is in the fibres and how much of the fluid is on the weighing scale or undergo cohesion on the walls of the lumen and outer surface.

This process depicts a much higher variation between the results as well. In nearly all comparisons (Figure 52-Figure 56), the porosity values for the isopropanol

porosity have values that span a higher range as compared to their geometric porosity value counterparts.

With more experiments being performed, it was also evident that the longer period of time in isopropanol somewhat reduced the wide deviation of the porosity values and brought them closer to the geometric porosity values. This suggests that a longer period of submersion leads to a higher probability that the isopropanol fills all the pores to their entirety, giving a more accurate and precise value. However, it has also been established that long periods of isopropanol submersion led to damage to the pores and pore walls. This should be kept in mind when performing porosity tests with solvents like isopropanol.

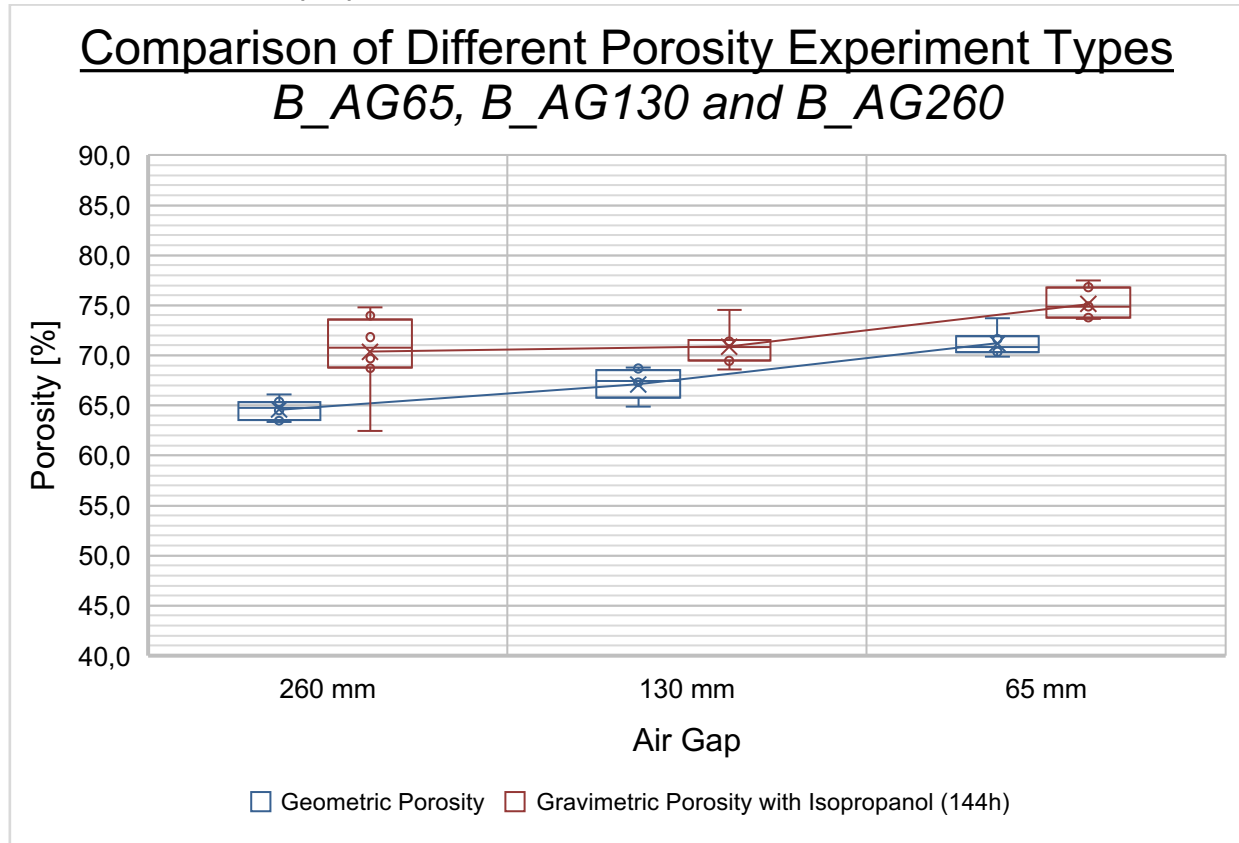


Figure 53: Comparison of geometric and isopropanol porosity experiments; airgap variation

More porosity experiments were conducted with different fluids at different durations (Figure 56). As can be seen, isopropanol porosity experiments for only three hours display a wide deviation from the median porosity. This improves when the period is increased to 72 hours. However, here the question lies if the porosities are higher due to better filling of the pores or damage of the pores. Water was also used as the submerging liquid and this experiment was carried out similarly for three days. Water has a higher surface tension than isopropanol, and thus is a worse surfactant than isopropanol. Isopropanol can fill and cover pores much more so than water in the same amount of time. All porosity experiments performed with fluids, however, show a much higher range of porosity values than the geometric porosities. This is because this method was calculated using mathematical formulae, dry fibre weight and the geometric properties of the fibres (from SEM pictures).

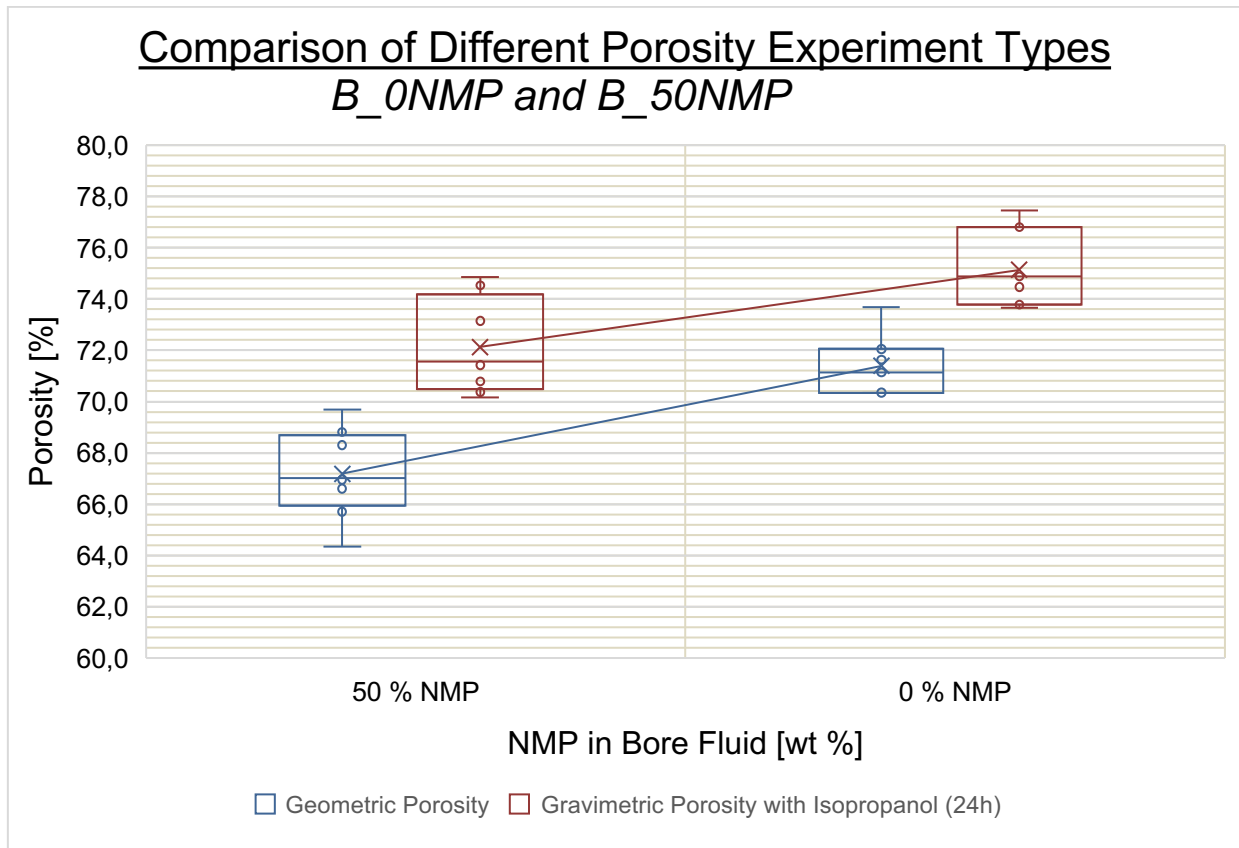


Figure 54: Comparison of geometric and isopropanol porosity experiments; NMP concentration variation

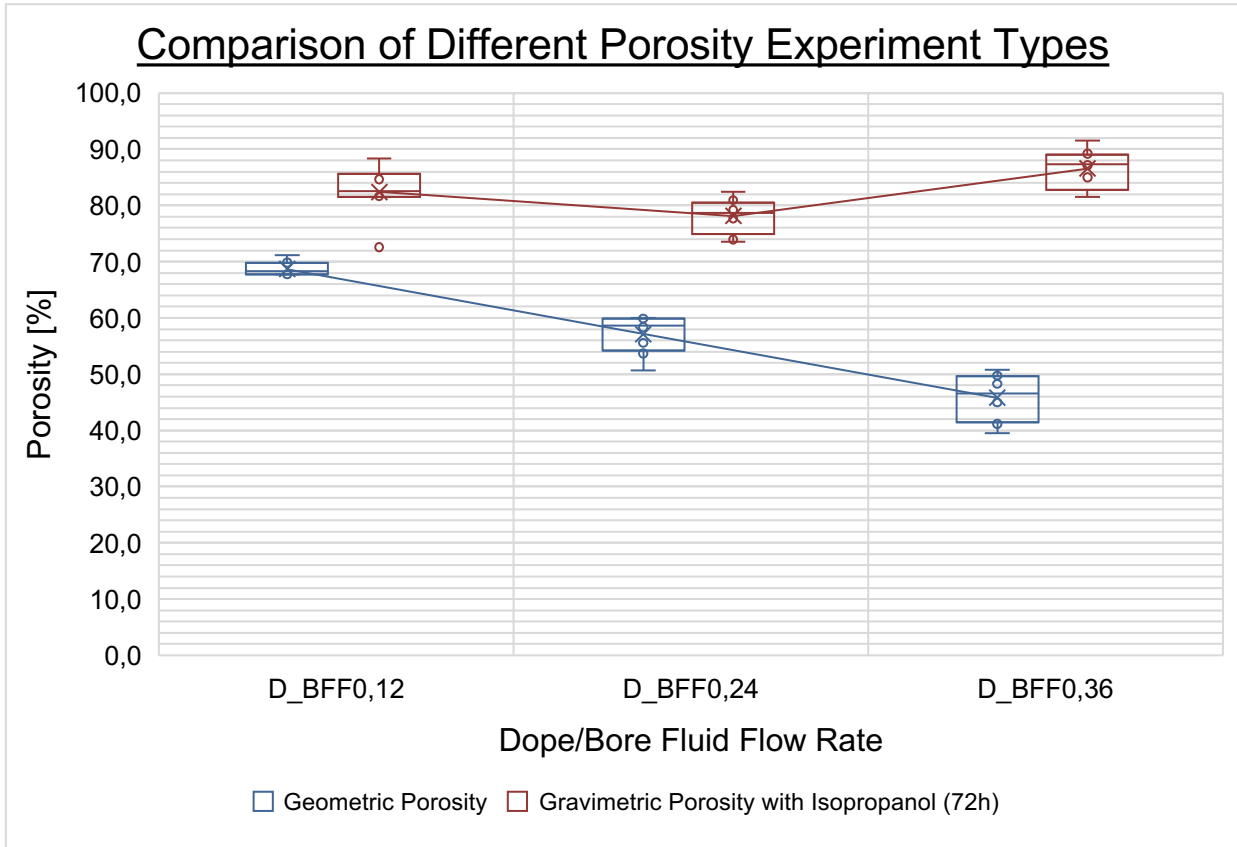


Figure 55: Comparison of geometric and isopropanol porosity experiments; flow rates variation

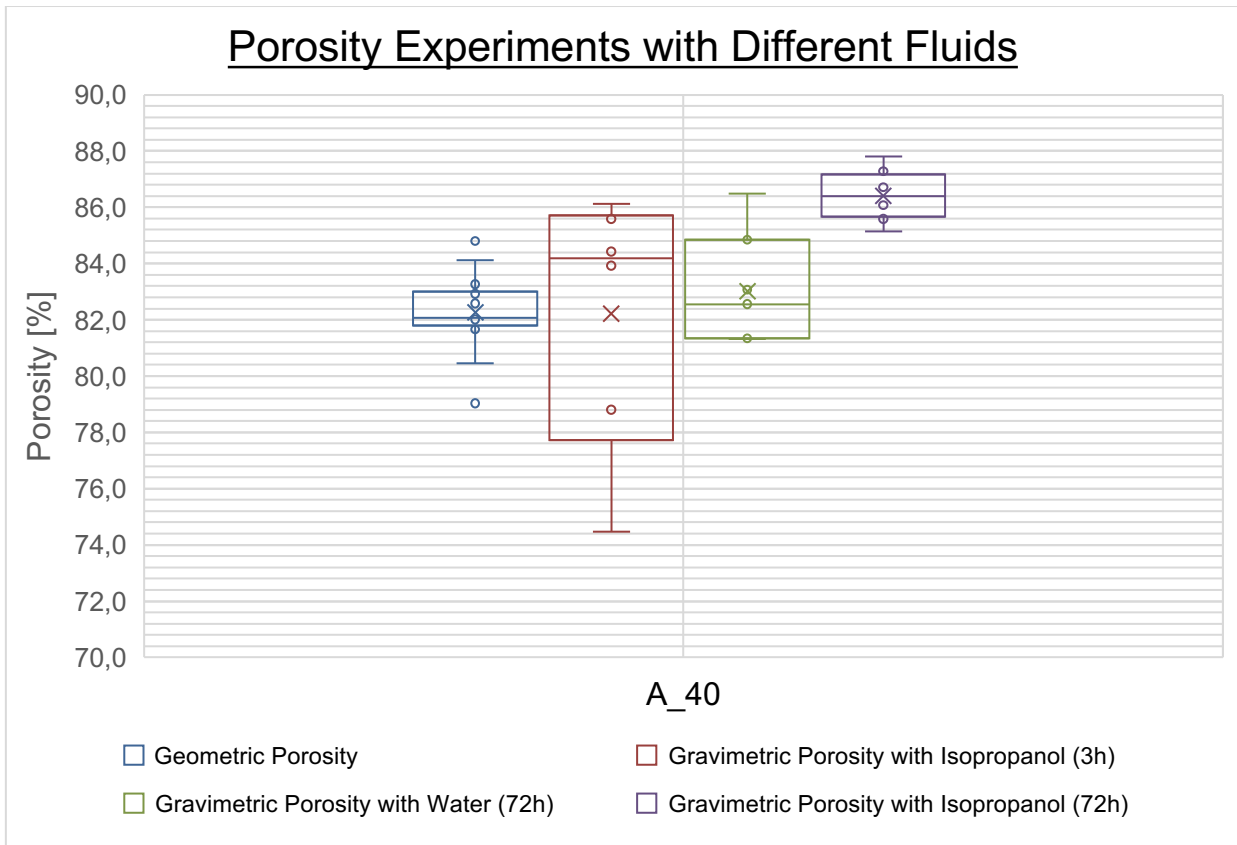


Figure 56: Comparison of four different fluids

5.5 Gas Separation Tests

Over the course of this thesis, multiple experiments have been conducted as a validation or a proof of concepts of sorts. As this was the first time the new NIPS modular plant was operated, several test runs were performed. Several gas separation experiments were performed so that documentation of the operation and usage of the NIPS and the gas separation plant could be carried out. While the results themselves might not always adhere to what is observed in literature, it is still a start and proof enough that viable fibres can be produced in the lab environment.

Three different gas separation (GP) tests were conducted for evaluation in this thesis: PES concentration variation with B_40 and C:40, spinneret temperature variation with C_65 and C_40 and the effect of PDMS coating with C_PDMS40.

5.5.1 Influence of Polymer Concentration in Dope Solution on Permselectivity Performance

From the results outlined from Figure 57 and Table 23, there is no seeming difference in the selectivity or pure gas permeance with an increase in PES concentration in the dope. While a connection is seen in literature with an inverse relationship between water flux and polymer concentration in the dope, very few studies could be found that attribute a difference in gas permeance and selectivity to polymer concentration in the dope.

Table 23: Selectivity of carbon dioxide to nitrogen with two different spinning dopes

delta P [bar]	Selectivity	
	B_ST40	C_40
	CO ₂ /N ₂	CO ₂ /N ₂
1,1	0,91	0,97
2,0	0,85	0,98
3,0	0,34	0,99

Results show that the fibres exhibited almost no selectivity between carbon dioxide and nitrogen, despite of the significant decrease in porosity between B_40 and C_40. There also was no difference to be found between the permeances of either gas. Permeance of both gases increased slightly with increasing pressure differences. Dismal results can be attributed to the fact that B_40 and C_40, while being one of the very first fibres that showed favourable geometries and thicknesses, were some of the earliest fibres to be tested using the gas separation unit in this thesis. It is highly probable that these fibres were rife with imperfections and pinholes, as is very typically the case with PES hollow fibres. The spike at 3 bars in Figure 57 for nitrogen for B_40 is most probably due to a rupture within the fibres, where nitrogen was able to flow with little to no resistance. Thus, the point is not shown as it does not represent the correct reading for the nitrogen permeance at 3 bars.

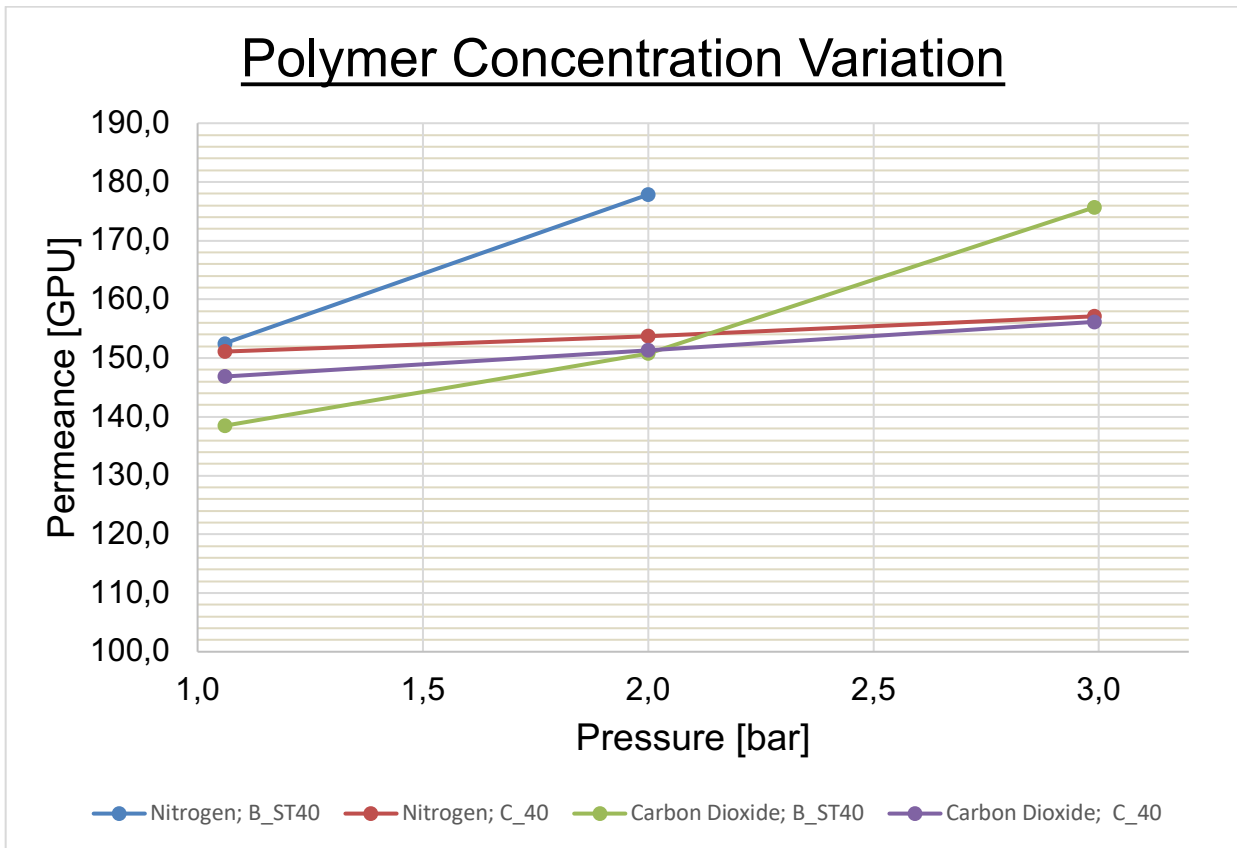


Figure 57: Permeance of nitrogen and carbon dioxide at 1,1-3 bar for modules built with fibres spun from spinning dopes A and B

5.5.2 Influence of Temperature of Dope Solution on Permselectivity Performance

C_65 and C_40 fibres were picked to evaluate the effect of spinneret and dope temperature on the gas separation performance of the fibres. Table 24 and Figure 58 display the results of this experiment and the SEM pictures for both fibres in Table 28.

C_65 shows a decrease in permeance for both nitrogen and carbon dioxide with increasing pressures. This can be due to the way the fibres were potted into the module. If they were not stretched properly enough that they stay taut even after the resin has been processed and cut, then the fibres may collapse as pressure is increased. This leads to a decrease in permeance as the gas experiences an even higher resistance as it flows through the fibres. C_40 shows a peak at 0,88 bar for both nitrogen and carbon dioxide before dramatically decreasing. This could be due to an error in noting down the measurement (flow rate measured by the definer).

Table 24: Selectivity of carbon dioxide to nitrogen at two different spinneret temperatures

delta P [bar]	Selectivity	
	C_65	C_40
	CO ₂ /N ₂	CO ₂ /N ₂ ; C
0,6	0,87	1,01
0,9	0,83	0,94
1,3	0,84	0,97

Selectivity does rise with decreasing spinneret temperature, albeit only slightly. Nevertheless, this can be attributed to the fact that porosity and the pore structure of the spun fibres decrease with decreasing spinneret temperature. Additionally, fibre dimensions are seen to decrease with increasing spinneret temperature. This change in morphology is responsible for the observed effect.

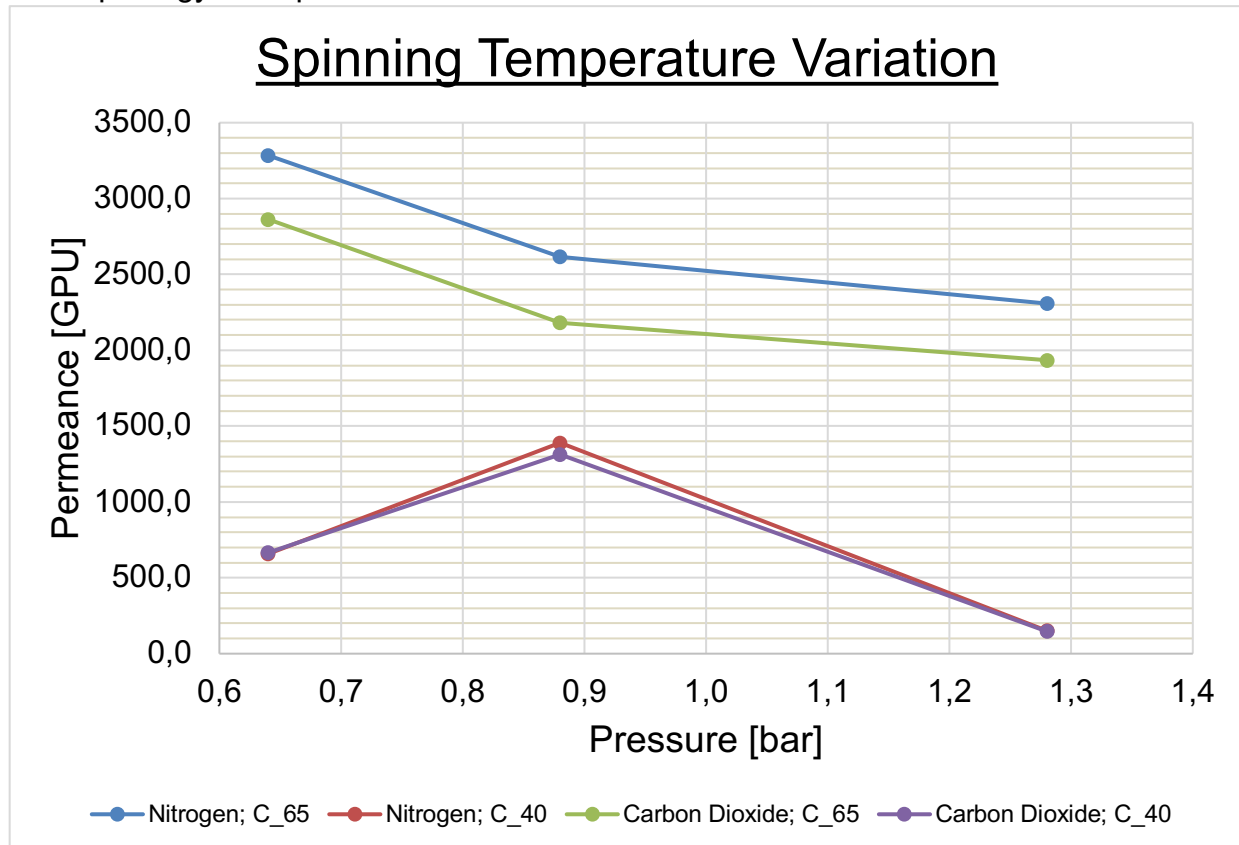


Figure 58: Permeance of nitrogen and carbon dioxide at 0,6-1,3 bar for modules built with fibres spun from spinning dope C

5.5.3 Influence of PDMS Coating on Permselectivity Performance

Finally, an attempt was made to improve the GP performance of the fibres. As it is quite difficult to spin defect-free PES hollow fibres, it was decided to coat the fibres with PDMS. The coating process is described in a previous unit. The benefits of coating fibres have also been lengthily discussed as well. The results obtained from this experiment were much more favourable than of the GP tests above.

Table 25 shows the selectivity of C and C_PDMS40 fibres. The selectivity is almost doubled at all pressures. This is one of the effects of PDMS, as it heals the outer layer and acts as a selective agent for carbon dioxide. This effect, while measurable, is still lower than what is recorded in literature. This can be since the spinning process requires a great deal more optimization and proper handling to produce fibres that show favourable qualities.

Table 25: Selectivity of carbon dioxide to nitrogen; module compared with no coating and PDMS coating

Selectivity		
	C_40	C_PDMS40
delta P [bar]	CO ₂ /N ₂	CO ₂ /N ₂
0,69	1,01	1,48
0,93	1,16	3,01
1,18	0,94	2,02

Figure 59 shows the effect of the PDMS coating on the permeance of nitrogen and carbon dioxide. It is evident that the coating also significantly lowers the permeances of nitrogen and carbon dioxide. This is due to the healing effect of the PDMS coating on the outer layer of the fibres. The coating covers any imperfections, defects and pinholes on the outer surface, preventing the gas from flowing through these imperfections, resulting in undesired results. Secondly, the PDMS layer also aids in differentiating nitrogen and carbon dioxide leading to a difference in permeance of each gas.

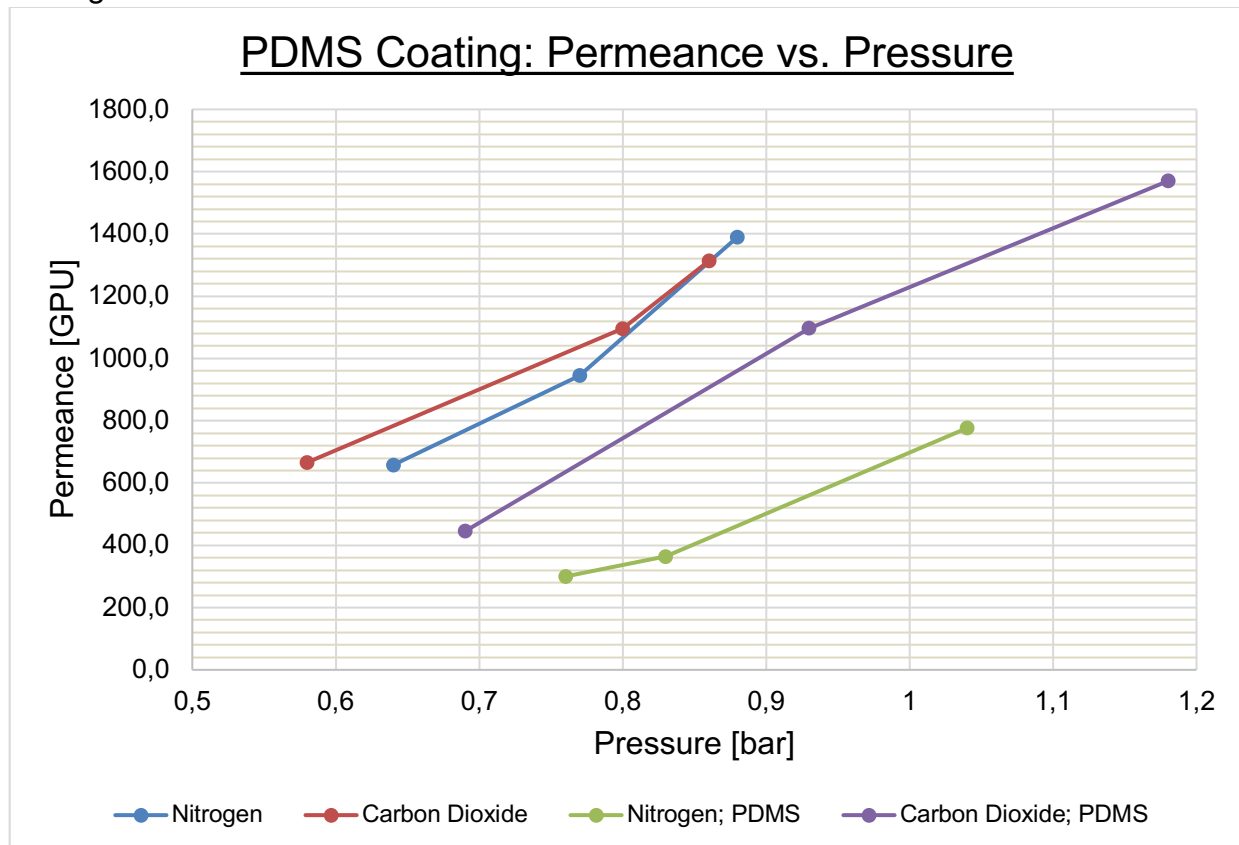


Figure 59: Permeance of nitrogen and carbon dioxide at 0,69-1,18 bar for modules built with fibres spun with spinning dope C; and coated with PDMS

The method of coating was also not the most ideal either. Once the module was built, the PDMS was injected into the module through the shell side. And allowed to pour from the opposing shell side. This leads to a chance that the fibres were not uniformly coated, and therefore the effect of PDMS not fully measurable. It is necessary to find a more optimized method of coating that uniformly covers all the fibres to be embedded in the module.

It can be deduced that the fibres that were tested with the GP unit were merely unsuitable for gas separation purposes. In contrast, more interesting and favourable results were obtained with UF experimentation, although even that experimentation unit requires further modification and optimization.

5.6 Mechanical Stability

5.6.1 Influence of Polymer Concentration in Dope Solution on Mechanical Stability

Lastly, Figure 37 shows the effect of PES concentration in the dope solution on the elongation of the fibres. It is evident that the higher the PES concentration in the dope solution, the elongation at break and tensile strength is larger. Fibres spun from D_40 depict an elongation at break nearly twice as large as B_ST40 and almost four times as large as A_40.

Table 26: Stress-strain parameters for fibres spun with four different spinning dopes

Parameter	Identifier			
	A_40	B_ST40	D_40	E_40
Young's Modul (E-Modulus) [cN/mm ²]	51,8	51,8	51,8	11,2
Tensile strength [cN/mm ²]	260	375	475	155
Elongation at break [%]	40	85	135	35

While the Young's Modul stays identical for all three samples, the D_40 exhibit a higher capability of withholding tensile stress (Table 26). This is due to the increase in PES concentration and the resulting effects in fibre morphology. Increasing PES concentrations lead to fibres with lower porosities but higher fibre dimensions. This increased thickness aids in the mechanical stability of the fibres. There is a higher number of PES macromolecules present in the fibre, giving it its mechanical stability.

E_40 showed a smaller Young's Modul as well as comparatively lower tensile strength and elongation at break as compared to A_40 (Figure 60). This is due to the pore-forming quality of PEG. The higher the porosity and thinner the fibre, the less mechanically stable the fibre will be.

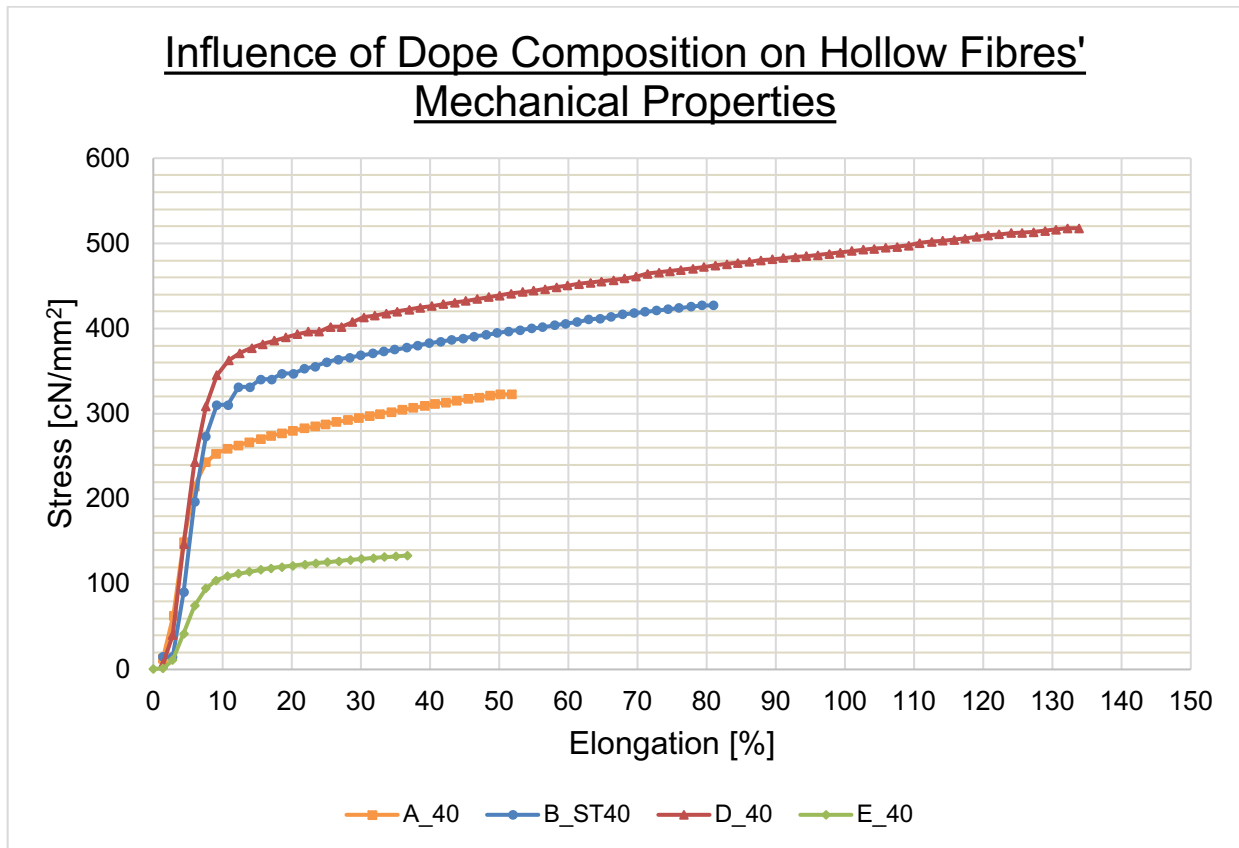


Figure 60: Stress-strain diagram of fibres spun with four different spinning dopes

6 Conclusions

The aim of this thesis was to explore the lab-scale production of PES hollow fibre membranes and to develop an all-encompassing method from scratch. The newly built inhouse modular NIPS plant was to be taken under operation to spin hollow fibres that can be utilised for applications in dialysis, blood oxygenation and other medical applications. This thesis has shown that while a long path lies until such fibres can be spun, with further optimisation and experience, the potential is clearly there. Additionally, the method of initiating from the polymer itself to modules ready for testing required specific documentation and evaluation, so that future research can be built upon this basis. The theory of demixing and NIPS was to be experimented and tested with as well. Considering the number of parameters and decisions that can influence the end result, this thesis barely scratches the surface of what is possible and what is open to further research.

Out of the parameters that are listed in Figure 24, the air gap, PES concentration in the dope, temperature of the spinneret and dope, coagulation bath temperature, additives, flow rates and post-treatment (PDMS coating) were chosen and their effects on fibre morphology, porosity, mechanical stability, UF and GP performance were examined. Not all results showed a complete alignment with the theory behind the spinning and the NIPS process. However, this fact proves that further research and operation with this NIPS plant is absolutely crucial. The theoretical framework within which the experiments were carried out, although contradicting in many aspects in multiple papers and studies, could be unambiguously observed.

The operation and production of the spinning plant requires a certain amount of expertise, experience, and optimisation. This is the grounding reason why the focus in this thesis lies on the SEM characterization and porosity testing. Before any UF and GP tests could be performed, it was imperative that the fibres have the desired uniform thickness and geometry, as well as the desired pore structure and porosity.

Results show that dope temperature and composition have a significant effect on viscosity. This in turn plays a large role in fibre porosity and pore structure. Parameters like the air gap length, dope and bore fluid flow rates and compositions, coagulation bath temperatures exhibited expected effects on fibre porosity and morphology. Flow rate variation as well as coagulation bath temperature were seen to have a profound impact on the UF performance of the fibres. While the fibres were probably not suited for GP purposes, the PDMS coating exhibited promising and expected results. All these results point to a direction where, with further development, process optimization and experimentation, fibres can be spun that exhibit favourable and desired properties. The spinning plant has already been utilised to produce fibres that depict favourable qualities. This in part, is due to the optimisation of the spinneret and the initial process part of demixing, which is extremely important for the demixing process and the way the fibres will turn out. Literature states that the spinning process is difficult to reproduce and requires a lot of practice and experience until desired fibres can be spun. This can be seen by the progression of the SEM pictures, UF performance and the module building process in this thesis.

Lastly, the operation of the NIPS plant opens many doors for further development. Different additives, polymers, solvent-nonsolvent systems can be experimented with, depending on the purpose of the end fibre. Different thermal pre-

treatments can be performed to alter the polymer or dope properties, that indirectly affect fibre properties. This thesis has only barely scratched the surface with the parameter variation that can be performed with the NIPS process plant. Different spinnerets could be utilised, different geometries could be produced as well. Further optimisation in the varying post-treatments and coating methods is necessary to produce defect-free fibres. Module building and porosity testing can be optimised further by varying the type of resin, module housing etc. The inhouse UF unit requires a better weighing scale as well as an easier way to control the pressure difference. Other solutes can be used for rejection experiments. More sophisticated characterisation methods such as atomic force microscopy (AFM), permoporometry etc. can be put to use as well. Thus, it is increasingly imperative to research, optimise and develop further applications, where such asymmetric membranes can be utilised.

7 Tables of Tables

Table 1: Overview of Technical Membrane Processes [3].....	7
Table 2: Some parameters for module design [1]–[3], [12], [14]–[16].....	18
Table 3: Membrane Separation Processes [1]–[3], [12]–[14], [18], [19].....	23
Table 4: Pressure-Driven Membrane Separation Processes [1]–[3], [11], [13], [14], [18], [19]	24
Table 5: An overview of polymers utilized for membrane production [2], [3], [6], [9], [14]–[16], [19], [21], [24]	33
Table 6: Classification of solvent-nonsolvent pairs [3]	52
Table 7: Overview of dope solutions used; *data linearly extrapolated	66
Table 8: Spinning parameters with different spinning dopes for different experiments performed; Key: Spinning Dope_Unique ParameterToBeTested, e.g., B_ST30 = dope B spun at spinneret temperature 30 °C; BFF: bore fluid flowrate; AG: airgap; CT: coagulation bath temperature	68
Table 9: Fibre dimensions and porosities of four identifiers at spinneret temperature 40 °C	75
Table 10: Fibre dimensions and porosities of hollow fibres spun from spinning dope B at four different spinneret temperatures	76
Table 11: Fibre dimensions and porosities of hollow fibres spun from spinning dope B at three different air gaps	77
Table 12: Fibre dimensions and porosities of hollow fibres spun from spinning dope B spun with two different bore fluid compositions	77
Table 13: Fibre dimensions and porosities of hollow fibres spun from spinning dopes A, E and F with different additives	77
Table 14: Fibre dimensions and porosities of hollow fibres spun from spinning dope D at different bore fluid flowrates	77
Table 15: Fibre dimensions of hollow fibres spun from spinning dope D at different coagulation bath temperatures	78
Table 16: Permeance and solute rejection rate for spinning dope D at two different flow rates	78
Table 17: Permeance and solute rejection rate of hollow fibres spun for spinning dope D at two different coagulation baths	79
Table 18: Permeance and selectivity for fibres spun with spinning dope C at spinneret temperatures 40 and 65 °C	80
Table 19: Permeance and selectivity for fibres spun with spinning dopes A and B at spinneret temperature 40 °C	80
Table 20: Influence of coating on the permselectivity performance; fibres spun with spinning dope C_40	81
Table 21: Physical dimensions of the resulting hollow fibres; concentration variation	87
Table 22: Physical dimensions of the resulting hollow fibres; spinneret temperature variation	91
Table 23: Selectivity of carbon dioxide to nitrogen with two different spinning dopes	106
Table 24: Selectivity of carbon dioxide to nitrogen at two different spinneret temperatures	107
Table 25: Selectivity of carbon dioxide to nitrogen; module compared with no coating and PDMS coating	109
Table 26: Stress-strain parameters for fibres spun with four different spinning dopes	110
Table 27: SEM pictures; PES concentration variation	124

Table 28: SEM pictures; temperature variation.....	125
Table 29: SEM pictures; air gap variation	126
Table 30: SEM pictures; NMP concentration in bore fluid variation.....	127
Table 31: SEM pictures; coagulation bath temperature variation	128
Table 32: SEM pictures; flow rate variation	129
Table 33: SEM pictures; GP experiment.....	130
Table 34: SEM pictures; additive variation.....	131

8 Table of Figures

Figure 1: Maxwell's thought experiment- the demon has sorted the random disorderly system into an ordered system; H: hot, C: cold [3].....	6
Figure 2: Fundamental basis of a porous membrane system; adapted from [11].....	9
Figure 3: One means of classifying membranes; adapted from [11]	12
Figure 4: Schematic diagrams of various membranes (classified by their structure and morphology) [1]	13
Figure 5: Membrane structure classification: pore size of the three main types of porous membranes [14]	14
Figure 6: Four standard technically relevant membrane geometries; adapted from [2]	15
Figure 7: Schematic depiction of two basic module configurations [3]	15
Figure 8: Flux decline in a dead-end configuration in filtration processes [3]	16
Figure 9: UF membranes are rated on the nominal MWCO, but the shape of the molecule also plays a massive role in the retentivity of the solute. Linear molecules are quickly passed, whereby globular modules of the same molecular weight may be rejected. The adjoining table shows typical results of testing globular protein and linear polydextran for a polysulfone membrane [1].	17
Figure 10: Top left: Plate-and-Frame module: a) components in flat sheet filtration modules; b) cross-section of flat sheet stack in a housing and the streams of feed, permeate and retentate; c) circular flat sheet module; d) rotating module design [2]; Top right: Capillary module: a) cross-section of the module; b) entrance/exit of the module where the membranes are potted in the shell tube [2]; Middle left: Tubular module with 30 tubes connected in series; permeate collected in permeate manifold [1]; Middle right: Two module designs for hollow fibre modules; a) shell-side feed modules; b) bore-side feed modules [1]; Bottom: Spiral-wound module; exploded and cross-section display; feed passes across the membrane surface where a portion enters the membrane envelope and flows towards the collection pipe [1]	19
Figure 11: RO, UF, MF and filtration are similar pressure-driven processes, basically differing in the average pore size of the membrane. Discrete pores do not exist in RO membranes, and therefore mass transport happens through statistically distributed free volume areas [1]	25
Figure 12: Differing transport mechanisms dependant on pore size within the membrane matrix [17]; dp : pore diameter; ds : molar size of solute; λ : free path of solute molecules.....	26
Figure 13: Characteristic pore geometries found in porous membranes [3].....	26
Figure 14: Porous membranes characterisation by their tortuosity, porosity, and average pore diameter [1]	27
Figure 15: Transport of spherical particles of two different components through a circular pore; a: radius of a particle; r: pore radius; adapted from [2].....	29
Figure 16: Flory-Huggins lattice model: molecular distribution in a binary system of (a) monomers and (b) polymers in a solvent [9]	39
Figure 17: (a) Dependence of ΔG_m on χ (left) (b) Binodal and spinodal curves illustrated for a polymeric solution as a function of the volume fraction (right) [9], [18]	41
Figure 18: (a) Stable (b) unstable (c) metastable states of polymer/solvent mixture [18]	43

Figure 19: (a) Chemical potential (b) stable/metastable/unstable regions in ΔG_m graph [18]	44
Figure 20: Left: tie lines for an isothermal graph: A and B lie on the binodal for a specific composition of the solution in consideration (blue point); right: ternary phase diagram for a NIPS process [9], [18]	45
Figure 21: Membrane formation through the NIPS process [17]	46
Figure 22: Schematic representation of the solution composition path immediately after immersion; t: top of the film; b: bottom of the film. Left: instantaneous demixing; right: delayed demixing [3]	47
Figure 23: An example of a spinning unit to spin hollow fibres [19]	49
Figure 24: Influence of parameters on the spinning of hollow fibres membranes.....	50
Figure 25: Delay time of demixing for 15% cellulose acetate/solvent solutions in water [3]	52
Figure 26: Precipitation in the dry-jet wet and wet spinning process [38]	55
Figure 27: Effect of bore fluid composition on the ternary phase diagram: (a) NMP/water (b) G/water (c) EG/water and (d) comparison of the binodal for membranes made with different bore fluids [45]	59
Figure 28: (a) Dope solution production process: heating mantle (1), triple-necked round-bottom flask (2), Dimroth condenser (3), Stirring motor (4), Thermoelement (5) (left); (b) Polyethersulfone/1-methyl-2-pyrrolidone dope solution (top right); (c) Polyethersulfone pellets (bottom right).....	65
Figure 29: The spinning equipment for the production of hollow fibre membranes: convectional thermostats for the dope solution (1), for the bore fluid (2) and the spinneret (3), motors and gearbox for the pumps (4), dope solution pump (5), bore fluid pump (6), pump regulation (7), bore fluid supply pipe (8), polymer supply pipe (9), spinneret (10), spinneret heating pipes (11), coagulation bath (12), fibre with a deflection roller (13), take-up conduction (14), take-up winder drum (15), take-up regulation (16), wash bath (17), convection thermostat for the baths (18), emergency switch (19), safety and electrical box of the equipment (20).	70
Figure 30: Module of 25 hollow fibres; complete module (far left), view from the lumen (centre) and view from the shell side (far right)	71
Figure 31: The ultrafiltration unit (left) pressurized air connection (1), pressure indicator (2), feed tank (3), flow indicators (4), needle valves (5), membrane module (6), permeate tank (7), extra tank for a feed (for dead-end configuration)/retentate tank (8), weighing scale (9); flow chart of the ultrafiltration unit built to determine pure water permeance (right).....	72
Figure 32: Gas separation unit with MFC (1), pressure sensors (2), steel valves (3), definer (4) and the membrane module (5).....	73
Figure 33: Influence of temperature variation on the dope viscosities for multiple spinning dopes used in this thesis.....	74
Figure 34: Influence of PES concentration on dope viscosity for spinning dopes A, B and D	75
Figure 35: SEM photographs of hollow fibres spun with increasing spinneret temperature : from the top left: B_ST30, B_ST40, and from bottom left: B_ST50 and B_ST65	76
Figure 36: BSA absorption spectrum for spinning dope D_BFF0,12	79
Figure 37: Influence of PES concentration on the stress strain test of spun hollow fibres from three different spinning dopes	81

Figure 38: Lumen surface of B_AG260 fibres; sample prepared by cutting the hollow fibre in half and placing the fibre flat on to the sample holder to be able to observe the inner surface..... 84

Figure 39: Influence of air gap length on fibre dimensions and porosity for hollow fibres spun from spinning dope B; three different air gap lengths set: 65, 130 and 260 mm 85

Figure 40: Die swell illustration in hollow fibre formation [59] 87

Figure 41: Influence of the PES concentration in the dope solution on fibre dimensions and porosity..... 89

Figure 42: Influence of the spinneret temperature on fibre dimensions and porosity..... 90

Figure 43: Lumen surfaces of B_0NMP (top) and B_50NMP (bottom)..... 92

Figure 44: Influence of the amount of NMP in the bore fluid on fibre dimensions and porosity..... 93

Figure 45: Influence of different additives on fibre dimensions..... 94

Figure 46: Influence of different additives on fibre porosity 95

Figure 47: Surface porosity on the shell side; A_40 (left), E_40 (right) and F_40 (bottom)..... 96

Figure 48: Influence of dope/bore fluid flow rates on fibre dimensions..... 97

Figure 49: Influence of dope/bore fluid flow rates on fibre porosity 98

Figure 50: Influence of dope/bore fluid flow rate on UF performance..... 99

Figure 51: UF performance for different membranes spun at different coagulation bath temperatures 101

Figure 52: Comparison of geometric and isopropanol porosity experiments; temperature variation 102

Figure 53: Comparison of geometric and isopropanol porosity experiments; airgap variation..... 103

Figure 54: Comparison of geometric and isopropanol porosity experiments; NMP concentration variation 104

Figure 55: Comparison of geometric and isopropanol porosity experiments; flow rates variation..... 105

Figure 56: Comparison of four different fluids..... 105

Figure 57: Permeance of nitrogen and carbon dioxide at 1,1-3 bar for modules built with fibres spun from spinning dopes A and B 107

Figure 58: Permeance of nitrogen and carbon dioxide at 0,6-1,3 for modules built with fibres spun from spinning dope C..... 108

Figure 59: Permeance of nitrogen and carbon dioxide at 0,69-1,18 bar for modules built with fibres spun with spinning dope C; and coated with PDMS..... 109

Figure 60: Stress-strain diagram of fibres spun with four different spinning dopes 111

9 References

- [1] R. W. Baker, *Membrane technology and applications*, Third Edition. Chichester, West Sussex ; Hoboken: John Wiley & Sons, 2012.
- [2] H. Strathmann, *Introduction to Membrane Science and Technology*. Wiley-VCH Verlag GmbH & Co. KGaA, 2011.
- [3] M. Mulder, *Basic Principles of Membrane Technology*, 2. Kluwer Academic Publishers, 1996.
- [4] N. Peng *et al.*, 'Evolution of polymeric hollow fibers as sustainable technologies: Past, present, and future', *Prog. Polym. Sci.*, vol. 37, no. 10, Art. no. 10, 2012, doi: 10.1016/j.progpolymsci.2012.01.001.
- [5] C. F. Wan, T. Yang, G. G. Lipscomb, D. J. Stookey, and T.-S. Chung, 'Design and fabrication of hollow fiber membrane modules', *J. Membr. Sci.*, vol. 538, pp. 96–107, 2017, doi: 10.1016/j.memsci.2017.05.047.
- [6] J. Meier-Haack, M. Müller, and K. Lunke, 'Polymer Membranes for Sustainable Technologies', in *Polymers - Opportunities and Risks II: Sustainability, Product Design and Processing*, P. Eyerer, M. Weller, and C. Hübner, Eds. Berlin, Heidelberg: Springer, 2010, pp. 281–297. doi: 10.1007/978-3-642-00917-1_17.
- [7] A. Moriya, T. Maruyama, Y. Ohmukai, T. Sotani, and H. Matsuyama, 'Preparation of poly(lactic acid) hollow fiber membranes via phase separation methods', *J. Membr. Sci.*, vol. 342, no. 1–2, Art. no. 1–2, Oct. 2009, doi: 10.1016/j.memsci.2009.07.005.
- [8] A. Moriya, P. Shen, Y. Ohmukai, T. Maruyama, and H. Matsuyama, 'Reduction of fouling on poly(lactic acid) hollow fiber membranes by blending with poly(lactic acid)–polyethylene glycol–poly(lactic acid) triblock copolymers', *J. Membr. Sci.*, vol. 415–416, pp. 712–717, Oct. 2012, doi: 10.1016/j.memsci.2012.05.059.
- [9] L. De Bartolo, E. Curcio, and E. Drioli, *Membrane Systems for Bioartificial Organs and Regenerative Medicine*. Berlin/Boston: Walter de Gruyter GmbH, 2017.
- [10] J. Black, *Biological Performance of Materials: Fundamentals of Biocompatibility, Fourth Edition*. CRC Press, 2005.
- [11] T. Melin and R. Rautenbach, *Membranverfahren: Grundlagen der Modul- und Anlagenauslegung*, 3., Aktualisierte und erw. Aufl. Berlin ; New York: Springer, 2007.
- [12] A. K. Pabby, S. S. H. Rizvi, and A. M. Sastre, *Handbook of Membrane Separations: Chemical, Pharmaceutical, Food, and Biotechnological Applications*. CRC Press, 2009.
- [13] M. K. Purkait, M. K. Sinha, P. Mondal, and R. Singh, 'Chapter 1 - Introduction to Membranes', in *Interface Science and Technology*, vol. 25, M. K. Purkait, M. K. Sinha, P. Mondal, and R. Singh, Eds. Elsevier, 2018, pp. 1–37. doi: 10.1016/B978-0-12-813961-5.00001-2.
- [14] T. A. Saleh and V. K. Gupta, 'Chapter 3 - Membrane Classification and Membrane Operations', in *Nanomaterial and Polymer Membranes*, T. A. Saleh and V. K. Gupta, Eds. Elsevier, 2016, pp. 55–82. doi: 10.1016/B978-0-12-804703-3.00003-6.
- [15] S. Ramakrishna, Z. Ma, and T. Matsuura, *Polymer Membranes in Biotechnology*. London: Imperial College Press, 2011.
- [16] C. Charcosset, '1 - Principles on membrane and membrane processes', in *Membrane Processes in Biotechnology and Pharmaceutics*, C. Charcosset, Ed. Amsterdam: Elsevier, 2012, pp. 1–41. doi: 10.1016/B978-0-444-56334-

- 7.00001-0.
- [17] Endre Nagy, 'Chapter 2 - Membrane Materials, Structures, and Modules', in *Basic Equations of Mass Transport Through a Membrane Layer; Second Edition*, 2nd ed., Elsevier, 2019. doi: 10.1016/B978-0-12-813722-2.00002-9.
- [18] N. Hilal, A. F. Ismail, and C. Wright, *Membrane Fabrication*. CRC Press, 2015.
- [19] N. Kubota, T. Hashimoto, and Y. Mori, 'Microfiltration and Ultrafiltration', in *Advanced Membrane Technology and Applications*, John Wiley & Sons, Ltd, 2008, pp. 101–129. doi: 10.1002/9780470276280.ch5.
- [20] T. A. Saleh and V. K. Gupta, 'Chapter 1 - An Overview of Membrane Science and Technology', in *Nanomaterial and Polymer Membranes*, T. A. Saleh and V. K. Gupta, Eds. Elsevier, 2016, pp. 1–23. doi: 10.1016/B978-0-12-804703-3.00001-2.
- [21] S. P. Nunes and K.-V. Peinemann, 'Presently Available Membranes for Liquid Separation', in *Membrane Technology*, John Wiley & Sons, Ltd, 2006, pp. 15–38. doi: 10.1002/3527608788.ch4.
- [22] C. Zhao, J. Xue, F. Ran, and S. Sun, 'Modification of polyethersulfone membranes – A review of methods', *Prog. Mater. Sci.*, vol. 58, no. 1, Art. no. 1, Jan. 2013, doi: 10.1016/j.pmatsci.2012.07.002.
- [23] P. T. P. Aryanti, D. Ariono, A. N. Hakim, and I. G. Wenten, 'Flory-Huggins Based Model to Determine Thermodynamic Property of Polymeric Membrane Solution', *J. Phys.: Conf. Ser.*, vol. 1090, p. 012074, Sep. 2018, doi: 10.1088/1742-6596/1090/1/012074.
- [24] L. W. McKeen, '7 - Polyimides', in *Film Properties of Plastics and Elastomers (Fourth Edition)*, L. W. McKeen, Ed. William Andrew Publishing, 2017, pp. 147–185. doi: 10.1016/B978-0-12-813292-0.00007-1.
- [25] J. Barzin and B. Sadatnia, 'Correlation between macrovoid formation and the ternary phase diagram for polyethersulfone membranes prepared from two nearly similar solvents', *J. Membr. Sci.*, vol. 325, no. 1, pp. 92–97, Nov. 2008, doi: 10.1016/j.memsci.2008.07.003.
- [26] A. Bottino, G. Camera-Roda, G. Capannelli, and S. Munari, 'The formation of microporous polyvinylidene difluoride membranes by phase separation', *J. Membr. Sci.*, vol. 57, no. 1, pp. 1–20, Apr. 1991, doi: 10.1016/S0376-7388(00)81159-X.
- [27] S.-H. Choi, F. Tasselli, J. C. Jansen, G. Barbieri, and E. Drioli, 'Effect of the preparation conditions on the formation of asymmetric poly(vinylidene fluoride) hollow fibre membranes with a dense skin', *Eur. Polym. J.*, vol. 46, no. 8, Art. no. 8, Aug. 2010, doi: 10.1016/j.eurpolymj.2010.06.001.
- [28] F. Tasselli, J. C. Jansen, F. Sidari, and E. Drioli, 'Morphology and transport property control of modified poly(ether ether ketone) (PEEKWC) hollow fiber membranes prepared from PEEKWC/PVP blends: influence of the relative humidity in the air gap', *J. Membr. Sci.*, vol. 255, no. 1, pp. 13–22, Jun. 2005, doi: 10.1016/j.memsci.2005.01.014.
- [29] Q. F. Alsalhy, H. A. Salih, S. Simone, M. Zablouk, E. Drioli, and A. Figoli, 'Poly(ether sulfone) (PES) hollow-fiber membranes prepared from various spinning parameters', *Desalination*, vol. 345, pp. 21–35, Jul. 2014, doi: 10.1016/j.desal.2014.04.029.
- [30] B. Torrestiana-Sanchez, R. I. Ortiz-Basurto, and E. Brito-De La Fuente, 'Effect of nonsolvents on properties of spinning solutions and polyethersulfone hollow fiber ultrafiltration membranes', *J. Membr. Sci.*, vol. 152, pp. 19–28, 1999, doi: 10.1016/S0376-7388(98)00172-0.
- [31] T. Liu, D. Zhang, S. Xu, and S. Sourirajan, 'Solution-Spun Hollow Fiber

Polysulfone and Polyethersulfone Ultrafiltration Membranes', *Sep. Sci. Technol.*, vol. 27, no. 2, Art. no. 2, Feb. 1992, doi: 10.1080/01496399208018871.

- [32] Z.-L. Xu and F. Alsahy Qusay, 'Polyethersulfone (PES) hollow fiber ultrafiltration membranes prepared by PES/non-solvent/NMP solution', *J. Membr. Sci.*, vol. 233, no. 1–2, pp. 101–111, Apr. 2004, doi: 10.1016/j.memsci.2004.01.005.
- [33] D. Wang, K. Li, and W. K. Teo, 'Polyethersulfone hollow fiber gas separation membranes prepared from NMP/alcohol solvent systems', *J. Membr. Sci.*, vol. 115, pp. 85–108, 1996, doi: 10.1016/0376-7388(95)00312-6.
- [34] P. van de Witte, P. J. Dijkstra, J. W. A. van den Berg, and J. Feijen, 'Phase separation processes in polymer solutions in relation to membrane formation', *J. Membr. Sci.*, vol. 117, no. 1, pp. 1–31, Aug. 1996, doi: 10.1016/0376-7388(96)00088-9.
- [35] Y. Liu, G. H. Koops, and H. Strathmann, 'Characterization of morphology controlled polyethersulfone hollow fiber membranes by the addition of polyethylene glycol to the dope and bore liquid solution', *J. Membr. Sci.*, vol. 223, no. 1–2, Art. no. 1–2, 2003, doi: 10.1016/S0376-7388(03)00322-3.
- [36] M. Khayet, 'The effects of air gap length on the internal and external morphology of hollow fiber membranes', *Chem. Eng. Sci.*, vol. 58, no. 14, pp. 3091–3104, Jul. 2003, doi: 10.1016/S0009-2509(03)00186-6.
- [37] J.-H. Kim, Y.-I. Park, J. Jegal, and K.-H. Lee, 'The effects of spinning conditions on the structure formation and the dimension of the hollow-fiber membranes and their relationship with the permeability in dry–wet spinning technology', *J. Appl. Polym. Sci.*, vol. 57, no. 13, pp. 1637–1644, 1995, doi: 10.1002/app.1995.070571310.
- [38] T.-S. Chung and X. Hu, 'Effect of Air-Gap Distance on the Morphology and Thermal Properties of Polyethersulfone Hollow Fibers', *J. Appl. Polym. Sci.*, vol. 66, pp. 1067–1077, 1997, doi: 10.1002/(SICI)1097-4628(19971107)66:6<1067::AID-APP7>3.0.CO;2-G.
- [39] B. L. Li, Y. Zhai, Y. Liu, and Y. B. Jiu, 'Preparation of polyimide hollow fiber membrane', *IOP Conf. Ser. Mater. Sci. Eng.*, vol. 770, pp. 1–7, Mar. 2020, doi: 10.1088/1757-899X/770/1/012034.
- [40] Q. Zhang, X. Lu, and L. Zhao, 'Preparation of Polyvinylidene Fluoride (PVDF) Hollow Fiber Hemodialysis Membranes', *Membranes*, vol. 4, no. 1, Art. no. 1, Mar. 2014, doi: 10.3390/membranes4010081.
- [41] D. Wang, W. K. Teo, and K. Li, 'Preparation and characterization of high-flux polysulfone hollow fibre gas separation membranes', *J. Membr. Sci.*, vol. 204, no. 1–2, Art. no. 1–2, Jul. 2002, doi: 10.1016/S0376-7388(02)00047-9.
- [42] I. M. Wienk, F. H. A. Olde Scholtenhuis, Th. van den Boomgaard, and C. A. Smolders, 'Spinning of hollow fiber ultrafiltration membranes from a polymer blend', *J. Membr. Sci.*, vol. 106, no. 3, Art. no. 3, Oct. 1995, doi: 10.1016/0376-7388(95)00088-T.
- [43] G. C. Kapantaidakis and G. H. Koops, 'High flux polyethersulfone–polyimide blend hollow fiber membranes for gas separation', *J. Membr. Sci.*, vol. 204, no. 1–2, Art. no. 1–2, Jul. 2002, doi: 10.1016/S0376-7388(02)00030-3.
- [44] T. Chung and E. R. Kafchinski, 'The effects of spinning conditions on asymmetric 6FDA/6FDAM polyimide hollow fibers for air separation', *J. Appl. Polym. Sci.*, vol. 65, no. 8, Art. no. 8, 1997, doi: 10.1002/(SICI)1097-4628(19970822)65:8<1555::AID-APP13>3.0.CO;2-V.
- [45] Y. Bang, M. Obaid, M. Jang, J. Lee, J. Lim, and I. S. Kim, 'Influence of bore

- fluid composition on the physiochemical properties and performance of hollow fiber membranes for ultrafiltration', *Chemosphere*, vol. 259, p. 127467, Nov. 2020, doi: 10.1016/j.chemosphere.2020.127467.
- [46] D. Wang, K. Li, and W. K. Teo, 'Highly permeable polyethersulfone hollow fiber gas separation membranes prepared using water as non-solvent additive', *J. Membr. Sci.*, vol. 176, pp. 147–158, 2000, doi: 10.1016/S0376-7388(00)00419-1.
- [47] F. Tasselli, J. C. Jansen, and E. Drioli, 'PEEKWC ultrafiltration hollow-fiber membranes: Preparation, morphology, and transport properties', *J. Appl. Polym. Sci.*, vol. 91, no. 2, pp. 841–853, 2004, doi: 10.1002/app.13207.
- [48] Y. Tang, N. Li, A. Liu, S. Ding, C. Yi, and H. Liu, 'Effect of spinning conditions on the structure and performance of hydrophobic PVDF hollow fiber membranes for membrane distillation', *Desalination*, vol. 287, pp. 326–339, Feb. 2012, doi: 10.1016/j.desal.2011.11.045.
- [49] J. Qin and T.-S. Chung, 'Effect of dope flow rate on the morphology, separation performance, thermal and mechanical properties of ultrafiltration hollow fibre membranes', *J. Membr. Sci.*, vol. 157, no. 1, Art. no. 1, Jan. 1999, doi: 10.1016/S0376-7388(98)00361-5.
- [50] K. Y. Wang, T. Matsuura, T.-S. Chung, and W. F. Guo, 'The effects of flow angle and shear rate within the spinneret on the separation performance of poly(ethersulfone) (PES) ultrafiltration hollow fiber membranes', *J. Membr. Sci.*, vol. 240, no. 1–2, Art. no. 1–2, Sep. 2004, doi: 10.1016/j.memsci.2004.04.012.
- [51] T.-S. Chung, J.-J. Qin, and J. Gu, 'Effect of shear rate within the spinneret on morphology, separation performance and mechanical properties of ultrafiltration polyethersulfone hollow fiber membranes', *Chem. Eng. Sci.*, vol. 55, pp. 1077–1091, 2000, doi: 10.1016/S0009-2509(99)00371-1.
- [52] J.-J. Qin, J. Gu, and T. S. Chung, 'Effect of wet and dry-jet wet spinning on the shear-induced orientation during the formation of ultrafiltration hollow fiber membranes', *J. Membr. Sci.*, vol. 182, no. 1–2, Art. no. 1–2, Feb. 2001, doi: 10.1016/S0376-7388(00)00552-4.
- [53] L. K. Wang, J. P. Chen, Y.-T. Hung, and N. K. Shamma, *Membrane and Desalination Technologies*. Totowa, NJ, UNITED STATES: Humana Press, 2010. Accessed: Dec. 01, 2021. [Online]. Available: <http://ebookcentral.proquest.com/lib/viennaut/detail.action?docID=666525>
- [54] P. Sukitpaneemit and T.-S. Chung, 'Molecular design of the morphology and pore size of PVDF hollow fiber membranes for ethanol–water separation employing the modified pore-flow concept', *J. Membr. Sci.*, vol. 374, no. 1, pp. 67–82, May 2011, doi: 10.1016/j.memsci.2011.03.016.
- [55] A. Jalali, A. Shockravi, V. Vatanpour, and M. Hajibeygi, 'Preparation and characterization of novel microporous ultrafiltration PES membranes using synthesized hydrophilic polysulfide-amide copolymer as an additive in the casting solution', *Microporous Mesoporous Mater.*, vol. 228, pp. 1–13, Jul. 2016, doi: 10.1016/j.micromeso.2016.03.024.
- [56] G. R. Guillen, G. Z. Ramon, H. P. Kavehpour, R. B. Kaner, and E. M. V. Hoek, 'Direct microscopic observation of membrane formation by nonsolvent induced phase separation', *J. Membr. Sci.*, vol. 431, pp. 212–220, Mar. 2013, doi: 10.1016/j.memsci.2012.12.031.
- [57] M. Azhari, O. Noorinah, N. Mustafa, and A. Ismail, 'Carbon Dioxide Permeation Characteristics in Asymmetric Polysulfone Hollow Fiber Membrane: Effect of Constant Heating and Progressive Heating', *Adv. Mater. Res.*, vol. 896, pp. 37–40, Feb. 2014, doi:

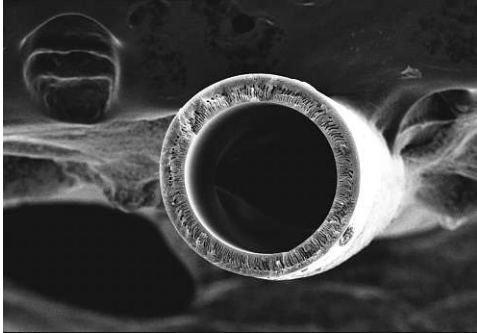
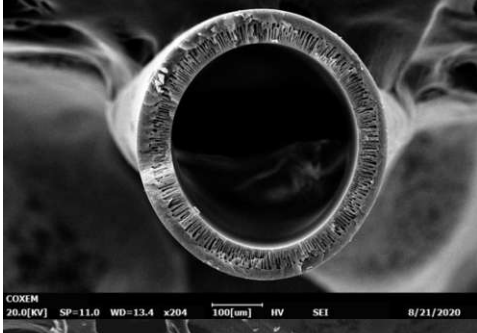
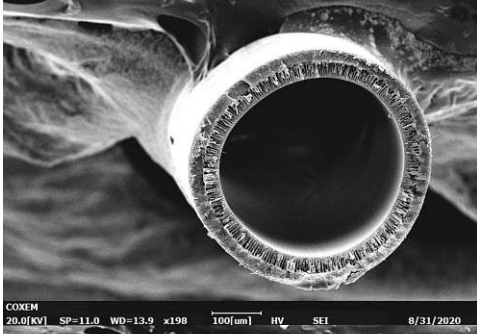
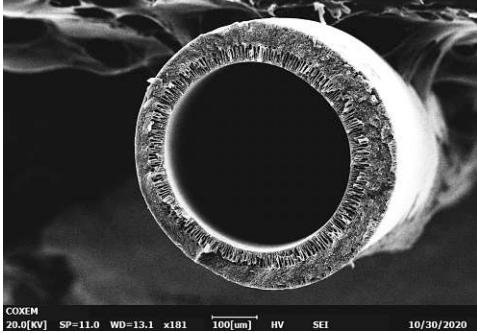
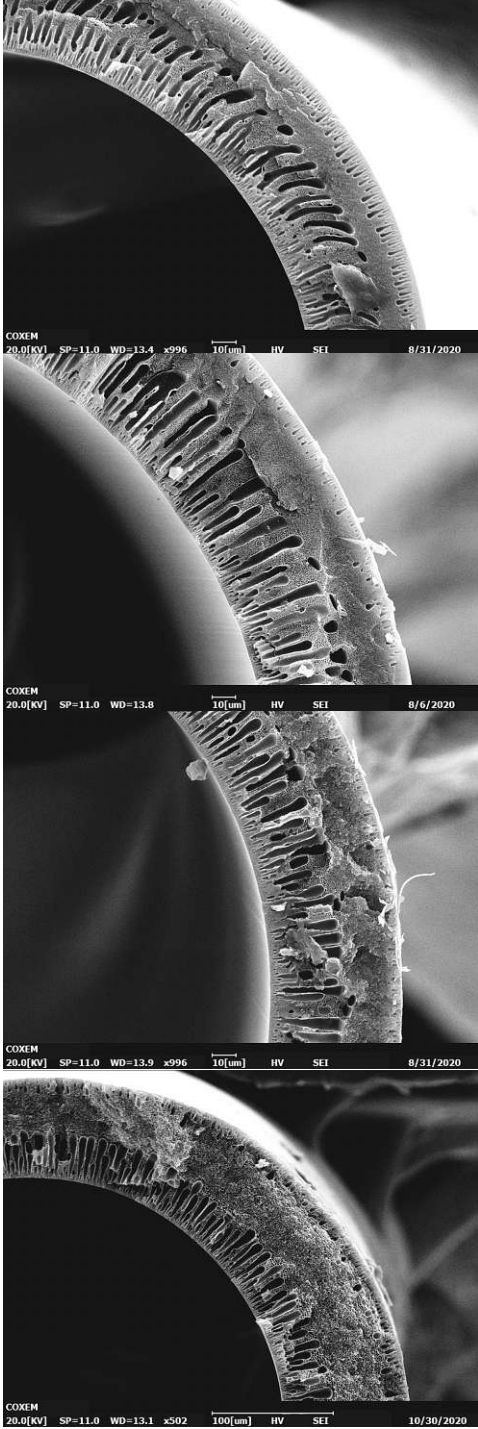
- 10.4028/www.scientific.net/AMR.896.37.
- [58] Purdue University, 'Viscosity'.
<https://www.chem.purdue.edu/gchelp/liquids/viscosity.html> (accessed Apr. 26, 2022).
- [59] N. Bolong, A. Ismail, and M. Salim, 'Effect of Jet Stretch in the Fabrication of Polyethersulfone Hollow Fiber Spinning for Water Separation', *J. Appl. Membr. Sci. Technol.*, vol. 6, Nov. 2017, doi: 10.11113/amst.v6i1.50.
- [60] J. Karger-Kocsis, Ed., *Polypropylene: an A - Z reference*. Dordrecht: Kluwer Academic Publishers, 1999.
- [61] S. Richardson, 'The die swell phenomenon', *Rheol. Acta*, vol. 9, no. 2, pp. 193–199, Apr. 1970, doi: 10.1007/BF01973479.
- [62] P. C. Hiemenz and T. Lodge, *Polymer Chemistry*, 2nd ed. Boca Raton: CRC Press, 2007.

10 Appendix

10.1 SEM Pictures

10.1.1 PES Concentration Variation

Table 27: SEM pictures; PES concentration variation

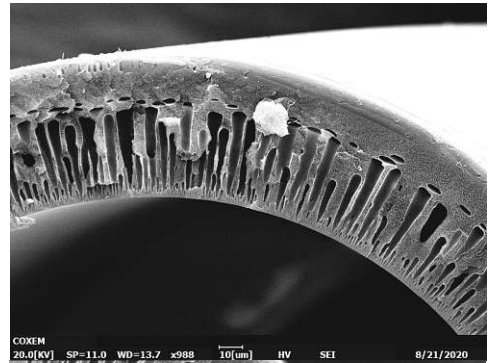
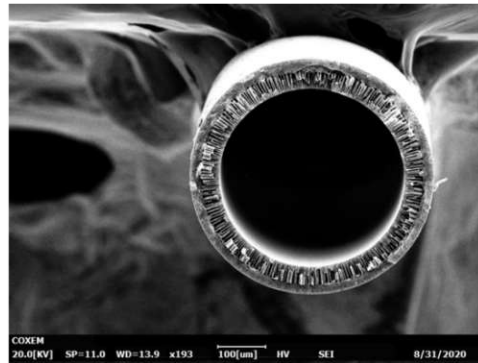
Identifier	
A_40	
B_ST40	
C_40	
D_40	
	

10.1.2 Spinning Dope B; Temperature Variation

Table 28: SEM pictures; temperature variation

Identifier

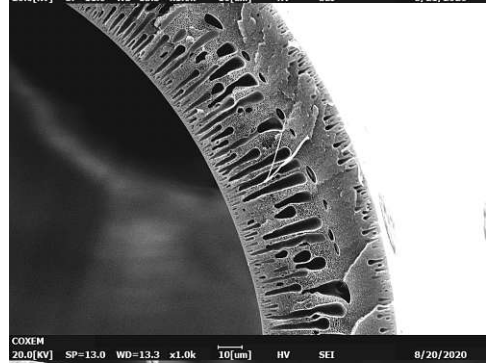
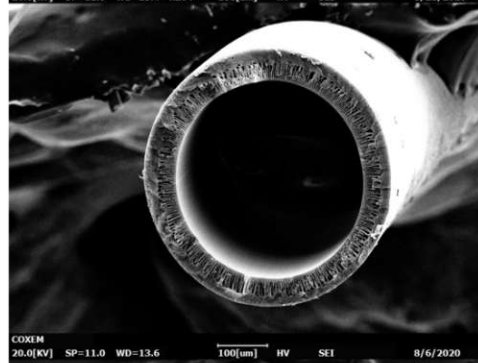
B_ST30



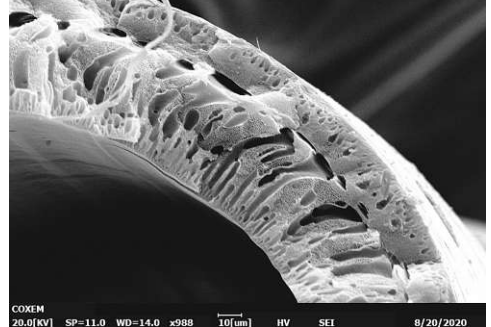
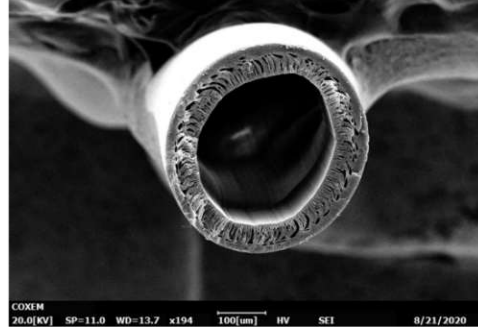
B_ST40



B_ST50



B_ST65

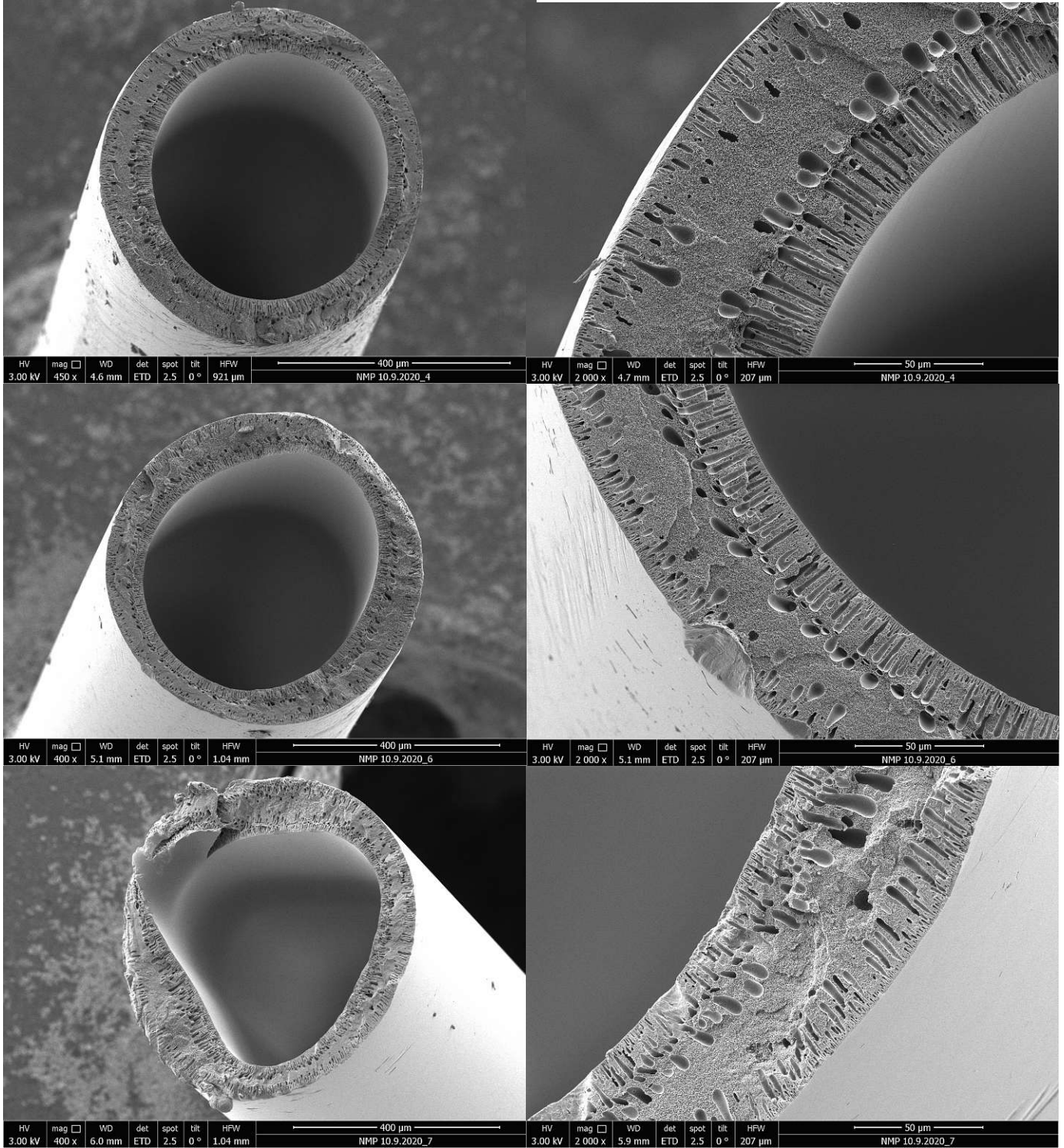


10.1.3 Spinning Dope B; Air Gap Length Variation

Table 29: SEM pictures; air gap variation

Identifier

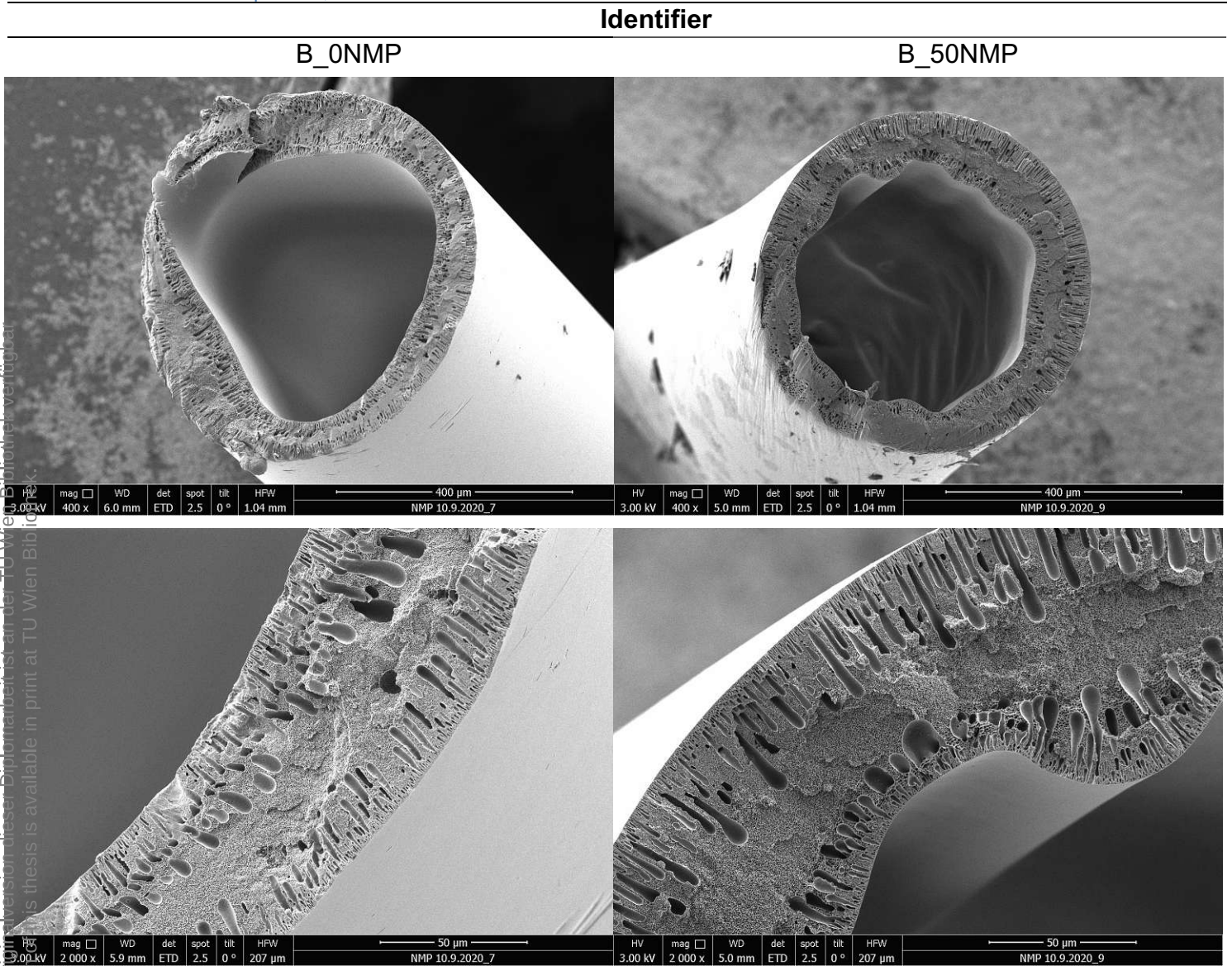
B_AG 65
 B_AG 130
 B_AG 260



Die approbierte gedruckte Originalversion dieser Diplomarbeit ist an der TU Wien Bibliothek verfügbar
 The approved printed original version of this thesis is available in the TU Wien Bibliothek.

10.1.4 Spinning Dope B; Variation of NMP Concentration in Bore Fluid

Table 30: SEM pictures; NMP concentration in bore fluid variation



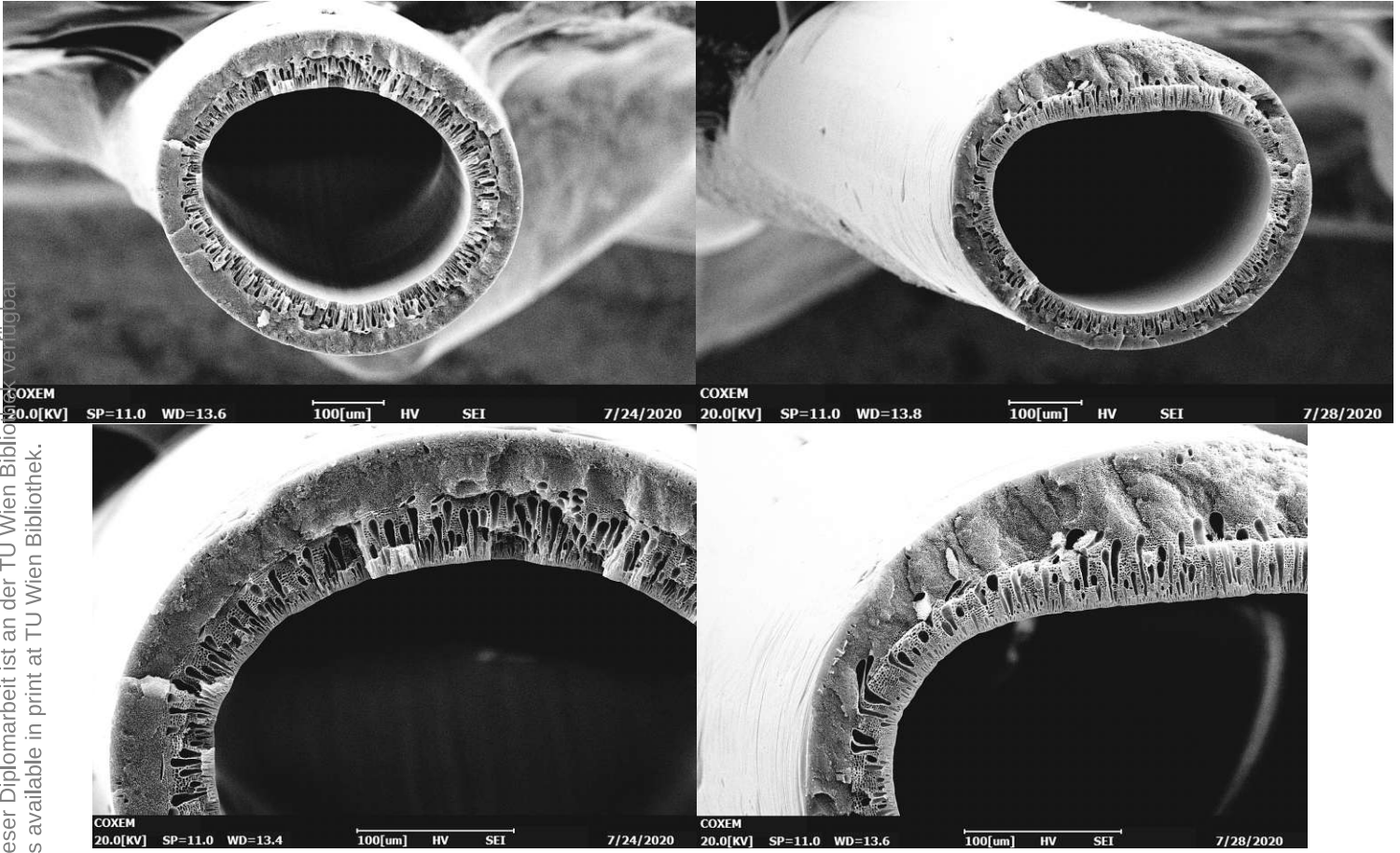
10.1.5 Spinning Dope D; Coagulation Bath Temperature Variation

Table 31: SEM pictures; coagulation bath temperature variation

Coagulation Bath Temperature [°C]

25

45



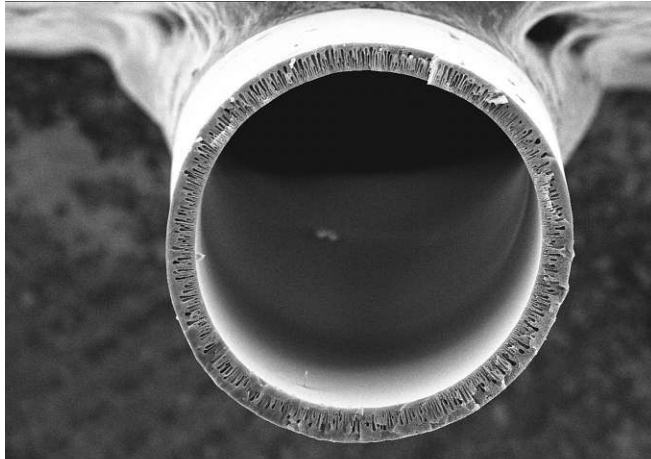
Die approbierte gedruckte Originalversion dieser Diplomarbeit ist an der TU Wien Bibliothek verfügbar.
The approved original version of this thesis is available in print at TU Wien Bibliothek.

10.1.6 Spinning Dope D; Dope/Bore Fluid Flow Rate Variation

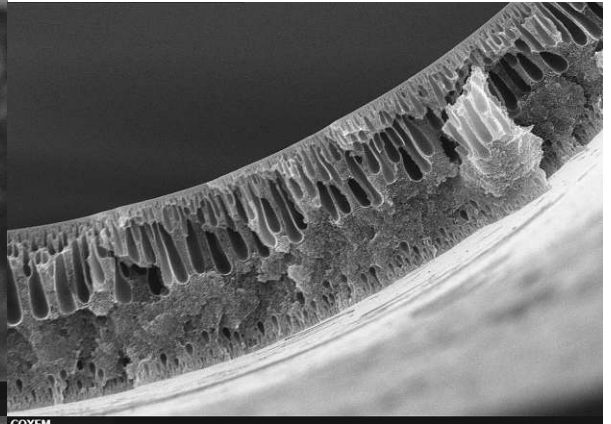
Table 32: SEM pictures; flow rate variation

Identifier

D_BFF0,12



COXEM
20.0[kV] SP=11.0 WD=13.8 x182 100[um] HV SEI 12/10/2021

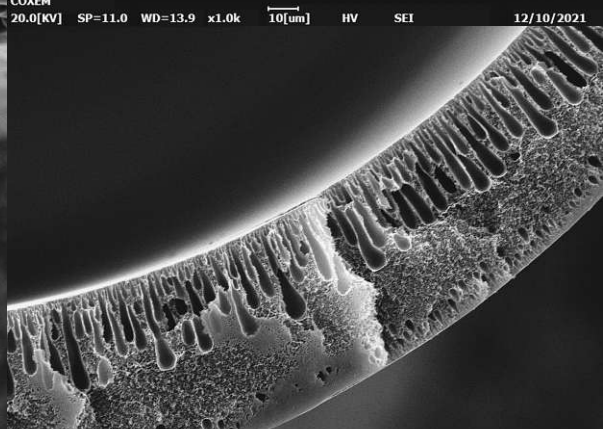


COXEM
20.0[kV] SP=11.0 WD=13.9 x1.0k 10[um] HV SEI 12/10/2021

D_BFF0,24



COXEM
20.0[kV] SP=11.0 WD=14.3 x170 100[um] HV SEI 12/10/2021

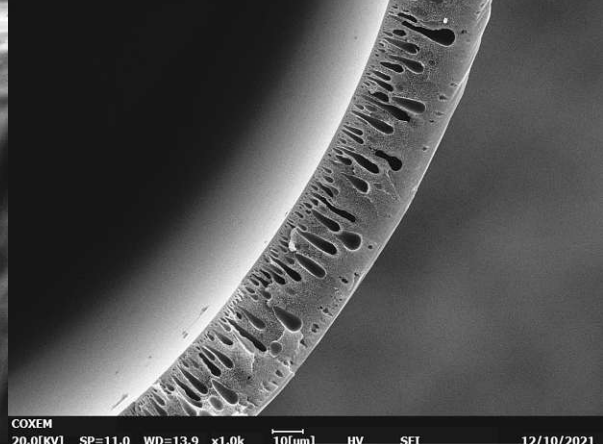


COXEM
20.0[kV] SP=11.0 WD=14.0 x1.0k 10[um] HV SEI 12/10/2021

D_BFF0,36



COXEM
20.0[kV] SP=11.0 WD=14.1 x180 100[um] HV SEI 12/10/2021

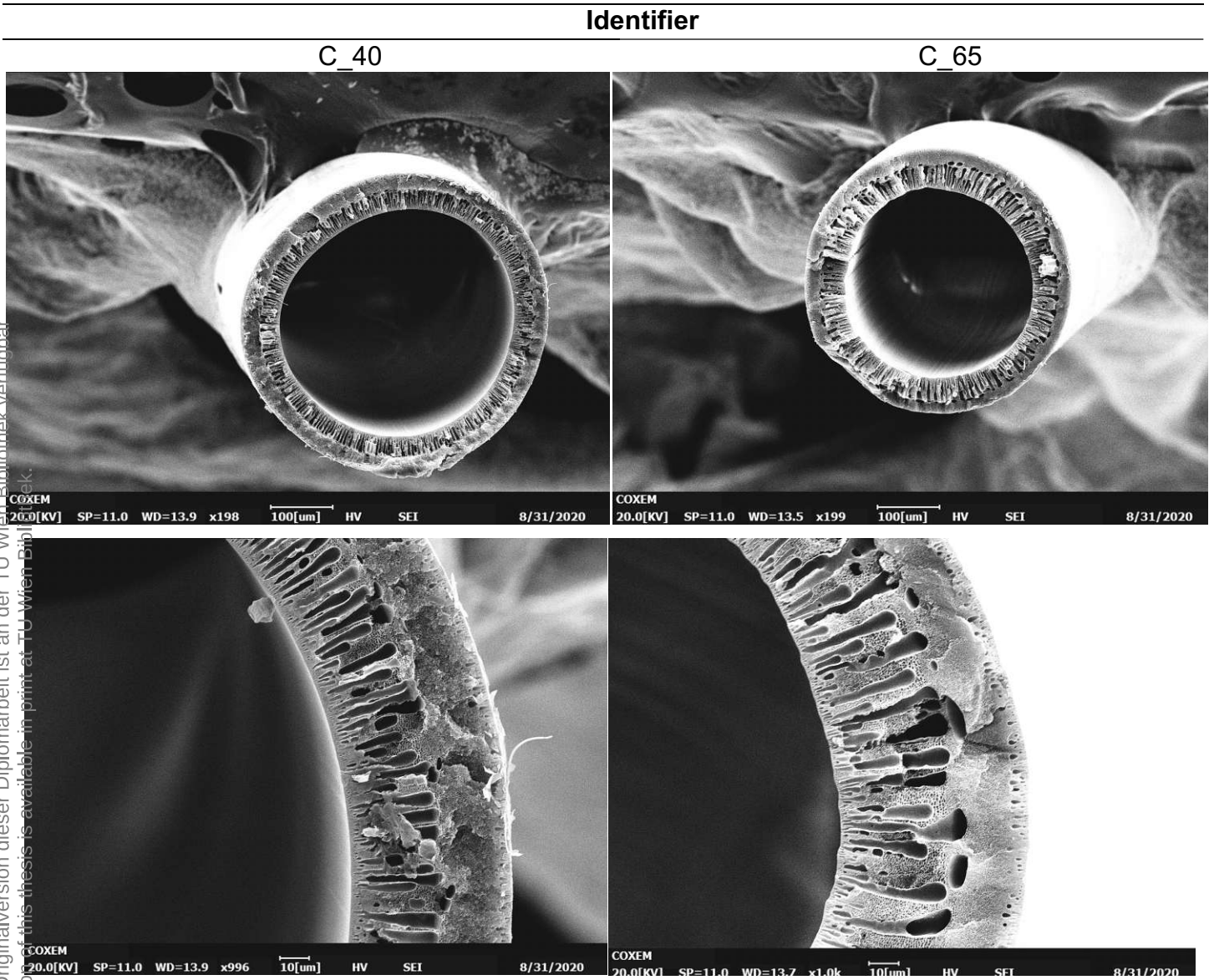


COXEM
20.0[kV] SP=11.0 WD=13.9 x1.0k 10[um] HV SEI 12/10/2021

Die approbierte gedruckte Originalversion dieser Diplomarbeit ist an der TU Wien Bibliothek verfügbar
The approved original version of this thesis is available in print at TU Wien Bibliothek.

10.1.7 Spinning Dope C; GP Experiment (Temperature Variation)

Table 33: SEM pictures; GP experiment



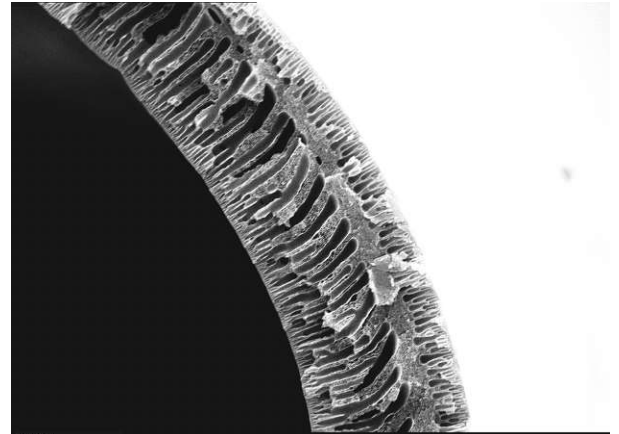
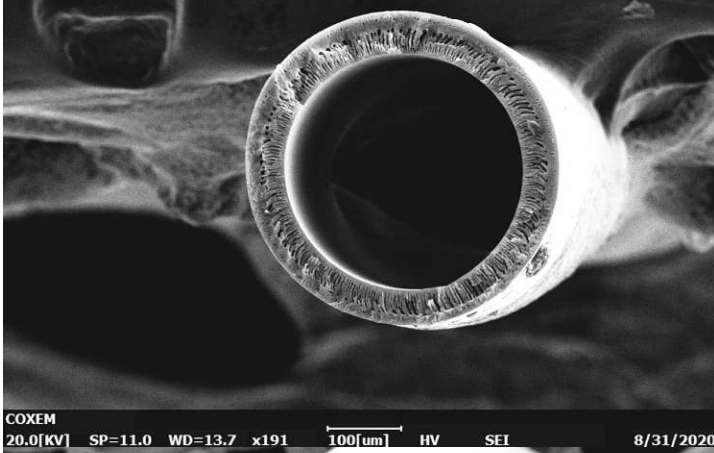
Die approbierte gedruckte Originalversion dieser Diplomarbeit ist an der TU Wien Bibliothek verfügbar.
 The approved original version of this thesis is available in print at TU Wien Bibliothek.

10.1.8 Spinning Dopes, A_40, E and F; Additive Variation

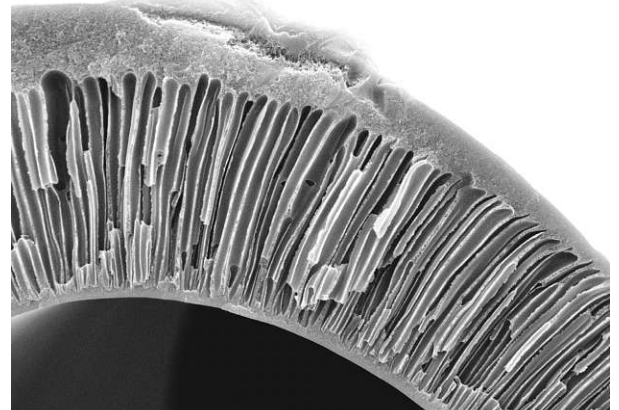
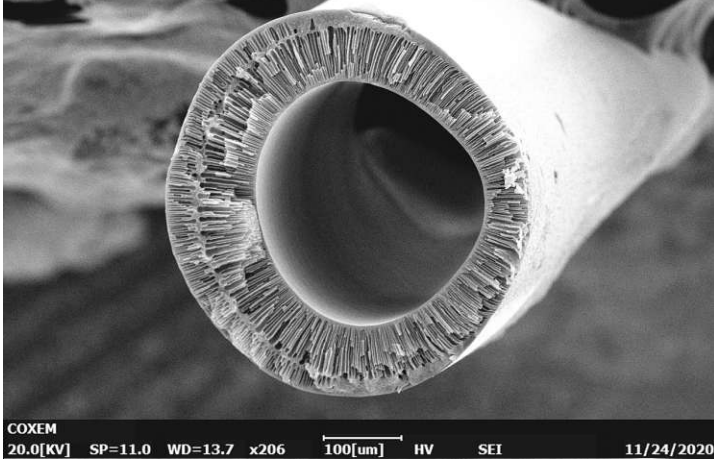
Table 34: SEM pictures; additive variation

Identifizier

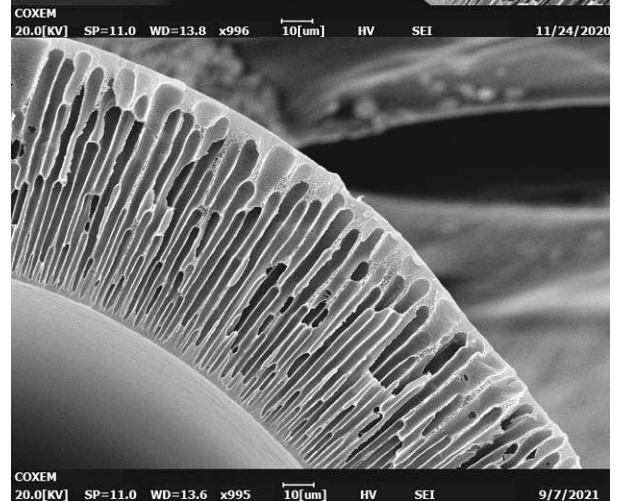
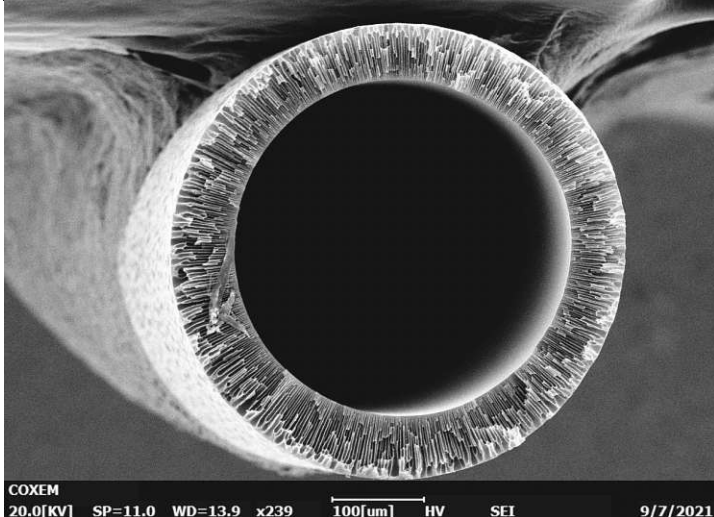
A_40



E_40



F_40



10.2 Abbreviations

MF	microfiltration
NF	nanofiltration
UF	ultrafiltration
RO	reverse osmosis
ED	electrodialysis
NIPS	nonsolvent -induced phase separation
TIPS	temperature-induced phase separation
VIPS	vapour-induced phase separation
MW	molecular weight
MWCO	molecular weight cut-off
PES	polyethersulfone
PEG	polyethylene glycol
PSf	polysulfone
CA	cellulose acetate
CTA	cellulose triacetate
CN	cellulose nitrate
PTFE	polytetrafluoroethylene
PVDF	polyvinylidene fluoride
PE	polyethylene
PP	polypropylene
PVC	polyvinylchloride
PAN	polyacrylonitrile
PI	polyimide
PEEK	polyetheretherketone
PEEK-WC	modified polyetheretherketone
PEI	polyetherimide
PA	polyamide
PC	polycarbonate
PLA	polylactic acid
CED	cohesive energy density
EIPS	evaporation-induced phase separation
DIPS	diffusion-induced phase separation
SIPS	solvent-induced phase separation
RIPS	reaction-induced phase separation
L-L	liquid-liquid
NMP	n-methyl-2-pyrrolidone
DMAc	dimethylacetamide
DMF	n, n-dimethylformamide
TEP	triethyl phosphate
DMSO	dimethylsulfoxide

THF	tetrahydrofuran
PVP	polyvinyl pyrrolidone
PWP	pure water permeability
BSA	bovine serum albumin
EG	ethylene glycol
G	glycerin
P	polymer
S	solvent
NS	nonsolvent
DER	dope extrusion rate

10.3 Symbols and Mathematical Abbreviations

J	volume flux
J_i	flux of component i
J_w	water flux
A	phenomemological coefficient
D	diffusion coeffiecient
L_p	permeability coefficient
c	concentration
T	temperature
-1/R	electrical conductivity
λ	thermal diffusivity
ν	kinematic viscosity
$\Delta\zeta$	membrane thickness
S_{AB}	selectivity of component A
x_A, x_B	mole fraction of component A and B in feed
y_A, y_B	mole fraction of component A and B in permeate
α_{AB}	separation factor
R_A	rejection of component A
C_A^p, C_A^f	concentration of A in permeate and feed
V_i	partial molar volume
μ_i	chemical potential
a_i	activity of component i
p, P	pressure
R	specific gas constant
τ	membrane tortuosity
k^f, k^p	partition coefficients

λ	free path of solute molecules
d_s	molar size of solute
d_p	pore diameter
r	pore radius
η	dynamic viscosity
ε	surface porosity
n_p	number of pores
A_m	membrane area
S	internal surface area
K	Carman-Kozeny constant
ε_π	pore cross-section area available for the small particle
ε_α	pore cross-section area available for the large particle
k	Boltzmann constant
D_k	Knudsen diffusion coefficient
M_w	molecular weight
G	Gibbs' free energy
H	enthalpy
S	entropy
G_m	Gibbs' free energy of mixing
H_m	enthalpy of mixing
S_m	entropy of mixing
n_i	number of moles of component i
G_i^0	Gibbs molar function of component i
ΔE	energy of vaporisation
$\frac{\Delta E}{V}$	cohesive energy of density
δ	solubility parameter
$\phi_1 \phi_2$	volume fractions of components 1 and 2
$\delta_\delta, \delta_\pi, \delta_\eta$	solubility parameter of dispersion forces, dipole-dipole forces and hydrogen bonding
N_{av}	Avogadro's number
χ_{12}	Flory-Huggins interaction parameter